Universität Hamburg
DER FORSCHUNG | DER LEHRE | DER BILDUNG

Inbetriebnahme eines Teststandes zur Charakterisierung von JUNO Photomultipliern

Commissioning of a test facility to characterise JUNO photomultipliers

Abschlussarbeit zur Erlangung des akedemischen Grades
Bachelor of Science
im Studiengang Physik

an der

Universität Hamburg
Fakultät für Mathematik, Informatik und Naturwissenschaften
Fachbereich Physik

von

Benedict Oliver Albert Kaiser
geboren am
12.01.1995 in Tübingen

Vorgelegt am: 14. November 2016
Erstgutachterin: Frau Prof. Dr. Caren Hagner
Zweitgutachter: Herr Dr. Björn Wonsak

Benedict O. A. Kaiser
Commissioning of a test facility to characterise JUNO photomultipliers
Bachelor thesis, 14th November 2016

Forschungsgruppe Neutrinophysik
Institut für Experimentalphysik
Universität Hamburg
Luruper Chaussee 149
22761 Hamburg
Federal Republic of Germany

Inbetriebnahme eines Teststandes zur Charakterisierung von JUNO Photomultipliern

Benedict Oliver Albert Kaiser

14. November 2016

Zusammenfassung

Das Jiangmen Underground Neutrino Observatory (JUNO) ist ein auf etwa 20 kt Flüssigszintillator basierender Antineutrino Detektor (engl.: LAND) der gegenwärtig in Jiangmen, China aufgebaut wird. Im inneren Behälter des Detektors werden 36 000 Photomultiplier (PMTs) mit einem Durchmesser von 20 Zoll sowie 18 000 PMTs mit einem Durchmesser von 3 Zoll verbaut. In einem zusätzlichen Veto-Detektor finden 1600 weitere 20 Zoll PMTs Verwendung. Im Rahmen der vorliegenden Bachelorarbeit wird ein Teststand zur Charakterisierung der 20 Zoll JUNO Photomultiplier in Betrieb genommen. Im Zuge dessen wird ein Temperaturüberwachungssystem für den Teststand implementiert. Hierbei werden verschiedene Sensortypen und Systeme auf ihre Eignung untersucht. Das endgültige System wird durch eine Arduino MEGA2560 Mikrokontrollerplatine und digitale DS18B20 Sensoren realisiert. Anschließend wird das System in LabView eingebunden. Außerdem wird mittels LabView eine Fernsteuerung für die Temperatursteuerungseinheit des Teststandes implementiert. Des Weiteren wird das im Teststand vorherrschende Magnetfeld untersucht. Dabei zeigt sich, dass eine Abschirmung aus Weicheisen die Feldstärke des Erdmagnetfeldes auf weniger als 10 % reduziert. Darüber hinaus werden an zwei kleineren, bereits vorhandenen Teststanden Dunkelstrom- und Koinzidenzmessungen mit verschiedenen Photomultipliern durchgeführt.

Commissioning of a test facility to characterise JUNO photomultipliers

Benedict Oliver Albert Kaiser

14th November 2016

Abstract

The Jiangmen Underground Neutrino Observatory (JUNO) is a Liquid Scintillator Antineutrino Detector (LAND) that is currently being built in Jiangmen, China. JUNO will use approximately 20 kt of liquid scintillator. In the inner vessel of the detector, 36 000 photomultiplier tubes (PMTs) with a diameter of 20 inches and 18 000 PMTs with a diameter of 3 inches will be used. Moreover, a veto detector will hold 1600 additional 20-inch PMTs. In this bachelor thesis, a test facility to characterise the 20-inch JUNO photomultiplier tubes is commissioned. A temperature monitoring system for the test stand is implemented. Therefore, various sensor types and readout systems are tested. The final system is realised using DS18B20 digital sensors that are read out using an Arduino MEGA2560 microcontroller board. The monitoring system is integrated into LabView. Moreover, a LabView based remote control system for the temperature control system of the test stand is developed. Also, the magnetic field inside the test stand is analysed. It is found that the magnetic field strength is reduced to less than 10 % of the earth's magnetic field using a soft iron shielding. Additionally, dark count and coincidence measurements with different photomultipliers are performed at two smaller, already existing test stands.

Contents

Introduction

In the last few decades, intensive global research showed that the Standard Model of particle physics is incomplete and needs to be generalised. One prominent observation is that neutrinos are massive leptons which have mixing mass eigenstates. Until now, the ordering of the neutrino mass eigenstates, i.e. the mass hierarchy, could not be determined.

The Jiangmen Underground Neutrino Observatory (JUNO) is a Liquid Scintillator Antineutrino Detector (LAND) [Gra16] consisting of a cylindrical water tank containing a veto detector as well as an inner vessel holding 20 kt of Linear Alkyl-Benzyne (LAB) liquid scintillator material. The JUNO project is aimed at determining the mass hierarchy. The JUNO detector will be built in Jiangmen, China, near two nuclear power plants. Via the detection of reactor anti electron neutrinos $\overline{\nu}_e$, JUNO will deliver data about the ordering of the neutrino mass eigenstates. To fulfil the requirements for the energy resolution of at least 3 % at 1 MeV needed to resolve the mass hierarchy, a stainless steel latticed shell around the detectors inner vessel will hold 18 000 photomultiplier tubes with a diameter of 20 inches that are complemented by up to 36 000 smaller 3-inch PMTs. Additionally, the veto detector comprised of 1600 PMTs with a diameter of 20 inches will veto signals from cosmic muons.

All of the PMTs that will be used in JUNO have to be characterised and calibrated individually. In order to obtain comparable results and calibration data, an automated testing setup is necessary. For the 20-inch PMTs, these testing setups consists of four specially designed shipping containers. These test facilities are being developed by the University of Hamburg and the Eberhard-Karls-University Tübingen.

Great emphasis of this thesis lies on these JUNO mass test stands. The performance characteristics of the photomultipliers that will be tested depend on environmental conditions such as the temperature. Hence, it is of the utmost importance to either constantly monitor these conditions or to diminish their influences on the PMTs up to a point where they are practically insignificant.

Thus, a temperature monitoring system for the test stand is implemented within this thesis. For this purpose, two different systems, a programmable logic controller (PLC), and different Arduino microcontroller boards are tested. Here, the main focus lies on the assessment of the Arduino microcontrollers. These systems are tested with two analogue sensor variants (platinum resistance detectors and LM35 series sensors) and DS18B20 digital sensors. For each tested system the required circuitry as well as the observed advantages and disadvantages are discussed and the final system is integrated into LabView. The working principle of the LabView VI and the designed user interface are explained.

Additionally, the test stand is equipped with a Heating, Ventilation and Air Conditioning (HVAC) unit. With this PLC-controlled unit the temperature in the inside can also be monitored and be held at constant temperature levels ranging from −40 °C to 50 °C. The set temperature can, however, only be adjusted via hardware buttons directly on the controller. Thus, a remote control system for the temperature control system of the container is implemented using LabView. This greatly simplifies a part of the operation of the test stand. The plan for PMT testing also sets forth that a few photomultipliers will be aged artificially in order to evaluate their performances over time beforehand. This will be done by increasing and decreasing the set temperature periodically, imposing mechanical stress on the PMTs. For this purpose, the option to remotely control the HVAC unit is practically mandatory.

In future, the JUNO mass test stands will be frequently used to test the required 20-inch photomultiplier tubes. Therefore, the detailed explanations of the temperature monitoring system and the remote control system developed within the scope of this thesis shall also partly serve as a documentation for these systems.

Photomultiplier tubes are also highly dependant on external magnetic fields. Even magnetic fields as weak as the terrestrial magnetic field can significantly hamper the performance of a PMT. To alleviate this issue, the test stand is equipped with a passive magnetic soft iron shielding. In this thesis, the magnetic field inside the test stand is evaluated with and without this shielding material in order to confirm its proper installation and functionality.

Two smaller test stands in a laboratory of the Hamburg University aim to reproduce the conditions that will prevail inside the JUNO mass test stands. Both of these small test stands are described briefly. In both test stands, dark count rate measurements with a small 2-inch and a larger 20-inch PMT are performed within the scope of this thesis. Additionally, a coincidence circuit in combination with the small PMT is tested.

Chapter 1 of this bachelor thesis covers the basics of neutrino physics and neutrino oscillations which are relevant for the JUNO experiment. Afterwards, the JUNO experiment itself is described in chapter 2. Chapter 3 outlines the principle of photomultiplier tubes. Subsequently, the dark count measurements as well as the coincidence measurements with the two smaller test stands are described in chapter 4. In chapter 5, the measurements of the magnetic field inside the JUNO mass test stand are illustrated. Chapter 6 comprehensively describes the temperature monitoring system developed for the test stand. The implementation of the HVAC unit's remote control system is finally explained in chapter 7.

Part I

Theoretical background

Within the scope of this thesis, the theoretical background covers neutrino physics, the JUNO-experiment as well as the principle of photomultiplication. Chapter 1 covers the basics of neutrino physics and neutrino oscillations which are necessary for the JUNO-project. In chapter 2, an overview of the JUNO detector and the scientific objectives of the experiment is given. The principle of photomultiplication utilising photomultiplier tubes is explained in chapter 3.

1 Neutrino physics

"I have hit upon a desperate remedy to save the "exchange theorem" [...] of statistics and the law of conservation of energy. Namely, the possibility that in the nuclei there could exist electrically neutral particles, which I will call neutrons, that have spin 1/2 and obey the exclusion principle and that further differ from light quanta in that they do not travel with the velocity of light [Pol10]."

— Wolfgang Pauli (December 4, 1930)

With these words, addressed to a physicist meeting in Tübingen, Germany, Wolfgang Pauli proposed the existence of electron neutrinos (at the time: neutrons) in order to explain the conservation of energy, momentum and angular momentum of the beta decay. Until now, neutrinos have been proven to have highly interesting features resulting in whole research groups dedicating themselves to neutrino physics. In this chapter, a short introduction into the Standard Model and the neutrinos within it is given in section 1.1. After that, sections 1.2 and 1.3 explain the phenomenon of neutrino oscillations and their mass hierarchy. Finally, the inverse beta-decay shall be outlined, as this is essential for the JUNO project which is described in the subsequent chapter.

1.1. Neutrinos and the Standard Model

The Standard Model (SM) summarises the essential knowledge about particle physics. However, it is incomplete. It describes all known elementary particles and combines their fundamental interactions within the framework of a consistent quantum field theory (QFT). The quantum field theory is an expanded theory combining classical field theories with quantum mechanics. In the QFT, a particle is considered as an excited state of an underlying quantum field [Nar16]. These quantum fields allow a description of the strong and electroweak interactions within the Standard Model. It is based on a local symmetry of the gauge group [Sch16]

$$\underbrace{\mathrm{SU}(3)_\mathrm{C}}_{\text{strong}} \times \underbrace{\mathrm{SU}(2)_\mathrm{L} \times \mathrm{U}(1)_\mathrm{Y}}_{\text{electroweak}} . \tag{1.1}$$

The electroweak sector, described by the $\mathrm{SU}(2)_\mathrm{L} \times \mathrm{U}(1)_\mathrm{Y}$ group, is referred to as Glashow-Weinberg-Salam theory and describes the weak and electromagnetic interaction, i.e. two of the four fundamental interactions. The strong interaction, which is the third of the four fundamental interactions, is described through the theory of quantum chromodynamics (QCD) that is based on a $\mathrm{SU}(3)_\mathrm{C}$ gauge symmetry. The gauge groups $\mathrm{SU}(3)_\mathrm{C}$ and $\mathrm{SU}(2)_\mathrm{L}$ are Yang-Mills theories [EK16]. Gravitation, the fourth fundamental interaction, is not described within the Standard Model.

The three fundamental interactions can be explained by the transfer of exchange particles, so called gauge bosons, between the interacting particles. Bosons are particles with integral spin. According to Fermi's Golden Rule, the probability amplitude for an interaction is determined by the transition matrix element, which contains the coupling strength and a propagator term, describing the exchange of the virtual boson [Pov+15; KS95; Sch11].

Besides the aforementioned gauge bosons, the Standard Model, which is shown in figure 1.1, contains the Higgs-boson as well as twelve elementary fermions, i.e. particles with half-integral spin, and their associated antiparticles. They can be divided into *quarks* and *leptons*. The six quarks (up , down, charm, strange, top, bottom, often abbreviated by their first letter: u, d, c, s, b, t) do have a *colour charge*, which is the charge of the strong interaction. This colour charge can be red/anti-red ($r/\overline{r}$), green/anti-green ($g/\overline{g}$) or blue/anti-blue ($b/\overline{b}$). Quarks never exist as individual, isolated particles, but only in bound states (quark confinement) [Sch11]. A bound state can only exist, when the colour charges of its quarks add up to white. Quarks are particles with mass and have an electric charge of $2/3\,e$ $(\mathrm{u}, \mathrm{c}, \mathrm{t})$ or $-1/3\,e$ $(\mathrm{d}, \mathrm{s}, \mathrm{b})$, where $e = 1.6 \times 10^{-19}$ C is the elementary charge [Kuc14]. They are affected by all three interactions covered by the Standard Model. The leptons consist of the electrons (e^-), muons (μ^-) and tauons (τ^-) as well as their corresponding neutrinos: ν_e, ν_μ, ν_τ. The first type of leptons only differ in their mass, other properties, like their charge of $-1\,e$ are equal. Neutrinos are neutral particles which are, within the realm of the Standard Model, massless. Together with their related massive leptons, they form three types of lepton generations, also called family doublets:

$$\begin{pmatrix} \nu_e \\ e^- \end{pmatrix}, \begin{pmatrix} \nu_\mu \\ \mu^- \end{pmatrix}, \begin{pmatrix} \nu_\tau \\ \tau^- \end{pmatrix}. \tag{1.2}$$

Leptons do not couple with gluons, the exchange particles of the strong interaction. Similar to quarks, gluons have a colour charge. The number of possible (anti) colour combinations can be derived from the group theory and is given by $3 \otimes \overline{3} = 8 \oplus 1$. This means, that the direct product of a colour triplet and an anti colour triplet forms a direct sum of an octet and a singlet ($r\overline{r} + g\overline{g} + b\overline{b}$, without normalisation factor). Due to symmetry of the singlet, only the gluons of the colour octet exist. Although gluons are massless, the quark confinement results in the strong interaction being short ranged, with an interaction length of approximately 1.5 fm.

The neutrinos are only affected by the weak interaction, which is mediated by the $W^\pm$ as well as the Z^0 boson. Due to their comparatively high masses of $m_{W^\pm} = 80.385(15)$ GeV and $m_{Z^0} = 91.188(2)$ GeV [Oli14], the weak interaction is very short ranged. For reference, the exchange particle of the electromagnetic interaction, the photon γ, has a rest mass of $m_\gamma = 0$ eV, resulting in an unlimited interaction length. The fact that neutrinos are massless, neutral and are only affected by the weak interaction gives them a special place in the Standard Model. The SM provides a good concept to describe elementary particles and their interactions, however it needs to be extended in order to include phenomena like *neutrino-oscillations*, i.e. the conversion of one neutrino into a differently flavoured one.

In 1930, neutrinos were first proposed by PAULI in order to explain the conservation of energy, and (angular) momentum of the β-decay (see introductory quote). The anti electron neutrino $\overline{\nu}_e$ was first discovered in the COWAN-REINES experiment [Cow+56] in 1956 via the inverse β-decay ($\overline{\nu}_e + p \rightarrow n + e^+$). From the WU experiment [Wu+57] and the GOLDHABER experiment [GGS58] a few years later it was concluded, that neutrinos are left-handed while antineutrinos are right-handed, signifying a maximum in parity violation. Parity is a symmetry property of a system towards a spatial reflection. A parity transformation $\mathcal{P}$ changes the sign of all three coordinates; $\mathcal{P} : (x, y, z) \mapsto (-x, -y, -z)$, thus transforming a right handed coordinate system into a left handed and vice versa. Should a physical process not change after a parity transformation, the parity is conserved. In the opposite case, parity is violated.

Until now, all three neutrino types could be directly detected due to the achievements of LEDERMANN *et.al* (Brookhaven, 1962) [Dan+62] and the DONUT collaboration (Fermilab, 2000) [Kod+01].

In the early 1970s, a deficit in the solar neutrino flux, known as the solar neutrino problem, was observed by DAVIS *et al.* in the Homestake experiment [BD76]. Here, the rate of electron neutrinos from the sun reaching the earth was found to be lower than expected. In 1998, the Super-Kamiokande detector in Japan reported strong evidence for the oscillation of atmospheric neutrinos [Fuk+98]. A clear confirmation of solar electron-neutrinos converting into muon- and tau-neutrinos was published in 2001 by the Sudbury Neutrino Oberservatory (SNO) Collaboration [SNO01]. With neutrino oscillations the solar neutrino problem could be explained.

Such neutrino oscillations require flavour mixing and that neutrinos are particles with mass. Both of these prerequisites are beyond the Standard Model. In oscillation experiments, the mass of neutrinos cannot be determined directly, but rather only the differences between their squared masses. Other methods to determine the mass of neutrinos include the search for the neutrino-less double beta ($0\nu\beta\beta$) decay (e.g. at the GERDA experiment [Bet07]) or the direct determination via the energy spectrum of electrons in the case of a tritium β-decay (e.g. at the KATRIN-experiment [Ang+05]). Furthermore, cosmological measurements (e.g. via Cosmic Microwave Background measurements with the Planck Surveyor, [Giu+13]) can be used to gain insights into neutrino masses [Pov+15].

It is currently unclear, whether the mass of neutrinos is caused by the Dirac mechanism, in which neutrinos are Dirac particles coupling to the Higgs boson. Dirac particles are fermions that differ from their antiparticles. Thus, four different states exist for Dirac particles. Should, for example, an electron-neutrino be a Dirac particle, these states would be $(\nu_{e,\uparrow}, \nu_{e,\downarrow}, \overline{\nu}_{e,\uparrow}, \overline{\nu}_{e,\uparrow})$ [Pov+15]. Here, $\uparrow$ and $\downarrow$ denote a positive and negative helicity respectively. Alternatively, the mass could result from the neutrinos following the Majorana mechanism due to their electrically neutral charge. Contrary to Dirac particles, Majorana particles do not differ from their anti-particles. In this case, the electron-neutrino would be the same as the anti-electron neutrino and only two states $(\nu_{e,\uparrow}, \nu_{e,\downarrow})$ would exist. The Majorana mechanism is beyond the Standard Model.

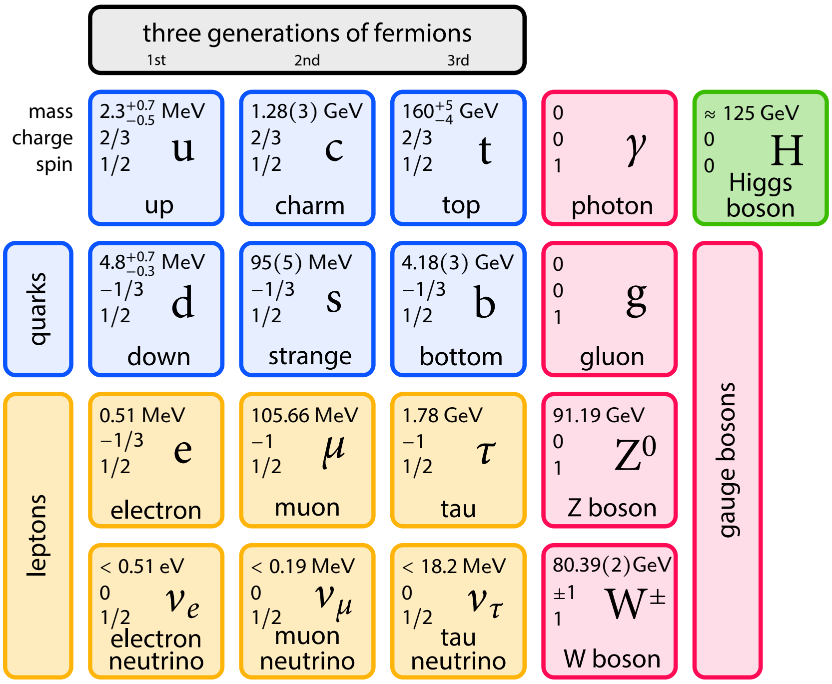

Figure 1.1.: Overview of the standard model. The quarks are depicted in blue, the leptons in yellow and the gauge bosons in red. In this depiction, the standard model is extended to include neutrino masses and the Higgs boson. The values for the mass, charge and spin originate from [Oli14].

1.2. Neutrino oscillations

Neutrino oscillations are the phenomenon of spontaneous and periodic changes from one neutrino flavour to another [An+15]. As mentioned before, they require flavour mixing as well as massive neutrinos. This means, that the weak eigenstates

$$|\nu_\alpha\rangle\,, \alpha = e, \mu, \tau \tag{1.3}$$

of the neutrinos differ from the mass eigenstates, which are denoted by

$$|\nu_i\rangle\,, i = 1, 2, 3. \tag{1.4}$$

Specifically the formalism states that the weak eigenstates and the mass eigenstates are comprised of linear combinations of each other:

$$\begin{aligned} |\nu_\alpha\rangle &= \sum_i U_{\alpha i} |\nu_i\rangle \\ |\nu_i\rangle &= \sum_\alpha U^*_{\alpha i} |\nu_\alpha\rangle . \end{aligned} \tag{1.5}$$

Here, $U_{\alpha i}$ are the entries of the transformation matrix $\mathbf{U}$. Their complex conjugations are denoted by $U^*_{\alpha i}$. In the standard three-flavour framework, $\mathbf{U}$ is a 3×3 matrix. Often it is referred to as PONTECORVO–MAKI–NAKAGAWA–SAKATA (PMNS) matrix [MNS62]. The PMNS matrix, which is the analogue to the CABIBBO-KOBAYASHI-MASKAWA (CKM) quark mixing matrix, is unitary (i.e. $\mathbf{U}^\dagger\mathbf{U} = \mathbf{U}\mathbf{U}^\dagger = \mathbf{I}$, where $\mathbf{I}$ denotes the identity matrix) and contains three mixing angles and a phase. It can be parametrized in the following way:

$$\begin{aligned} \mathbf{U} &= \begin{pmatrix} 1 & 0 & 0 \\ 0 & c_{23} & s_{23} \\ 0 & -s_{23} & c_{23} \end{pmatrix} \begin{pmatrix} c_{13} & 0 & s_{13}\mathrm{e}^{-\mathrm{i}\delta} \\ 0 & 1 & 0 \\ -s_{13}\mathrm{e}^{\mathrm{i}\delta} & 0 & c_{13} \end{pmatrix} \begin{pmatrix} c_{12} & s_{12} & 0 \\ -s_{12} & c_{12} & 0 \\ 0 & 0 & 1 \end{pmatrix} \mathbf{P}_\nu \\ &= \begin{pmatrix} c_{12}c_{13} & s_{12}c_{13} & s_{13}\mathrm{e}^{-\mathrm{i}\delta} \\ -s_{12}c_{23} - c_{12}s_{13}s_{23}\mathrm{e}^{\mathrm{i}\delta} & c_{12}c_{23} - s_{12}s_{13}s_{23}\mathrm{e}^{\mathrm{i}\delta} & c_{13}s_{23} \\ s_{12}s_{23} - c_{12}s_{13}c_{23}\mathrm{e}^{\mathrm{i}\delta} & -c_{12}s_{23} - s_{12}s_{13}c_{23}\mathrm{e}^{\mathrm{i}\delta} & c_{13}c_{23} \end{pmatrix} \mathbf{P}_\nu . \end{aligned} \tag{1.6}$$

Here, $c_{ij} \equiv \cos\theta_{ij}, s_{ij} \equiv \sin\theta_{ij}$ for $ij = 12, 13, 23$, where θ_{ij} are the mixing angles. The complex CP violating phase is denoted by δ and $\mathbf{P}_\nu$ is the diagonal Majorana phase matrix, which is indifferent for neutrino oscillations.

The probability to find a neutrino in a specific flavour changes with the time as the mass eigenstates are time dependent [Zub12]:

$$|\nu_i(x,t)\rangle = \exp(-\mathrm{i}E_i t)\, |\nu_i(x,0)\rangle . \tag{1.7}$$

Here, E_i is the energy of the mass eigenstate i and x the position of the neutrino with respect to its initial location. The time passed since the beginning of the propagation is denoted by t. Equation (1.7) holds true for neutrinos with the momentum p being emitted by a source located at $x = 0$ ($t = 0$):

$$|\nu_i(x,0)\rangle = \exp(\mathrm{i}px)\, |\nu_i\rangle . \tag{1.8}$$

Also, the neutrinos have to be relativistic [Zub12], i.e.

$$E_i = \sqrt{m_i^2 + p_i^2} \simeq E + \frac{m_i^2}{2E}. \tag{1.9}$$

Here it is assumed, that $p_i \gg m_i$, where m_i is the mass of the neutrino state i. The neutrino energy is given by $E \approx p$. Using equation (1.5) it follows, that a flavour eigenstate at $t = 0$ is described by

$$|\nu_\alpha(x,t)\rangle = \sum_i U_{\alpha i} \exp(-\mathrm{i}E_i t)\,|\nu_i\rangle \tag{1.10}$$

$$= \sum_{i,\beta} U_{\alpha i} U^*_{\beta i} \exp(\mathrm{i}px) \exp(-\mathrm{i}E_i t)\,|\nu_\beta\rangle\,. \tag{1.11}$$

The transition probability $P(\alpha \to \beta)$ to find a neutrino with the energy E that started out in the flavour state $|\nu_a\rangle$ after a certain time t in a different flavour state $|\nu_\beta\rangle$ can be determined using

$$P(\alpha \to \beta)(t) = \left|\langle \nu_\beta | \nu_\alpha(x,t)\rangle\right|^2. \tag{1.12}$$

Under the assumption of CP invariance it can be shown [Zub12], that this results in

$$P(\alpha \to \beta)(L/E) = \delta_{\alpha\beta} - 4 \sum_{j>i} U_{\alpha i} U_{\alpha j} U_{\beta i} U_{\beta j} \sin^2\left(\frac{\Delta m_{ij}^2}{4}\frac{L}{E}\right). \tag{1.13}$$

Here, L is the path length and $\Delta m_{ij}^2 = m_i^2 - m_j^2$ the difference between the squared masses of the two states i and j. Equation (1.13) makes it clear, that oscillations between flavour eigenstates occur. Their amplitude is determined by the elements of the PMNS matrix $\mathbf{U}$ and their frequency by the quotient $1/E$ as well as Δm_{ij}^2. Equation (1.13) also implies, that not all values for Δm_{ij} can be zero, as otherwise no oscillations would occur.

1.3. Mass hierarchy

In the standard three-flavour framework, six free parameters determine the behaviour of neutrino oscillations. These are the three mixing angles θ_{ij}, the CP-violating phase δ and two independent mass differences Δm_{ij}. Until now, various of these parameters were determined in different experiments (e.g. Borexino, KamLAND, SuperKamiokande) including the mass difference Δm^2_{21} as well as the three mixing angles $\theta_{12}, \theta_{13}, \theta_{23}$. While the value of $|\Delta m_{31}|^2$ is known, its exact sign and the phase δ are not yet known. Table 1.1 gives an overview of the parameters.

Table 1.1.: The best fit values as well as the 1σ intervals for the six three-flavour neutrino oscillation parameters. The data is based on an evaluation of current experimental data performed by Capozzi *et. al.* [Cap+14]. See also: [An+15].

Parameter	Normal hierarchy (NH)		Inverted hierarchy (IH)	
	Best fit	**1σ range**	**Best fit**	**1σ range**
$\Delta m^2_{21}/10^{-5}\mathrm{eV}^2$	7.54	7.32–7.80	7.54	7.32–7.80
$\Delta m^2_{31}/10^{-3}\mathrm{eV}^2$	2.47	2.41–2.53	2.42	2.36–2.48
$\sin^2\theta_{12}/10^{-2}$	3.08	2.91–3.25	3.08	2.91–3.25
$\sin^2\theta_{13}/10^{-1}$	2.34	2.15–2.54	2.40	2.18–2.59
$\sin^2\theta_{23}/10^{-1}$	4.37	4.14–4.70	4.55	4.24–4.94
$\delta/180°$	1.39	1.22–1.77	1.31	0.98–1.60

It has to be emphasized, that the absolute masses are unknown. Combined with the uncertainty of the sign of Δm^2_{31}, this gives two different possibilities for ordering the mass eigenstates:

$$m_1 < m_2 < m_3 \tag{1.14}$$

$$m_3 < m_1 < m_2. \tag{1.15}$$

This is called the *mass hierarchy* (MH), as shown in figure 1.2. The neutrinos can either follow the *normal hierarchy* (NH, relation 1.14) or the *inverted hierarchy* (IH, relation 1.15). Further experiments aiming to determine the mass hierarchy of neutrinos include the JUNO project, which is outlined in chapter 2.

The mass hierarchy of neutrinos is of great importance, as it is crucial for neutrino astronomy and cosmology. It is also a decisive factor for the measurement of the CP violating phase δ. Also, the mass hierarchy has to be known in order to design future experiments aimed at the detection of the neutrinoless double beta decay which is hoped to reveal, whether neutrinos are Dirac or Majorana particles. In general, the mass hierarchy is important to frame a precise model about neutrino masses and flavour mixing. Acquiring more data about it is required to determine the origin of the neutrino masses.

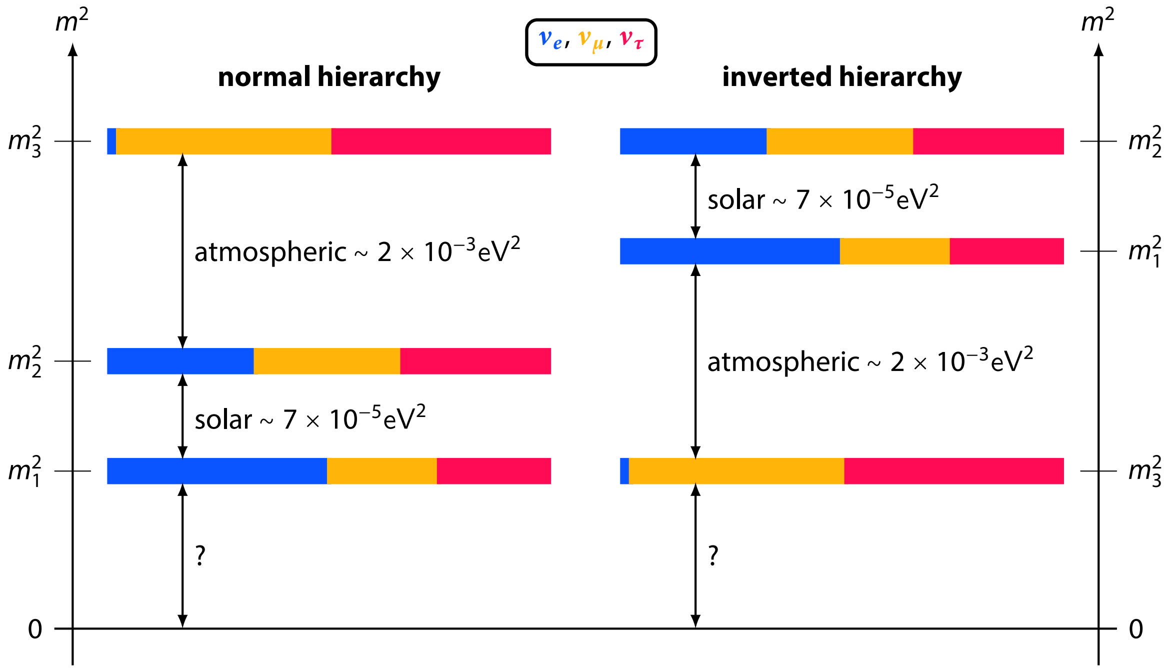

Figure 1.2.: The ordering of the neutrino mass eigenstates for the normal and inverted mass hierarchies. The colors indicate the proportion of the different neutrino flavours in each mass eigenstate. Representation adapted from [An+15].

On earth, nuclear reactors are one of the most intense, controllable, and well-understood sources of man-made neutrinos [VWZ15]. During the nuclear fission of ^{235}U,^{238} U,^{239} Pu and ^{241}Pu, elements are produced, which emit neutrons in order to approach the valley of stability. In average, the beta decay of these elements produces six electron-antineutrinos per fission [LS05]. Such reactor anti-neutrinos are suited for mass hierarchy measurements. The survival probability of an electron antineutrino can be derived (see [An+15]) from equation (1.13) to be

$$\begin{aligned} P(\overline{\nu}_e \to \overline{\nu}_e) = 1 - \sin^2(2\theta_{12})c_{13}^4 \sin^2\left(\frac{\Delta m_{21}^2 L}{4E}\right) \\ - \sin^2(2\theta_{13})\left[c_{12}^2 \sin^2\left(\frac{\Delta m_{31}^2 L}{4E}\right) + s_{12}^2 \sin^2\left(\frac{\Delta m_{32}^2 L}{4E}\right)\right], \end{aligned} \tag{1.16}$$

where $\Delta m_{32}^2 = \Delta m_{31}^2 - \Delta m_{21}^2$. The spectrum of oscillating reactor anti electron neutrinos is shown in figure 1.3. The first, dominant, term in equation (1.16) shows the oscillation that is solely ruled by the solar oscillation parameters Δm_{21}^2 and θ_{12}. In figure 1.3 this is drawn in solid black. An additional subdominant oscillation pattern occurs due to the last two terms in equation (1.16) which interfere with each other. Besides their slightly differing amplitudes, their oscillation frequencies differ also. This depends on the mass hierarchy. Resolving one of the subdominant oscillation patterns will allow to distinguish between the normal and inverted mass hierarchies. Until now, this could not be achieved, as such measurements require unprecedented energy resolutions of at least 3 % per 1 MeV. The JUNO detector (see chapter 2) will be the first purpose built experiment for determining the mass hierarchy, featuring an energy resolution of 3 % per 1 MeV. JUNO will measure $P(\overline{\nu}_e \to \overline{\nu}_e)$ of reactor neutrinos.

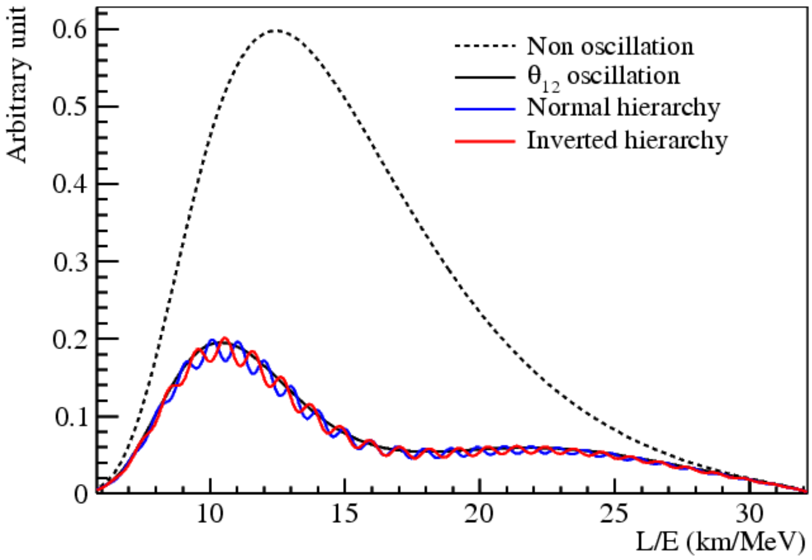

Figure 1.3.: The spectrum of reactor neutrinos as a function of L/E at a baseline of 60 km (black, dashed). The m^2_{21} term is depicted in solid black, the blue (red) curves are an explicit calculation for the normal hierarchy (inverted hierarchy). Source: [Lu14; Zha+08].

Anti electron neutrinos can be detected via the *inverse beta decay*:

$$\overline{\nu}_e + p^+ \longrightarrow e^+ + n. \tag{1.17}$$

Figure 1.4a shows the Feynman diagram of the inverse beta decay. Here, an electron antineutrino $\overline{\nu}_e$ interacts with a proton p^+ forming a positron e^+ and a neutron n. The outgoing positron annihilates almost instantly with an electron creating an easily detectable pair of photons ($e^+e^- \to \gamma + \gamma$, see figure 1.4b). After an average time of 200 µs, neutron-proton capture leads to a smaller delayed signal. Using coincidence techniques, this yields a very distinct and detectable antineutrino signature.

Besides JUNO, other projects to determine the mass hierarchy are currently being planned, including the ORCA (Oscillation Research with Cosmics in the Abyss [Kat13]) project. It is a deep-sea water Cherenkov experiment where the mass hierarchy measurement will be based on atmospheric neutrinos. Another project that is currently planned is the PINGU project (Precision IceCube Next Generation Upgrade [Ice16]). It is a proposed extension to the IceCube detector [Ach+06], which is a high-energy neutrino observatory located at the South Pole.

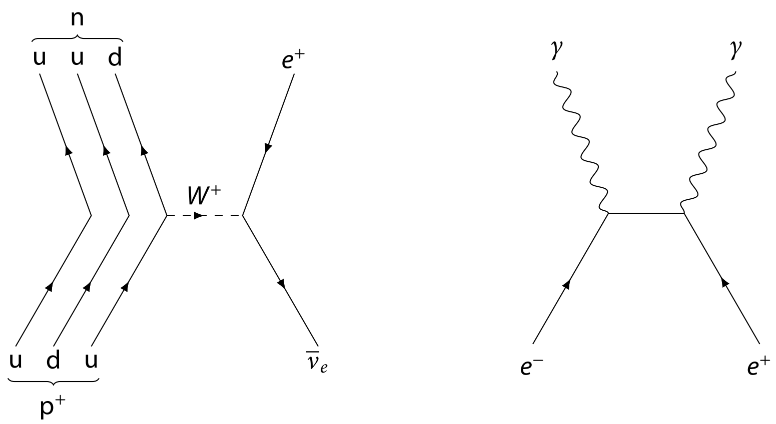

(a) Inverse β-decay.

(b) e^--e^+-annihilation.

Figure 1.4.: Feynman diagrams for the inverse beta-decay and the electron positron annihilation.

2 The JUNO-Experiment

This chapter, which is mainly based on [An+15; Ada+15; Li16], gives a short description of the JUNO-experiment. Section 2.1 outlines the scientific goal of JUNO as well as the detector layout and its location. Other goals which might be achieved with JUNO are briefly explained in section 2.2. Finally, section 2.3 illustrates the contribution of the University Hamburg to the JUNO project.

2.1. Overview and detector layout

The Jiangmen Underground Neutrino Observatory (JUNO) is a Liquid Scintillator Antineutrino Detector (LAND) that was proposed in 2008 and approved in 2013 [Gra16]. JUNO is planned to start taking data in 2020. It is a multi-purpose experiment with the main goal to determine the mass hierarchy of neutrinos via the detection of nuclear reactor antineutrinos, which were shortly discussed in the previous chapter. Due to the ratio L/E in equation (1.16) being known, the sign of Δm^2_{31} can be resolved by precisely determining the flux rate and energy spectrum of $\overline{\nu}_e \to \overline{\nu}_e$ oscillations. Additionally, the location of the JUNO detector optimises the ratio L/E to roughly $11\,\mathrm{km\,MeV^{-1}}$ granting the best sensitivity for the mass hierarchy determination. The sensitivity to the mass hierarchy is planned to reach 3σ to 4σ based on a six year data-taking period. JUNO will also improve the precision of Δm^2_{21}, Δm^2_{32} and $\sin^2\theta_{12}$. Currently, their accuracy is around 5 %, 3 % and 6 % percent respectively, JUNO targets a precision that exceeds 1 % for all three of the aforementioned oscillation parameters.

JUNO is a low statistics experiment. It is thus important to know the background sources in order to either reduce or identify background signals. In JUNO, this is done by building the detector underground and by using an additional veto detector. A major source of background is *accidental background*. This includes radioactivity from multiple sources including

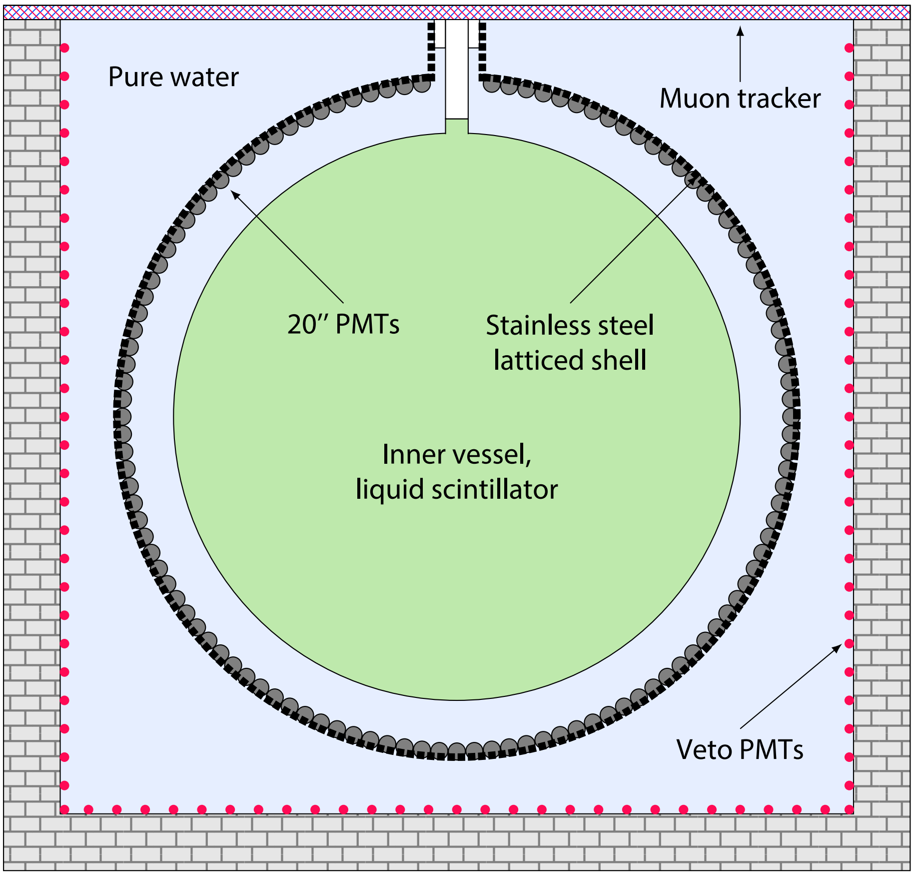

Figure 2.1.: A schematic view of the JUNO detector. It consists of a cylindrical water tank containing the veto detector and the inner vessel of the detector which holds 20 kt of liquid scintillator material. The required photomultiplier tubes are supported by a stainless steel latticed shell. Depiction adapted from [An+15].

the surrounding rocks and the PMT glasses as well as the spallation of neutrons and cosmogenic isotopes. In average, around 0.9 signals due to accidental background are expected per day. Furthermore, alpha particles resulting from the radioactivity of uranium (U) and thorium (Th) in the earth can react with the liquid scintillator, leading to a correlated background with a rate of 0.01 d^{-1} to 0.05 d^{-1}. Also, the radioactive decays of U and Th produce antineutrinos, which consitute themselves as the geo-neutrino flux. The expected rate of geo-neutrino induced signals is 1.5 d^{-1} in average. Additionally, cosmic muons can interact with ^{12}C atoms in the liquid scintillator and create cosmogenic isotopes such as ^{8}He and ^{9}Li. Both of these isotopes are β^{-}-emitters ($n \rightarrow p + e^{-} + \overline{\nu}_e$) that can also exhibit daughter nuclei with neutron-unstable excited states. The branching ratios for ^{8}He and ^{9}Li to neutron unstable states in ^{8}Li and ^{9}Be are 16 % and 51 % respectively [Bel+13]. A photon is released after the consequently emitted neutron is captured mainly on hydrogen after approximately 260 μs. Combined with the photons which are created due to the interaction of the electron from the beta decay with the liquid scintillator, this mimics the signal of an anti neutrino, causing an expected background rate of approximately 1.6 d^{-1}. In JUNO, muons are partly shielded by the overburden of the detector and their signals are vetoed.

The experimental site shown in figure 2.2 is located underground in Jinji Town, Kaiping City in the Greater Jiangmen Region in China with a total overburden of roughly 700 m, which corresponds to a meter water equivalent (MWE) of around 2000 m [Str+15]. It is roughly 53 km away from the six-core Yangjiang nuclear power plant and the currently built four-core Taishan plant. The total combined thermal power of the two power plants amounts to 35.73 GW. Roughly 2.8 % of the antineutrino events will be contributed by the Daya Bay nuclear power plant complex, which is located 215 km eastwards of the JUNO site.

The JUNO detector consists of three main parts: A central detector, a cherenkov detector and a muon tracker (see figure 2.1). The central detector is comprised of an inner vessel with a diameter of 35.4 m and a stainless steel latticed shell with a diameter of 37.5 m. Inside the inner vessel 20 kt of Linear Alkyl-Benzyne (LAB) liquid scintillator are located. Added to the liquid scintillator are 3 $g\,L^{-1}$ 2.5-diphenyloxazole (PPO) as the flour and 15 $mg\,L^{-1}$ of bis-MSB as a wavelength shifter that improves the PMT's sensitivity. Special techniques are used to regularly purify the liquid scintillator material. On a stainless steel latticed shell 18 000 photomultiplier tubes with a diameter of 20 inches will be mounted and protected against cascaded implosion through acrylic covers. The PMTs will be partly manufactured by Hamamatsu and Northern Night Vision Technology (NNVT). They are planned to have a quantum

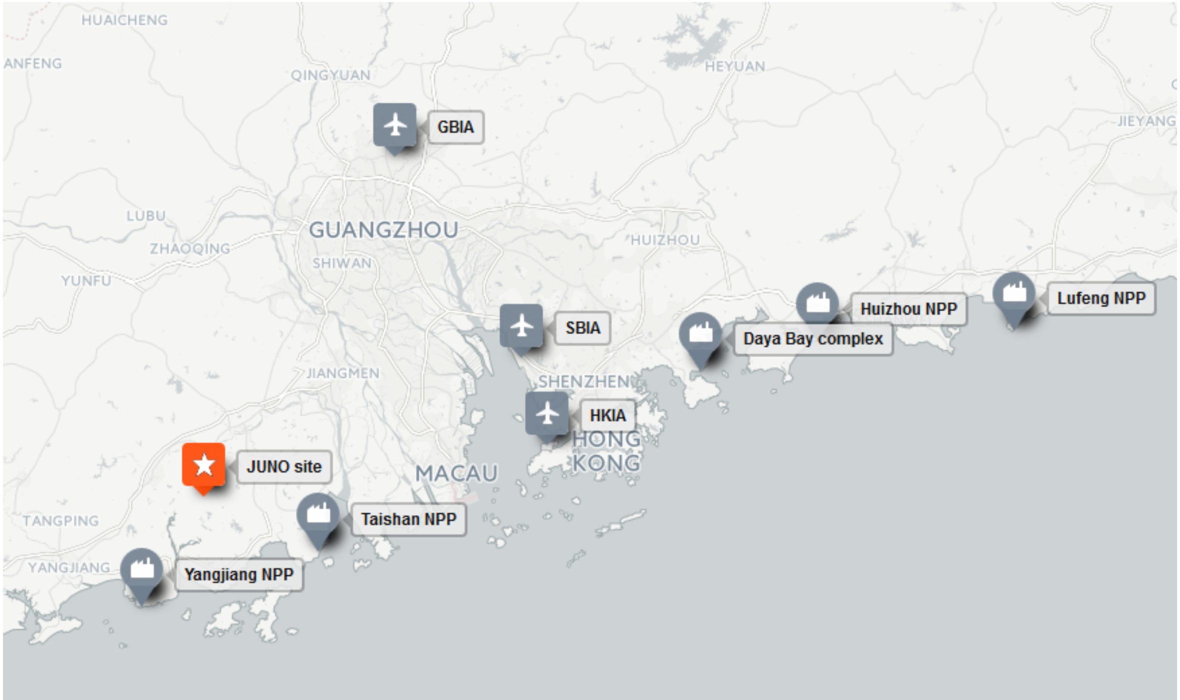

Figure 2.2.: Location of the JUNO site (orange) as well as the surrounding nuclear power plants (NPPs). The Huizhou and Lufeng plants are currently in the planning stage. Also shown on the map are the locations of the three nearest main airports: Hong Kong Intl. Airport (HKIA), Shenzhen Baoan Intl. Airport (SBIA) and Guangzhou Baiyun Intl. Airport (GBIA).
Source: OSM Positron (Carto) Map tiles by CartoDB under CC BY 3.0. Map data ©OpenStreetMap contributors under ODbL.

efficiency of $\eta > 35\,\%$ and will yield an energy resolution of 3 % at 1 MeV [Gra16], which is required to resolve the subdominant oscillation pattern from figure 1.3. Depending on the final design, the photocathode coverage will range from 75 % to 78 %. Gaps between the 20-inch PMTs are filled with up to 36 000 smaller Hamamatsu 3-inch PMTs further refining the energy and vertex resolution by increasing the time resolution. Mu-metal cages around each of the photomultipliers as well as various coils around the whole detector might be used to shield the PMTs from the terrestrial magnetic field. Currently, the specific technical realisation of constructing the central detector is being discussed.

A cylindrical tank encloses the central detector with a clearance of at least 2 m between the tank itself and the latticed shell supporting the PMTs. The tank is filled with 20 kt of pure water shielding the detector from the surrounding rocks radioactivity. It also is a part of the cherenkov detector tagging cosmic muons. This cherenkov detector consists of 1600 Veto-photomultipliers ($\varnothing$: 20 inches), also manufactured by Hamamatsu and NNVT. Additionally, the tracker elements from the dismantled OPERA project [Ada+07] will be used, resulting in an expected muon detection efficiency of 99.8 % in total. They are planned to be read out by a Hamamatsu 64-channel multi-anode PMT. The detector will be calibrated and accessed via a shielded chimney reaching to the surface.

2.2. Auxiliary goals

Beside the determination of the mass hierarchy of neutrinos, JUNO might serve several other neutrino related goals. While so far the heat flow of the earth's surface could be determined, the question how this heat is produced still remains to be answered. The heat balance of the earth depends on the decay energy of natural radio isotopes. Via the measurement of geoneutrinos, the amount and the isotope abundance of natural radio isotopes, which are important to assess the radiogenic heating of the earth, can be determined. Here, JUNO will reduce the errors of existing geoneutrino measurements and thus improve estimations of the radiogenic heating in the earth [Uni15].

Another aspect JUNO might help to resolve lies within supernovae. If a star dies in a core-collapse supernova, it releases 99 % of its energy in the form of neutrinos. Given a typical stellar distance of 10 kpc, JUNO would register around 5000 neutrino events in a very short period of time. The temporal progress, energy spectrum and the flavour composition of these signals can deliver important information about the mechanisms of supernovae. Also, knowledge about the diffuse supernova neutrino background (DNSB), i.e. the integrated neutrino flux coming from past core-collapse events, might by acquired by JUNO.

Atmospheric neutrinos are created due to cosmic ray interactions or the decay of pions and kaons in the earth's atmosphere. It is known that the ratio of atmospheric electron and muon neutrinos depends on the path length covered inside the earth. This can be explained by neutrino oscillations. With JUNO it could thus be possible to determine the mass hierarchy via the detection of atmospheric neutrinos, albeit with a small significance of 1σ due to JUNO's comparatively small mass. Nevertheless the determination of the mass hierarchy via atmospheric neutrinos is a complementary method that may increase the total significance of JUNO's mass hierarchy measurements.

Furthermore, JUNO might help in detecting sterile neutrinos, which are hypothetical gauge singlets of the Standard Model. Especially information about light sterile neutrinos, which are candidates for Warm Dark Matter [Kus09], might be gathered.

Besides, data about nucleon decay can be taken with JUNO. The detectors location makes it well suited for the detection of the decay of nuclei. Here, the prime decay channel is the SUSY (supersymmetry) favoured proton decay, where a proton decays into a kaon K^+ and an anti-neutrino ($p \rightarrow K^+ + \overline{\nu}$). More detailed investigations can give some information about the asymmetry between matter and antimatter.

2.3. Contribution of the University Hamburg

As of now, more than 70 universities are involved in the JUNO project, including six major German Universities and research centres. The University of Hamburg mainly focuses on two aspects.

The first main focus is the development of software allowing three-dimensional topological reconstructions in liquid scintillators. Specifically, the target here lies within the reconstruction of 3D high- and low-energy events.

The second main focus, to which this thesis contributes, lies within the development of an automated photomultiplier test stand. Due to the high quality requirements in terms of the sensitivity of the JUNO PMTs, all of them will be tested and calibrated utilising an automated testing system. Among other parameters, the testing includes determining the photo detection efficiency (PDE) and the dark count rate (DCR) of the PMTs (for a more detailed explanation of the PDE and DCR see chapter 3). Furthermore, the afterpulsing and pulse form characteristics of the PMTs will be analysed. For the 20-inch PMTs, this test system will consist of four shipping containers, each of which will hold 36 photomultipliers encased in aluminium drawers, as shown in figure 2.3. Readout electronics for the PMTs will be provided and developed by the Eberhard Karls University Tübingen.

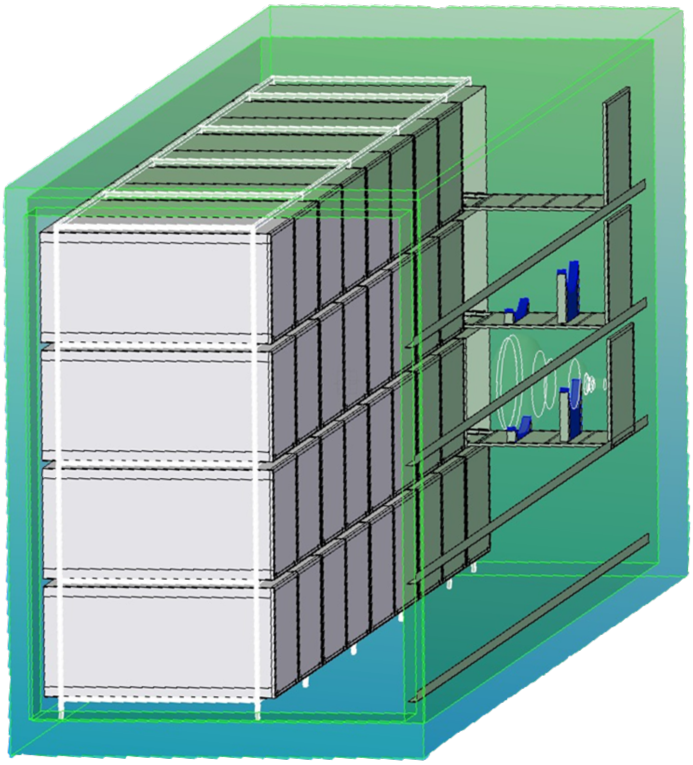

Figure 2.3.: Schematic view of the interior of the test stand. The PMTs will be placed in 36 aluminium drawers that are arranged in four stacked rows with nine drawers each.

3 Photomultiplication

The principle of photo detection is applied in many areas of technology. In the spectral range of photonics mostly quantum detectors are used. These photo detector types use the photoeffect to convert a photon into a charge carrier. The difficulty here is that low numbers of photons are hard to detect, as it is the case in single photon events. For this purpose, photomultipliers (PMs) are used. While there are many different types (e.g. silicon PMs, avalanche photodiodes) of photomultipliers, the following chapter gives an overview of photomultiplier tubes (PMTs), as such devices will be used in the JUNO project. Section 3.1 describes the working principle and the key parameters of a PMT. In sections 3.2 and 3.3, the influence of magnetic fields and the temperature on PMTs are outlined.

3.1. Working principle and key parameters of PMTs

Photomultiplier tubes (PMTs) generally consist of an evacuated glass tube containing a photo cathode, an anode and an electron multiplier. Two main designs can be distinguished: Side-on PMTs and head-on PMTs. In case of the side-on design, incident photons pass through a specific spot on the side of the tube and impinge an opaque cathode. Figure 3.1 schematically shows a PMT with the head-on design where the light field enters the top of the tube upon striking the photo cathode. The photomultiplier tubes used within the scope of this thesis as well as the ones planned to be used in JUNO are of the head-on design.

In any case, incoming photons striking the photo cathode release electrons due to the photoelectric effect. These photoelectrons are accelerated by an electric field and directed to the electron multiplier. This multiplier consists of multiple electrodes, so called *dynodes*. Photoelectrons that are accelerated towards the first dynode release multiple secondary electrons upon striking it. Due to the dynodes being held consecutively at a higher potential (mostly around 100 V) using a series of voltage dividers, each secondary electron can release several

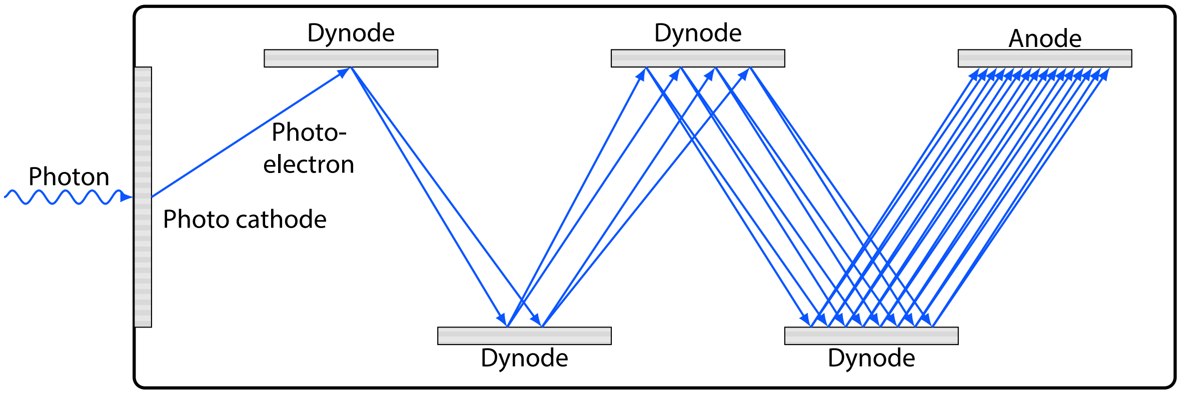

Figure 3.1.: A schematic representation of the most essential parts of a photomultiplier tube. Photons striking the cathode release photoelectrons which are accelerated by an electric field and hit dynodes, where additional photoelectrons are released. This leads to a multiplication of electrons making single photons detectable.

electrons upon striking the next dynode. Collectively, this leads to an exponential increase of secondary electrons, which are collected at the anode. Using an analogue to digital converted (ADC), the PMT signal can be digitised. A typical PMT spectrum is depicted in figure 3.2. Here, the pedestal, i.e. the noise (channel 45), a single photoelectron peak (channel 70) and a smaller two photo electron peak (channel 110) can be seen [Bri+13].

The amplification factor of the secondary electrons caused by the dynodes is called *gain*. Quantitatively, the gain can be calculated using the *secondary emission coefficient* δ_i of the dynodes, which is dependent on the voltage V:

$$\mathcal{G}(V) = \prod_{i=1}^{n} \delta_i(V). \tag{3.1}$$

The secondary emission coefficient describes the ratio of the number of released electrons to the number of incident electrons and depends on the applied voltage. Under the assumption that all dynodes have the same emission coefficient, equation (3.1) simplifies to

$$\mathcal{G}(V) = \delta^n(V). \tag{3.2}$$

Most photomultiplier tubes are equipped with $n = 10$ to $n = 12$ dynodes. Assuming that each dynode releases roughly four electrons per incident electron, this results in a typical gain of

$$\mathcal{G}(V) \geqslant 10^6. \tag{3.3}$$

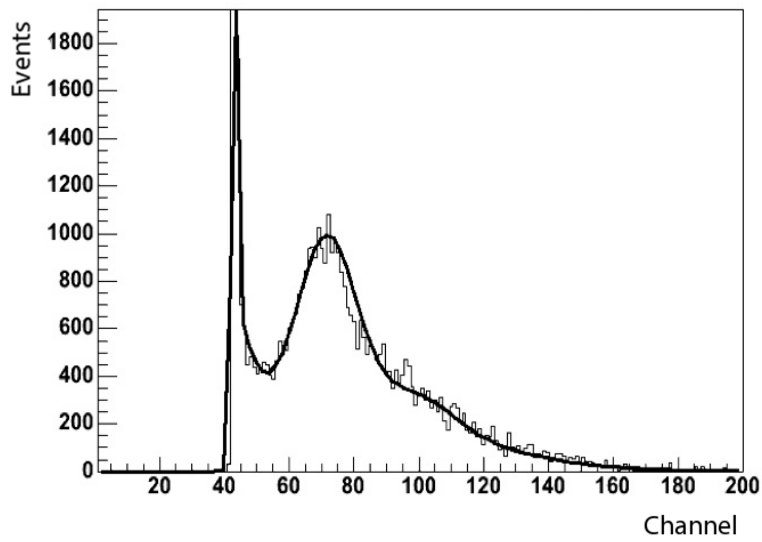

Figure 3.2.: A typical PMT spectrum showing the pedestal, a single photo electron peak and a smaller two photo electron peak. Source: [Bri+13]

Another key performance indicator of a PMT is its *quantum efficiency* $\eta(\lambda)$. The quantum efficiency (QE) is defined as the ratio of the emitted photoelectrons at the cathode to the number of incident photons. An increase of the quantum efficiency is usually observed for photons with shorter wavelengths λ, as these have a higher energy and thus a higher probability to release an electron from the cathodes material than photons with greater wavelengths. Figure 3.3 shows a characteristic curve form of the quantum efficiency as a function of the wavelength. Here, a peak of the QE at short wavelengths of around 400 nm is discernible. For wavelengths shorter than 400 nm, the quantum efficiency drops again. This is due to the fact that for such wavelengths an increasing number of photons is no longer able reach the cathode, as more of them are absorbed by the PMT's glass. For longer wavelengths the quantum efficiency drops rapidly due to the photons not having sufficient energy to overcome the work force of the cathode's material.

With the quantum efficiency, the overall *photon detection efficiency* ψ (PDE) can be determined. It describes the number of output pulses compared to the number of incidence photons and is given by

$$\psi(\lambda) = \alpha\eta(\lambda). \tag{3.4}$$

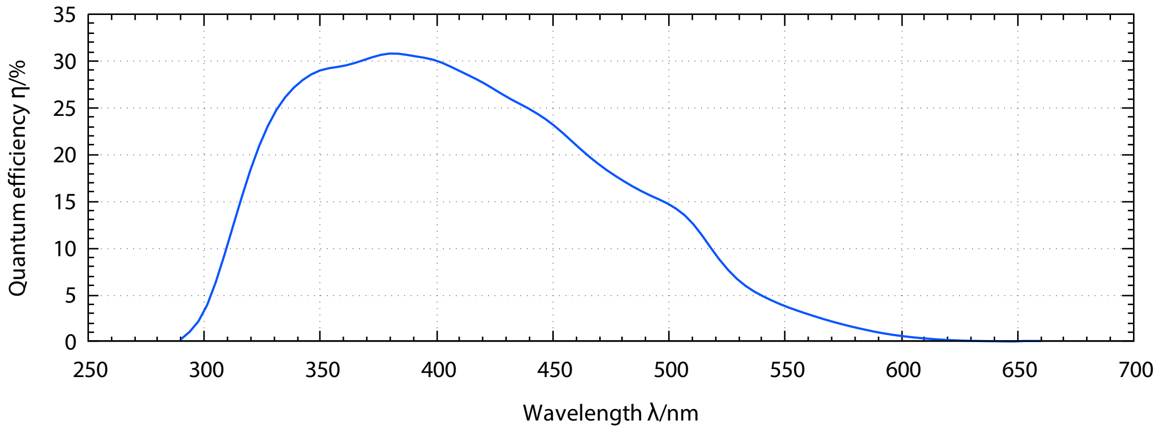

Figure 3.3.: The quantum efficiency η depending on the wavelength λ of a Hamamatsu R12860 HQE 20-inch PMT. Source: Own compilation based on the data in the manufacturers test sheet [HAM15].

Here, α is the collection efficiency. It describes the probability of a photoelectron released from the cathode impinging on the first dynode and thus contributing to the gain [HAM07].

In many applications ultra fast and highly sensitive photomultiplier tubes are required. In these cases, *microchannel plate* (MCP) PMTs are preferred. As the name suggests, an MCP-PMT uses a microchannel plate instead of a set of discrete dynodes. Figure 3.4a schematically shows an MCP. It is a thin disk that consists of a multitude of glass capillaries, so called *channels*, that are aligned parallel to each other. Each channel has an inner diameter of 6 µm to 20 µm [HAM07]. In figure 3.4b, the cross section of a channel is depicted schematically. A voltage V is applied across the MCP. When a photon impinges the input electrode, it releases multiple secondary electrons from the material of the channel's interior. This material is designed to provide the correct secondary emissive properties. The released photoelectrons are accelerated due to the voltage V, thus releasing more electrons after striking the channel again. This process is repeated along the whole channel resulting in an exponential increase of secondary electrons similar to what happens at a multi-dynode structure of a more conventional PMT design.

In large detector systems like JUNO, photomultiplier tubes are coupled to *scintillators*. A scintillator is a medium, that is excited by impinging photons or charged particles. The energy excess that is added to the scintillator molecules via particle collisions results in the emittance of photons, which can be detected via PMTs. This way, photomultipliers can be used to detect ionising radiation. Photomultipliers can also be coupled with Cherenkov-emitters like pure

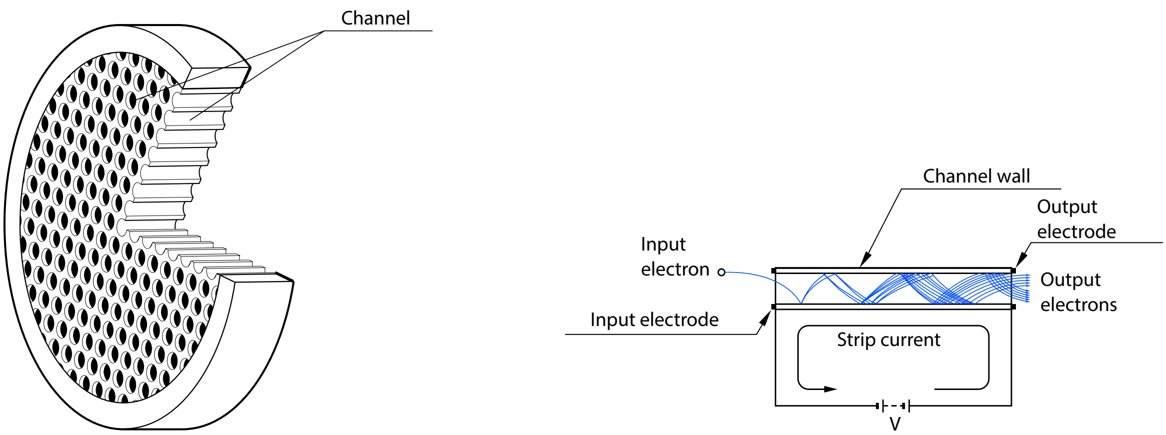

(a) Microchannel plate. **(b)** Cross section of an MCP channel.

Figure 3.4.: Schematic view of both a microchannel plate (MCP) and an MCP channel. Source: [HAM07]

water. Such media emit electromagnetic radiation, should a charged particle (e.g. a muon) pass through them at a speed greater than the speed of light in this medium.

3.2. Influence of magnetic fields on PMTs

Photomultiplier tubes are greatly affected by external magnetic fields. While photoelectrons travel inside the PMT, they experience the Lorentz force, which, for a point-like particle with the charge q and the velocity v, is given by:

$$F_\mathrm{L} = qvB\sin\theta. \tag{3.5}$$

Here, B is the magnetic field strength and θ the angle between the particles direction of propagation and the direction of the magnetic field. This force acts on the electrons that are released from the cathode and travel to the first dynode. It results in a deflection of these electrons, which consequently reduces the dynode collection efficiency α and thus the gain as well as the photon detection efficiency (see equation (3.4)). According to Bein [Bei16], the deflection of a single electron can be derived from equation (3.5) to be:

$$z = \frac{1}{3}\frac{eBR^2}{m_\mathrm{e}}\left(\frac{2m_\mathrm{e}}{Ve}\right)^{\frac{1}{2}}. \tag{3.6}$$

Here, R is the radius of the PMT, V the acceleration voltage, $e = 1.6 \times 10^{-19}$ C the elementary charge and $m_e = 9.1 \times 10^{-31}$ kg the mass of an electron [Kuc14]. Assuming a magnetic field of 49 µT and a voltage of $V = 700$ V, this yields a theoretical deflection of approximately 2.4 cm for a 20-inch PMT like the ones used in JUNO. The force caused by the external magnetic field has an especially large influence on large area PMTs, as they have a much longer distance between the cathode and the dynode. Depending on the orientation of the PMT and the magnetic field, the electrons between dynodes might also be affected significantly by the magnetic field.

Aiello *et.al* [Aie+12] have thoroughly examined the effect of the the earth's magnetic field on 8-inch and 10-inch Hamamatsu PMTs. Besides other characteristics, they analysed the photo detection efficiency ψ and the gain $\mathcal{G}$. Depending on the orientation, the photo detection efficiency varied by up to 40 % and 29 % for the 10-inch and 8-inch PMTs respectively. The gain of the larger PMT varied by 29 %, the one of the smaller PMT by 7 %. Using a passive magnetic shielding, the variations could be significantly reduced, in most cases to less than a half.

Such variations in gain and photo detection efficiency severely affect the performance of a PMT. It is thus necessary to not only shield the JUNO detector from external magnetic fields, but also the JUNO test stands as these will be used to test and calibrate the required PMTs. The JUNO test stand is equipped with a passive soft-iron shielding whose performance will be evaluated in chapter 5.

3.3. Influence of temperature on PMTs

Due to photomultiplier tubes being based on photoemitting materials, they are, to a certain degree, temperature dependent. This temperature dependency may affect the pulse shape, anode and cathode sensitivities, the gain and the dark count rate, which is the average number of registered counts without any incident photons, of the device. The influence of the temperature on the components of a PMT is a deeply complex matter and highly reliant on the specific materials as well as the PMT design. Without specific research dedicated to the temperature dependency of a certain photomultiplier, only tendencies and averages can be identified.

To begin with, the cathode and anode sensitivities of a PMT change with the temperature. For wavelengths ranging from the ultraviolet to the visible region, the sensitivity $\mathcal{S}(T)$ of the electrodes usually has a negative temperature coefficient $\alpha_{\mathcal{S}(T)}$. The sensitivity depends on the temperature coefficient as follows:

$$\mathcal{S}(T) = \mathcal{S}(T_0)\left[1 + \alpha_{\mathcal{S}(T)}(T - T_0)\right]. \tag{3.7}$$

Here, $\mathcal{S}(T_0)$ is the sensitivity at the reference temperature T_0. Depending on the material, the temperature coefficient $\alpha_{\mathcal{S}(T)}$ ranges roughly from $-0.5\,\%\,°\mathrm{C}^{-1}$ to $-0.2\,\%\,°\mathrm{C}^{-1}$. For long wavelengths, especially near the maximum detectable wavelength of the device, the temperature coefficient is usually positive, reaching up to $0.6\,\%\,°\mathrm{C}^{-1}$ for multialkali cathodes [HAM98].

Furthermore, the emission of the dynodes can change with temperature, resulting in a change of the gain. As for the anode and cathode, the temperature coefficient for the dynodes depends mainly on their material. According to Flyckt and Marmonier [FM02], their temperature coefficient is commonly negative, ranging from $-0.1\,\%\,°\mathrm{C}^{-1}$ to $-1\,\%\,°\mathrm{C}^{-1}$.

Also, the dark count rate is influenced by temperature changes. The dark count rate is mainly caused by electrons created due to to thermal excitation of the material and is often described through the dark current, which follows Richardson's law [Kuc14]:

$$J = aT^2 \exp\left(-\frac{W_{\mathrm{th}}}{k_{\mathrm{B}}T}\right). \tag{3.8}$$

Here, J is the current density, T the temperature, $k_{\mathrm{B}} = 1.38 \times 10^{-23}\,\mathrm{J\,K^{-1}}$ the Boltzmann constant, W_{th} the work function and a the Richardson constant. According to Dushman [Dus23], the Richardson constant can be estimated to be $a = 4\pi k_{\mathrm{B}} e h^{-3} \simeq 1.2 \times 10^{6}\,\mathrm{A\,m^{-2}\,K^{-2}}$, where $e = 1.6 \times 10^{-19}\,\mathrm{C}$ is the elementary charge and $h = 6.63 \times 10^{-34}\,\mathrm{J\,s}$ the Planck constant [Kuc14]. Equation (3.8) shows that the thermal emission increases exponentially with the temperature.

The JUNO site is located near the transition of the subtropical and the tropical climate zones, meaning that annual mean temperatures of 12 °C to 24 °C are expected [MM12]. Temperature fluctuations between day and night can be greater than 10 °C. Temperature changes of 10 °C could reduce the sensitivity of the PMT's electrodes by up to 5 % and the sensitivity of the dynodes by up to 10 %. The resulting variation in gain combined with the change of the dark current from equation (3.8) can render the PMT's test and calibration results uncomparable. Additionally, the readout electronics for the PMTs will require approximately 0.5 MW during operation, creating additional waste heat. In order to acquire comparable results when testing and calibrating the PMTs, fluctuations in temperature need to be diminished and the temperature has to be monitored constantly. Within the scope of this thesis, a temperature monitoring system for the JUNO test stand is developed (see chapter 6). Additionally, the JUNO test stand is equipped with an air conditioning and heating unit, for which a remote control system is implemented (see chapter 7).

Part II

Commissioning of a test facility

The photomultiplier tubes for the JUNO project have to be tested thoroughly due to the high quality requirements. For the 20-inch PMTs this is done using shipping containers that are fitted with a passive magnetic shielding in order to minimise the effect of the earth's magnetic field on the PMTs, which was shortly discussed in the previous part (see section 3.2). The influence of the temperature on the photomultipliers (see section 3.3) is minimised utilising a Heating, Ventilation and Air Conditioning (HVAC) unit.

In the first chapter of this part, chapter 4, various measurements with two small test stands located in a laboratory of the Hamburg University are described. These smaller testing rigs target to reproduce the conditions that will prevail in the JUNO mass test stands. The commissioning of these mass test stands is covered in the subsequent three chapters. Chapter 5 gives an overview of the performance of the test facility's magnetic shielding. In chapter 6, various different attempts to implement a temperature monitoring system for the HVAC unit are outlined. The final design including its LabView integration are explained comprehensively. Conclusively, chapter 7 outlines the remote control system that allows to change and read the parameters of the HVAC unit.

4 Small laboratory test stands

The Institute of Experimental Physics of the Hamburg University is currently equipped with two small test stands. The test stands provide an environment in which photomultiplier tubes can be tested and analysed under controlled conditions. In particular, they aim to reproduce the conditions at which the JUNO PMTs will be tested in the mass test stands. For this purpose, lightproofness, a controllable light source and shielding against external magnetic fields are relevant aspects. Also, the test stands can be used to give information about the performance of the electronic components used to read out the PMTs. In sections 4.1 and 4.2, an overview of the two small test stands is given. Within the scope of this thesis, dark count measurements at both test stands were performed. These are described in section 4.3. Furthermore, coincidence measurements were performed. These are explained in section 4.4.

4.1. Optical test stand

The first, optical test stand is a wooden box with outside dimensions of 179.5 cm×62 cm×66 cm (width × height × depth), as schematically shown in figure 4.1. It can be opened using a hinged top lid. To ensure lightproofness at the gap between the main body and the top lid, both parts are padded with a rubberised inlay. Additionally, a black light tight PVC foil is superimposed.

The optical test stand does not feature active or passive shielding from the earth's magnetic field. It is mainly used for testing the electronics and examining single- and multi-photon events and designed to facilitate PMTs with a diameter of up to 18 inches. Within the scope of this thesis, measurements with a 2-inch R1828-01 Hamamatsu PMT were performed with this test stand. A light source is implemented utilising a light emitting diode (LED) with a wavelength of 420 nm. Through an optical setup, the light emitted by the LED can be channelled onto the PMT. However, this optical setup was not used for the measurements performed in

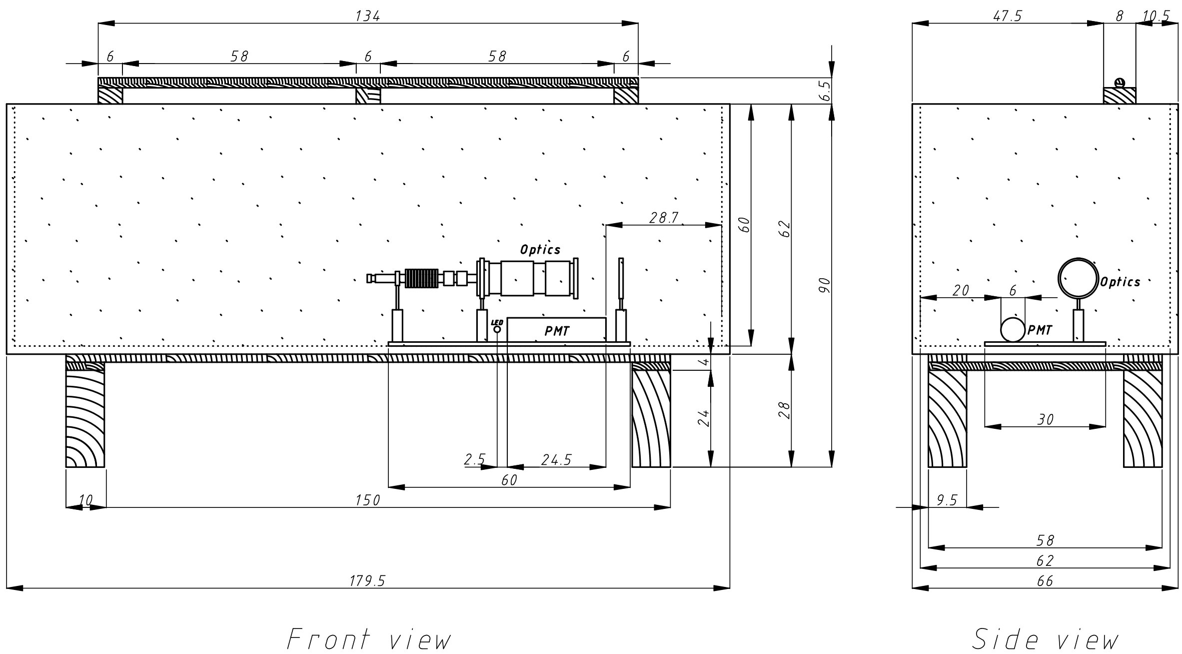

Figure 4.1.: Schematic 2-dimensional representation of the optical test stand. The test stand consists of a wooden box placed on a wooden support structure. The hinged top can be opened via a wooden handle and be securely closed by metal clasps (not depicted). Connections for the PMTs are on the back side. A PVC foil (not depicted) is superimposed to ensure lightproofness. All length specifications are in cm.

the course of this thesis. The connectors for the high voltage, the PMT output signal and the LED are located on the back side of the rig.

Due to its size, this test stand cannot fit the 20-inch photomultipliers that need testing for the JUNO project. Instead of modifying this existing testing rig, another different test stand was designed in [Bei16].

4.2. Zero-*B* test stand

The second test stand available is sketched in figure 4.2. The Zero-*B* test stand is designed to hold the large 20-inch PMTs for the JUNO experiment including their structural mounting hardware. This testing rig features a two metre long tube made out of laminated paper that is suspended by polyvinyl chloride (PVC) belts in a metal scaffold. The inside diameter of the testing rig is 0.8 m. A pair of two wooden disks with clamps allows the test stand to be closed on either side. They are also an important part of the structural integrity of the rig as they mitigate material warping over time. As for the first test stand, the lightproofness is secured through the application of black PVC foils on either side that are held on by elastic rings. The Zero-*B* test stand can be equipped with the same LED as the optical test stand. Connections for the high voltage and the PMT's output signal are located on either end of the tube.

The Zero-*B* test stand is especially constructed with magnetic shielding in mind. It is wrapped 34 times with 40-wire ribbon cable [3M 10]. This effectively creates a coil with 1360 windings, allowing for an active shielding of the magnetic field. Using this active shielding, the terrestrial magnetic field can be either completely suppressed or amplified to up to 160 µT [Bei16]. It has to be noted that for a proper shielding the test stand has to be properly aligned so that it opposes the magnetic field. One difficulty here is that the magnetic field in Hamburg has an inclination of roughly 60° in relation to the horizontal plane. Currently, the Zero-*B* test stand is not appropriately aligned with the earth's magnetic field.

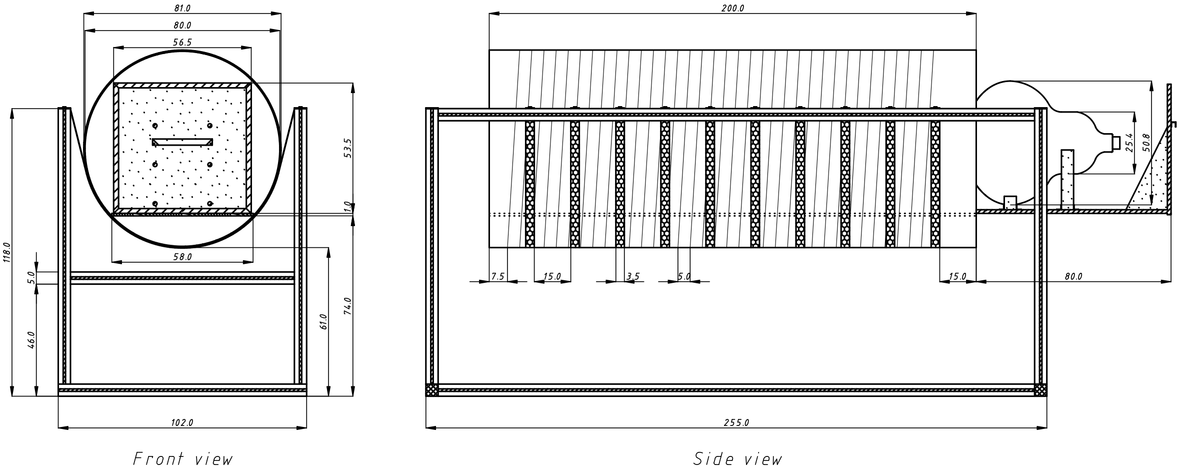

Figure 4.2.: Schematic 2-dimensional representation of the Zero-*B* test stand. It consists of a laminated paper tube that is supported by a metal scaffold and wrapped with ribbon cable. During measurements, the PMT is placed in a drawer on a wooden board located inside the tube. It is closed on either side using a wooden disk with metal clamps (not depicted). A PVC foil (not depicted) ensures lightproofness. The depicted Hamamatsu R12860 PMT is modelled according to the manufacturers length specifications [HAM15]. All length specifications are in cm.

4.3. Dark count measurements

As already outlined in section 3.3, PMTs do register signals even without an external light source. This dark count rate mainly results from thermal excitation of electrons in the PMT's cathode. To begin with, dark count measurements were performed with both small test stands. Dark count measurements are highly important as they are necessary to identify the actual signal of the PMT. They were performed in the optical test stand with a 2-inch Hamamatsu R1828-01 PMT first and afterwards in the Zero-B test stand with a Hamamatsu R12860HQE 20-inch PMT. In both cases, the PMTs were given an idle period of one day after installing them in the test stands. This is to ensure that photoelectrons, which were released due to the influence of the ambient light, are no longer a concern.

4.3.1. Readout electronics

The readout electronics for the two photomultipliers are located in a rack nearby the two test stands. The same components that will later be used in the JUNO test stands are, however, not available. Figure 4.4 gives a schematic overview of the rack.

In figure 4.3, the circuit used for the dark count measurements is shown as a block diagram. The photomultiplier tubes are equipped with splitter boxes that allow to connect the high voltage as well as the PMT output signal. The signal of the photomultiplier is fed into an input connection of a LeCroy Mod. 428F Linear Fan IN-Fan OUT module (see figure 4.4, ⑪). This module creates multiple outputs from one input, effectively duplicating the PMT signal. One output of the Fan I/O module is used to display the PMT's signal on an oscilloscope (Tektronix DP0 2024 Digital Phosphor Oscilloscope).

A second output is used to amplify the photomultiplier signal using an Ortec 474 Timing Filter Amp ⑦. This amplifier is needed in order to adjust the signal of the PMT to the range of the analogue to digital converter (ADC).

The amplified signal is then fed into the Gate In connection of a C.a.e.n N957 8K MCA ③. This Multichannel Analyser (MCA) can collect the data from its inputs and convert them into an output signal. Different trigger methods are available for the N957 MCA. In the autogate mode, which was used for the purpose of the dark count measurements, the conversion is enabled by a discriminator with an adjustable threshold and performed as soon as an input signal is registered. The external gate mode utilises a signal fed into the Gate In connection for the conversion and was used for coincidence measurements (see section 4.4). The MCA's output signal is digitised by an internal 13-bit fast ADC and can be read out via the COM-interface. For this, the MCA is connected via USB to a laboratory computer, which also allows to change the trigger method of the MCA. Via a data acquisition (DAQ) program the ADC-signals of the PMT are saved in a `.root` file. Here, the DAQ software also saves the time as well as the ADC value in a separate `tree` structure.

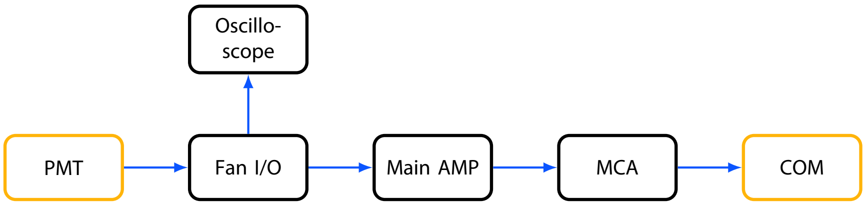

Figure 4.3.: Block diagram illustrating the electronic circuit used to perform the dark count measurements. The PMT signal is duplicated using a Fan-In/Fan-Out module, amplified and via an MCA converted into a digital signal that is recorded by a computer (COM).

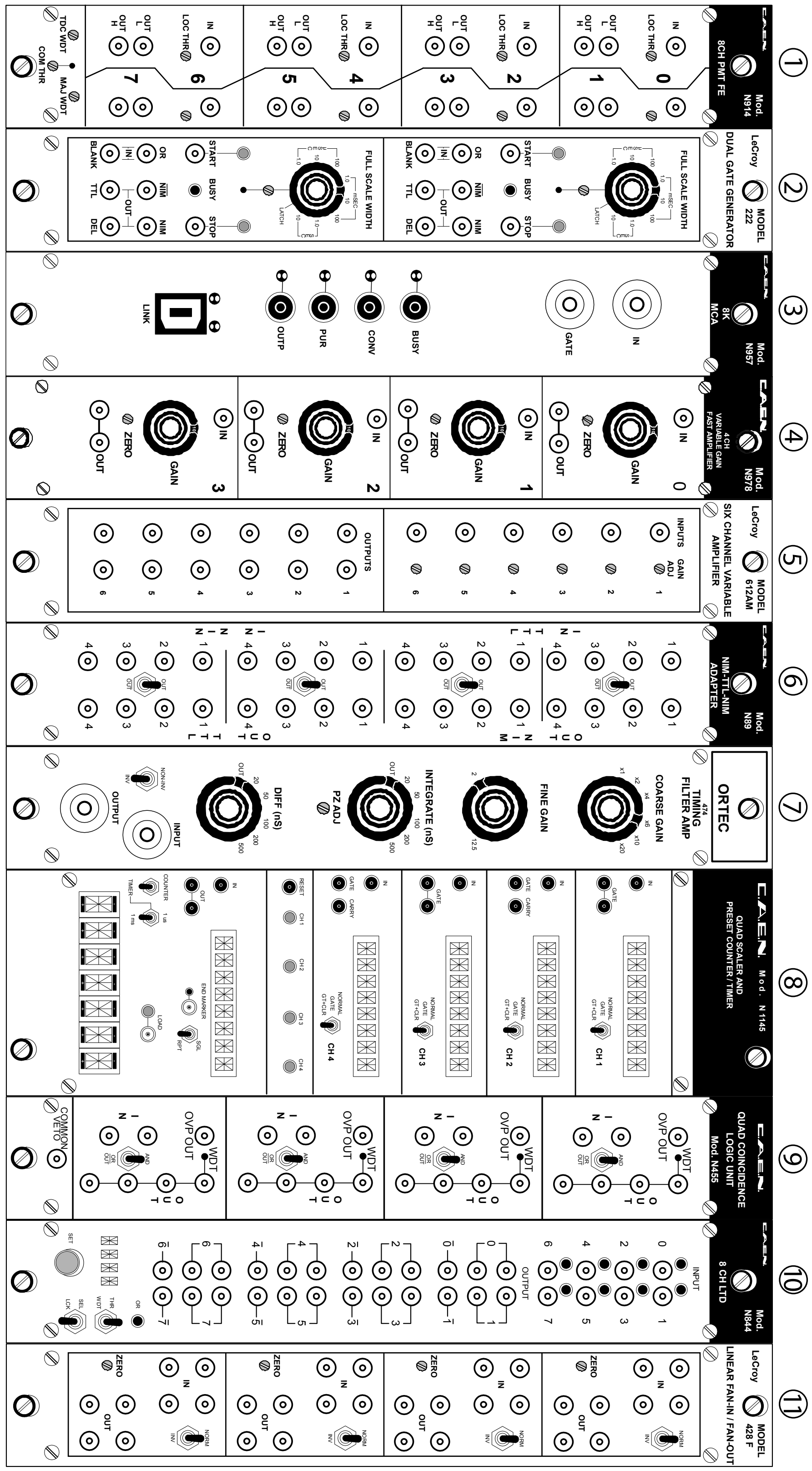

Figure 4.4.: A schematic overview of the available electronic components in the rack to read out the photomultipliers. It consists of a Fan-In/Fan-Out module ⑪, various amplifiers ①④⑤⑦, a discriminator ⑩, a signal converter ⑥, an analogue to digital converter ③, logic units ⑧⑨, and a gate generator ②. Source: Own depiction, partially based on and adapted from [CAE15].

4.3.2. Readout method and results

Dark count measurements using the previously explained circuit were performed with both test stands and two different photomultiplier tubes. In the optical test stand, a 2-inch R1828-01 Hamamatsu PMT was tested at nine different voltages ranging from 1100 V to 2700 V in 200 V steps. The Zero-*B* test stand contained a 20-inch R12860 HQE Hamamatsu PMT. This larger photomultiplier was tested at three different voltages: 1470 V, 1670 V and 1870 V. All measurements were performed for a duration of roughly 22 h. The data in the `.root` file acquired by the DAQ program was analysed and visualised using ROOT (for a short description of ROOT, see appendix B.3). In particular, the ADC signals were normalised on time in order to ensure their comparability.

Figure 4.5 shows the ADC signals for both the 2-inch and the 20-inch Hamamatsu PMTs. The measurements for both PMTs show a peculiar noise behaviour. For the 2-inch PMT it is recognisable that the number of entries increases with the voltage. For all voltages, the ADC signals show various peaks ranging from channels 50 to 300. A clear valley around channel 350 is visible for voltages ranging from 1700 V to 2700 V, followed by a peak in the range from channel 420 to 460. For the three lowest voltages the signal, and thus this peak in particular, is no longer clearly visible. Closer examinations show that the peak between channel 420 and 460 shifts towards higher ADC channels for lower voltages. In the further course, a rise of the signals can be observed, which manifests itself in peaks at channel 2040. Strikingly, this rise cannot be observed for the signal corresponding to 2300 V. Here, the number of events decreases, with a small plateau at channel 2040. However, all signals for 2100 V to 2700 V show another peak at channel 3100. For voltages lower than that, the signals are no longer clearly discernible. Similar to the signals of the small PMT, the signals of the R12860HQE 20-inch PMT show various small peaks at ADC channels 40 to 180. At channel 2000, all signals plateau, which is followed by a bend towards lower event numbers. The signals corresponding to a voltage of 1670 V and 1870 V have another small peak at channel 3200. Here, the signal for 1470 V is no longer discernible.

For none of the observed peaks, a shift towards greater ADC channels with rising voltage can be observed. This indicates that the measured noise originates from the readout electronics and not from the PMT itself. For example, the various peaks between channels 50 to 300 for the small PMT (and between channel 40 to 180 for the larger PMT respectively) might be caused by reflections inside one of the various cables.

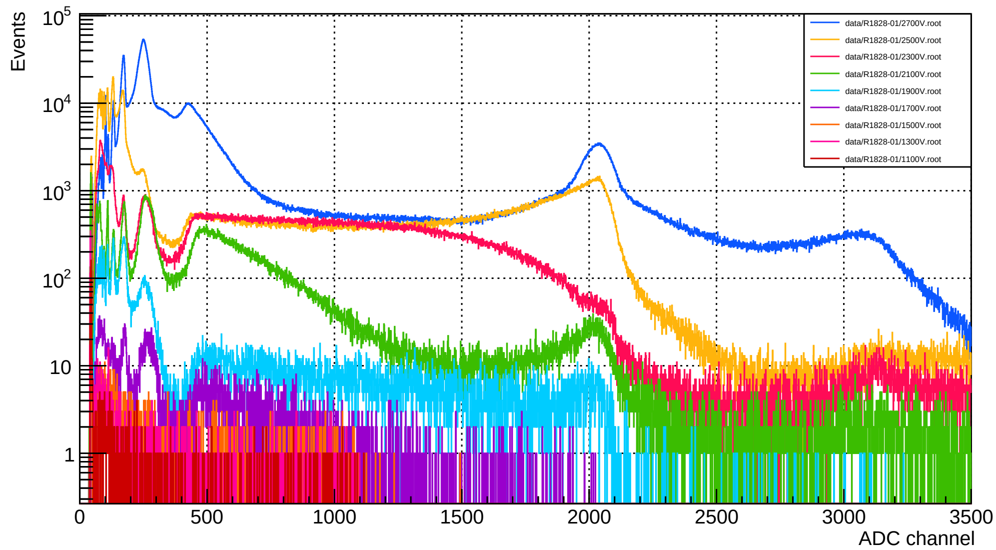

(a) Hamamatsu R1828-01 (⌀: 2 inch).

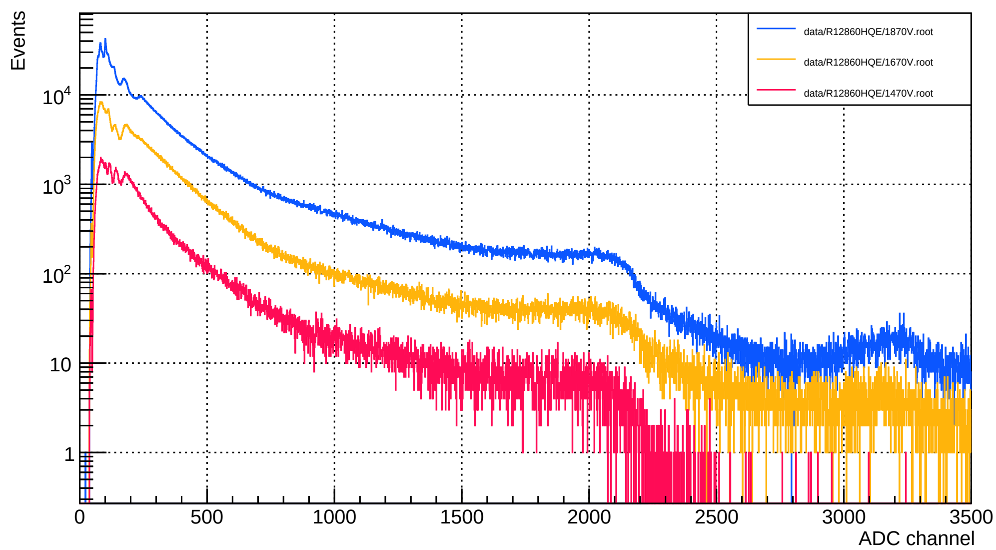

(b) Hamamatsu R12860 HQE (⌀: 20 inch).

Figure 4.5.: Dark count measurements of two different Hamamatsu PMTs. The measurements with the smaller (⌀: 2 inch) R1828-01 PMT were performed in the optical test stand (without the optical setup being used) at nine different voltages ranging from 1100 V to 2700 V in 200 V steps. Measurements with the bigger (⌀: 20 inch) R12860 HQE were performed at 1470 V, 1670 V and 1870 V in the Zero-*B* test stand without the active shielding being turned on. The signals are normed to a measurement duration of 22 h. One thousand channels correspond to approximately 0.2 V.

4.4. Coincidence measurements

A possibility to reduce the noise is to implement a coincidence circuit. In doing so, the PMT is triggered by an LED that is controlled via a function generator allowing to control the pulse frequency as well as the pulse length. This way the LED can be set up to create single photon events. The theory behind this coincidence circuit is that data is taken if, and only if, the PMT detects a signal *and* the function generator generated a pulse.

4.4.1. Readout electronics

As for the dark count measurements, the rack depicted in figure 4.4 was used. Again, the PMT signal is fed into the Fan-In/Fan-Out module ⑪. From there, it is displayed on an oscilloscope and amplified using the ORTEC 474 Timing Filter Amp ⑦. However, the circuitry, which is shown in figure 4.6 as a block diagram, is expanded by a coincidence circuit.

Therefore, another output of the Fan I/O is connected to a C.A.E.N Mod N844 8CH LTD ⑩. This is a Low Threshold Discriminator (LTD), which outputs a signal, should the input signal exceed a certain discriminator threshold. The output signal is of the Nuclear Instrumentation Module (NIM) standard. A NIM signal is a logical zero for 0 V and a logical one for −0.6 V to −1.6 V [AME08]. NIM signals are a standard for negative logic levels, such as the ones provided by a PMT.

A NIM output of the LTD can be used, to display the number of events on a C.A.E.N Mod. N1145 Quad Scaler and Preset Counter Timer ⑧. Another output is connected to the START input of a LeCroy Mod. 222 Dual Gate Generator ②. This unit opens a logical gate when it receives a signal coming from the LTD.

The logical signal coming from the Dual Gate Generator is then fed into an input port of a C.A.E.N Mod N455 Quad Coincidence Logic unit ⑨. Additionally, the signal from the frequency generator that triggers the LED is fed into another input of the coincidence unit. The frequency generator's output signal is a TTL (transitor-transistor logic) type signal. Contrary to the NIM-standard, the TTL-standard defines a standard for positive logic levels. TTL signals are a logical zero for 0 V to 0.4 V and a logical one for 1.5 V to 5 V [AME08]. Because the signal coming from the Dual Gate Generator is a NIM signal, it is necessary to convert the TTL signal of the frequency generator into a NIM signal. This is done using a C.A.E.N Mod. N89 NIM-TTL-NIM Adapter ⑥, which then feeds the NIM signal into the coincidence unit.

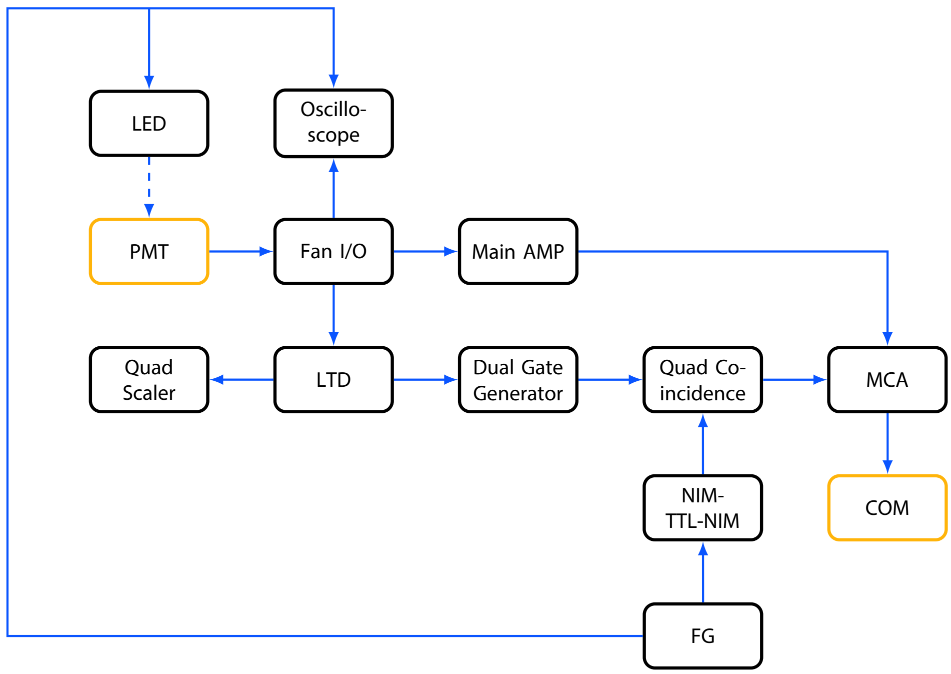

Figure 4.6.: Block diagram illustrating the electronic circuit used to perform the coincidence measurements. A LED controlled by a function generator (FG) creates single photon events. The PMT signal is duplicated and amplified as is the case for the dark count measurements. Additionally, the signal is fed into a discriminator and then into a gate generator that creates a signal for a coincidence unit. This coincidence unit provides a signal to the multi channel analyser, should a signal of the FG exist simultaneously. With this setup, a signal is only digitised if the LED was on and the PMT registered a signal.

The coincidence unit then creates an output signal, depending on the two input signals. In case of an AND setting, both input signals have to be a logical one in order to get an output signal.

The coincidence signal is connected to the Gate In connection of a C.A.E.N N957 8K MCA ③. Using the In connection, this Multichannel Analyser also receives the amplified signal of the PMT. For coincidence measurements, the trigger mode was set to external gate.

4.4.2. Readout methods and results

In total, eight measurements with the 2-inch Hamamatsu R1228-01 PMT were performed at four different voltages (1900 V, 2100 V, 2300 V and 2500 V). For each voltage, one measurement was performed with coincidence, and, for reference, one without. The timespan of data acquisition time was approximately 22 h each. The taken ADC data was processed and normalised with ROOT, similar to the dark count measurements. Figures 4.7 and 4.8 show the ADC signals at the four voltages.

It is recognisable that for both trigger modes the number of entries increases with the voltage. For the measurements with coincidence, all histograms have a peak around ADC channel 70. Both the measurements at 2500 V and 2300 V have a small second peak at channel 110. For the measurement at 2500 V a third peak at channel 135 is discernible. At 2300 V, a third peak is visible at channel 140. The measurement at 2100 V shows no discrete peaks but rather two plateaus at ADC channels 110 and 140. For 1900 V the histogram has peaks at channels 155 and 215. Except for the measurement at 2100 V, none of the histograms shows a discernible fourth peak. At 2100 V, a small peak at channel 185 is visible.

The histograms for the coincidence measurement do not correspond to the expected histograms. The observed behaviour contradicts the expectation that an increase of voltage should result in the peaks being shifted towards a higher ADC channel. To some extent, the histograms show the opposite behaviour, as a consideration of the measurements at 1900 V, 2300 V and 2500 V shows that the second peak is shifted towards less ADC channels with an increasing voltage. For further investigations, the number of entries per second for each measurement was determined. These results are shown in table 4.1. They suggest that a part of the setup is malfunctioning. The function generator was set to output a pulse every 2 μs, which corresponds to a pulse rate of 500 000 s^{-1}. Thus, in theory, around 500 000 ADC signals should have been observed assuming a photo detection efficiency of 100 %. However, at

2500 V, only 184.35 entries per second were observed, suggesting that the taken ADC signals do not originate from the LED, but are rather noise. Another unexpected observation is that the initial peaks of the signals with coincidence are roughly two orders of magnitude higher than the initial peaks of the signals without coincidence. At 2300 V, the observed number of entries with coincidence is almost 15 times higher than the number of entries without coincidence (see table 4.1).

The measurement without coincidence behaves similar to the the dark count measurement from figure 4.5a. From ADC channels 50 to 300 the signals have multiple peaks. Around channel 2000, the signals for 1900 V, 2100 V and 2500 V also show a peak. Here, the signal for 2300 V has no discrete peak, but rather a plateau, as is the case for the dark count measurement. Strikingly, an additional peak at channel 1800 is visible for the signal corresponding to a voltage of 2500 V.

The observed behaviour can have multiple reasons. To begin with, the LED might be defective or its pulse width set too short. The pulse width as well as the pulse length could be increased for future measurements or troubleshooting steps. A malfunctioning function generator is unlikely a reason for the expected behaviour, as its output was cross checked using the oscilloscope. In order to verify the proper operability of the LED, it could be checked via an oscilloscope whether the PMT does output a signal. Moreover, coincidence measurements without the LED could give insight about the observed behaviour. Another reason might be that one or more of the gates are delayed. This could lead to the measurements happening when the LED is off. In total, the troubleshooting process turns out to be quite complex and will thus not be further covered within the scope of thesis. It will, however, be covered in more detail in [Ste17].

Table 4.1.: The number of events per second for the measurements with coincidence (external gate) and without coincidence (autogate) depending on the voltage.

Voltage	Entries per second	
	Trigger mode: Autogate	Trigger mode: External gate
1900 V	0.66	2.36
2100 V	3.56	43.86
2300 V	9.31	137.41
2500 V	26.05	184.35

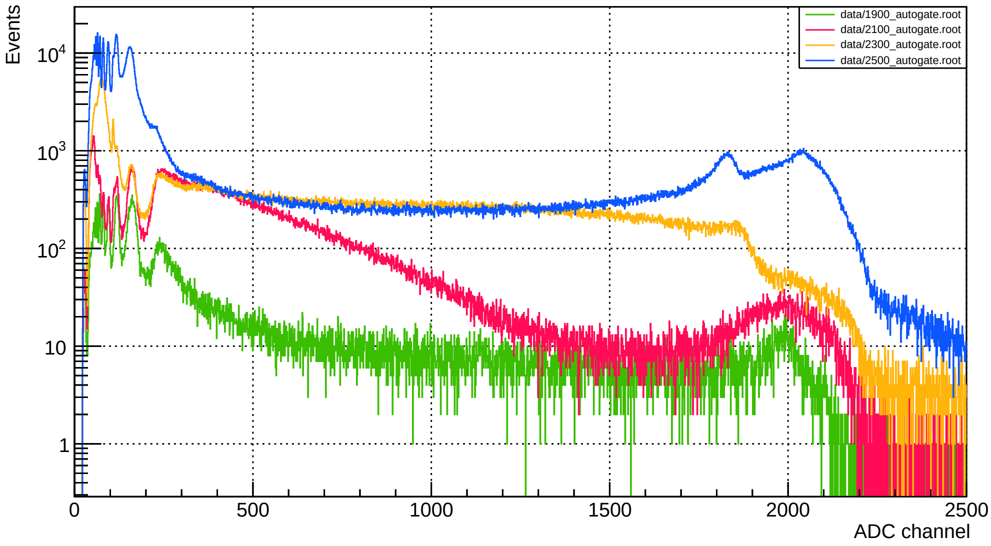

(a) Trigger mode: Autogate (no coincidence).

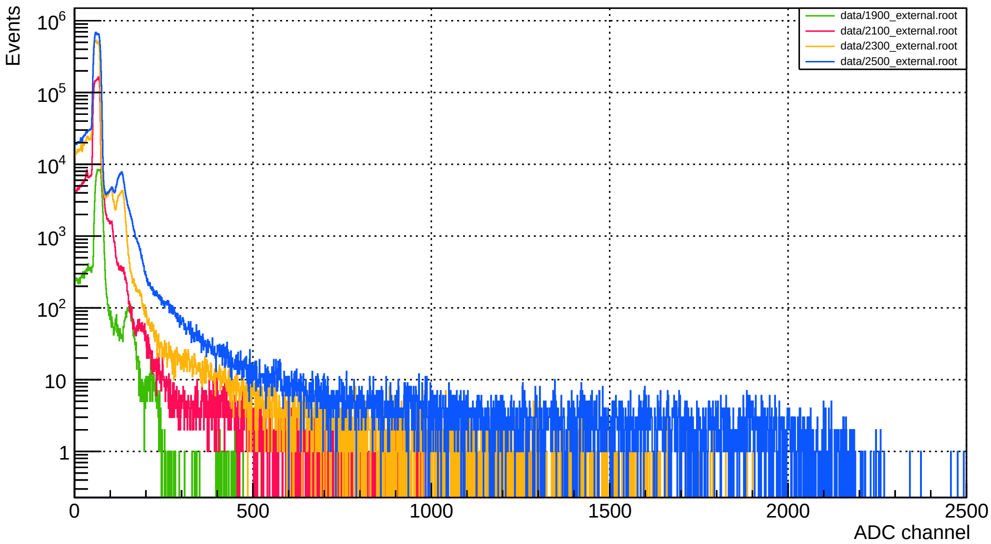

(b) Trigger mode: External Gate (coincidence).

Figure 4.7.: Coincidence measurements (bottom) with a Hamamatsu R1828-01 (⌀: 2 inch) PMT at four different voltages (1900 V, 2100 V, 2300 V, 2500 V). For reference, measurements without coincidence were taken at the same voltages (top). All measurements were performed in the optical test stand without the optical setup being used. The signals are normed to a measurement duration of 22 h. One thousand channels correspond to approximately 0.2 V.

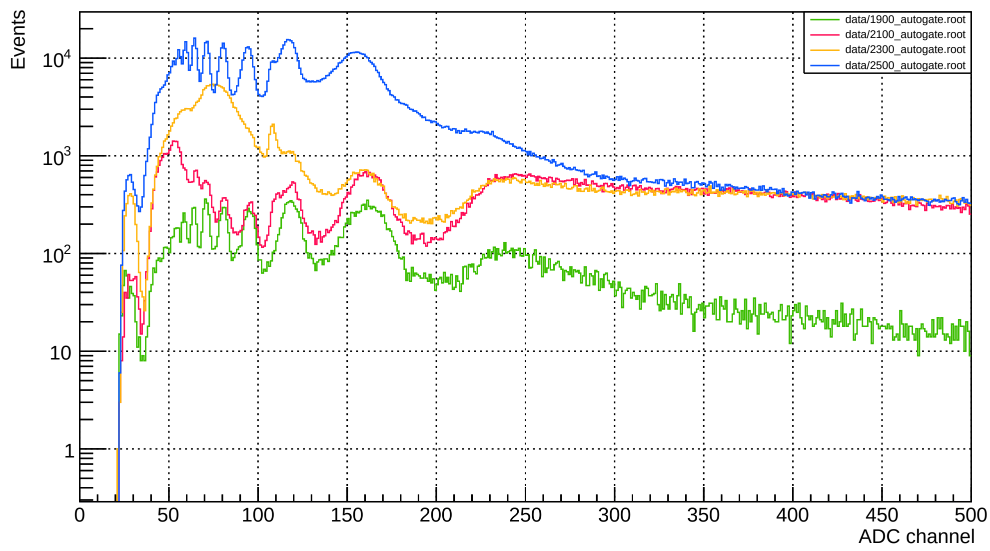

(a) Trigger mode: Autogate (no coincidence).

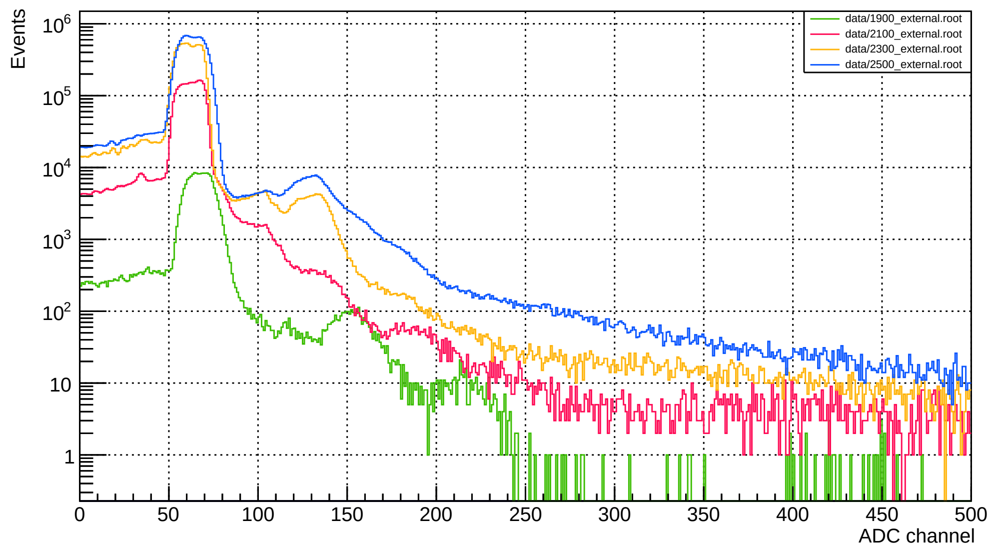

(b) Trigger mode: External Gate (coincidence).

Figure 4.8.: A smaller section (ADC channels 0 to 500) of the measurements with (bottom) and without coincidence (top) shown in figure 4.7. The measurements were performed in the optical test stand with a Hamamatsu R1828-01 (⌀: 2 inch) PMT at four different voltages (1900 V, 2100 V, 2300 V, 2500 V). One thousand channels correspond to approximately 0.2 V.

5 Evaluation of the magnetic field inside the JUNO test facility

The JUNO photomultiplier tubes will be tested and calibrated in a shipping container that is equipped with a Heating, Ventilation and Air Conditioning (HVAC) unit. As described in section 3.2, magnetic fields as weak as the earth's magnetic field can severely affect the performance of a photomultiplier tube. It is therefore necessary to not only shield the JUNO detector, but also the JUNO test stand. In the JUNO detector, various coils around the detector provide an active shielding of the magnetic field. Additionally, each PMT might be shielded passively by enclosing it in a cage made out of *mu-metal* wires, however the planning for this shielding is not yet finalised.

In order to shield the shipping container from the earth's magnetic field, an external firm was commissioned to fit the interior of the container with various alternating layers of *silicon soft iron* and aluminium sheets, providing passive shielding of external magnetic fields. The target of the shielding is a reduction of the earth's magnetic field to less than 10 %, as early studies have shown that such a reduction ensures proper PMT functionality with an ample scope.

Silicon soft iron is a material typically consisting of 96 % iron (Fe) and 4 % silicon (Si) [Jil98]. Soft iron is a *ferromagnetic material*, meaning that it has a high *relative permeability*. Generally, the *permeability* μ is a measure describing the ability of a certain material to support the formation of a magnetic field within it. With regard to the permeability of vacuum, $\mu_0 = 1.257 \times 10^{-6}\,\mathrm{V\,s\,A^{-1}\,m^{-1}}$ [Kuc14], this yields the relative permeability $\mu_\mathrm{r} = \mu/\mu_0$. Soft iron with a four percent share of silicon has a relative permeability of up to 7000. For reference, mild steel has a relative permeability of 800 to 2000 [Kuc14]. In the shielded container this results in the magnetic field lines flowing mainly through the soft iron and not further entering the interior. Mu-metals, which might be used to individually shield the PMTs in the JUNO detector, are soft magnetic alloys typically consisting of 77 % nickel, 16 % iron, 5 % copper and

2 % chromium [Jil98]. As is the case for soft iron, mu metals are ferromagnetic materials and have a high relative permeability of up to 80 000 to 100 000 [Kuc14]. Due to the fact that the performance of mu metals can significantly decrease when subjected to mechanical stress, a mu metal based shielding was not used for the JUNO test facility.

The magnetic field inside the container was measured before and after the shielding was applied. The results of these measurements are described in section 5.2. Beforehand, section 5.1 gives an overview of the readout and evaluation method.

5.1. Readout and evaluation method

To measure the magnetic field strength inside the container, a Stefan Mayer Instruments FLC3-70 magnetic field sensor was used. The FLC3-70 is a triaxial fluxgate magnetometer that can measure magnetic fields of up to ±200 μT if supplied with a voltage of 12 V [Ste]. It does output three analogue voltages which are proportional to the magnetic field components in x, y and z direction. In order to read the voltages V, an external analogue to digital converter (ADC) was used, which can be read out via USB (COM-interface). A calibration of the ADC performed by the Aachen University resulted in an output voltage of

$$V_{\text{out}} = 9.375\,29 \times 10^{-2}\,\text{mV} \cdot |\boldsymbol{c}_{\text{ADC}}|, \tag{5.1}$$

where $|\boldsymbol{c}_{\text{ADC}}|$ is the absolute value of the vector of ADC counts that consists of the counts in x, y and z-direction:

$$\boldsymbol{c}_{\text{ADC}} = \left(c_{\text{ADC,x}}, c_{\text{ADC,y}}, c_{\text{ADC,z}}\right)^{\top}. \tag{5.2}$$

Utilising the software HTerm (see appendix B.5), the COM-port can be monitored and the vectors $\boldsymbol{c}_{\text{ADC}}$ can be saved to a text file. The data is evaluated using a ROOT script and visualised via GnuPlot (see appendices B.3 and B.4). First, the absolute values $|\boldsymbol{c}_{\text{ADC}}|$ are determined and averaged. Using equation (5.1), the absolute values are converted into a voltage. With this output voltage the magnetic field strength can be resolved, as the data sheet [Ste] states that an output voltage of 1 V corresponds to a field strength of 35 μT.

5.2. Results

The first measurement was performed before the soft iron shielding was fitted to the container. Due to the container being made out of steel, this ensures that the container itself is not magnetised. In total, 27 points of measurement were captured. For each point, ten vectors $\boldsymbol{c}_{\mathrm{ADC}}$ were taken. The coordinates of these points have an estimated accuracy of 20 cm. Figure 5.1 shows the results of the first measurement. The magnetic field inside the container ranges from a minimum of 27.88(27) µT to a maximum of 54.68(38) µT. Averaging over all points of measurement yields

$$|\boldsymbol{B}_{\mathrm{unshielded}}| = 43.12(528)\ \mu\mathrm{T}. \tag{5.3}$$

According to the United States National Oceanic and Atmospheric Administrations (NOAA) National Centers for Environmental Information (NCEI) [Nat], the earth's magnetic field in Hamburg amounts to:

$$|\boldsymbol{B}_{\mathrm{HH}}| = 49.65(15)\ \mu\mathrm{T}. \tag{5.4}$$

A measurement that was performed outside the test stand agrees with this value:

$$|\boldsymbol{B}_{\mathrm{HH,\ measured}}| = 49.18(225)\ \mu\mathrm{T}. \tag{5.5}$$

As expected, the measured field strength inside the test stand from equation (5.3) does not deviate substantially from the earth's field. It corresponds to approximately

$$|\boldsymbol{B}_{\mathrm{unshielded}}| \approx 0.87 \cdot |\boldsymbol{B}_{\mathrm{HH}}|. \tag{5.6}$$

This result does indicate that the steel of the container is not magnetised and rather shields the magnetic field slightly.

Another measurement of the magnetic field was performed within the shielded container. As a significant reduction of the field strength is expected, the measurement procedure was refined. This included a much larger number of measurement points and the implementation of a coordinate system allowing for a systematic measurement. The origin of the coordinate system was chosen to be in one of the container's inside bottom corners (see figures 5.1 and 5.3). The sensor was placed on a height-adjustable, non-magnetic table and its position was de-

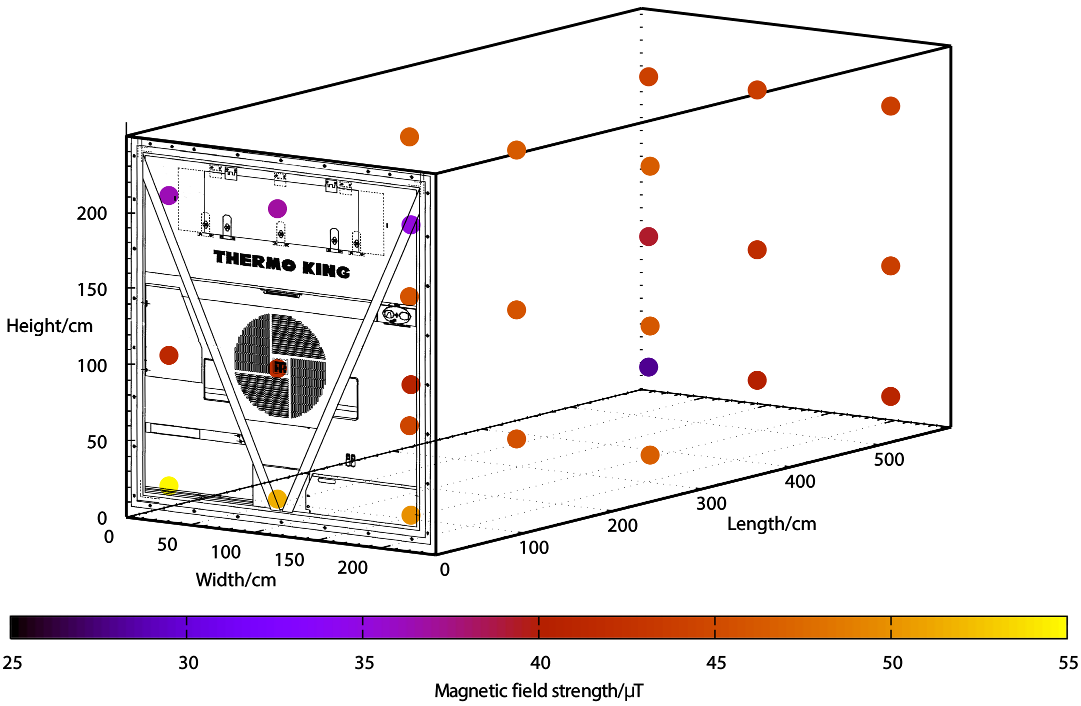

Figure 5.1.: The magnetic field strength inside the unshielded container. For each value, the error is less than 2 %. The coordinates of the 27 points of measurement have an accuracy of roughly 20 cm. At the front, the HVAC unit is sketched (source: [Ing08]). The door allowing to access the test stand is located on the opposite side.

termined using an ultrasonic rangefinder (type TOPCRAFT GT-UDM-07 [Top09]). The accuracy of this device is unknown, however it was cross-checked with a measuring tape. For the measurements of the coordinates, possible sources for statistic errors include an improper alignment of the rangefinder, i.e. the measuring axis not being parallel to the corresponding axis of the coordinate system. Also, slight bulges in the container's interior can lead to falsified values. It is estimated that the accuracy of each position is ±2.5 cm in each direction. For each position, 20 ADC values were taken and evaluated as described in the previous section.

The result of the measurement is shown in figure 5.3. It shows that the magnetic field is significantly reduced. Practically in the whole container the field strength ranges from 1.09(1) µT to a maximum of 6.66(4) µT, with an average of

$$|\boldsymbol{B}_{\text{shielded}}| = 2.7(10)\ \mu\text{T}. \tag{5.7}$$

Excluded from this mean are field strengths greater than 9 µT. Such values are exclusively located directly behind the HVAC unit inside the container. Here, two air vents (see figure 5.2) for the unit are placed, which could not be covered with shielding material for technical reasons. The magnetic field at these air slits ranges from 9.17(7) µT to 12.42(10) µT, correspond-

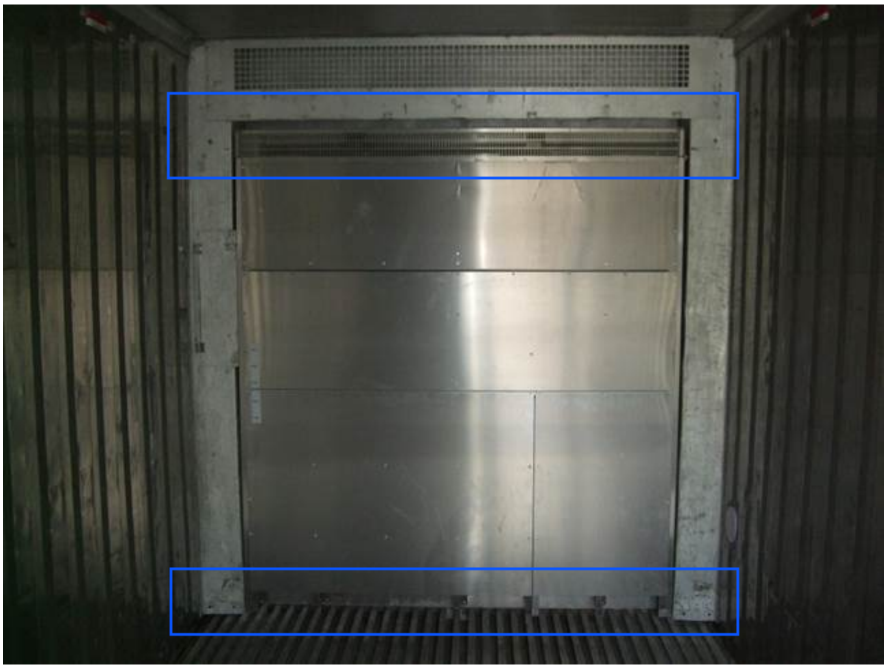

Figure 5.2.: An inside view of the container looking towards the back side of the HVAC unit. The photograph was taken *before* the magnetic shielding was applied. Ventilation slits of the HVAC unit are marked in blue. Due to technical reasons, these slits could later not be covered with shielding material.

ing to a reduction of the earth's magnetic field to approximately a fifth, not fulfilling the targeted specification of a reduction down to $0.1|\boldsymbol{B}_{\mathrm{HH}}|$. However, this behaviour was expected and the current planning sets forth that no photomultipliers will be placed in very close proximity to the vents. The predominant average field strength from equation (5.7) corresponds to a reduction of the magnetic field to

$$|\boldsymbol{B}_{\mathrm{shielded}}| \approx 0.06|\boldsymbol{B}_{\mathrm{HH}}|, \tag{5.8}$$

which fulfils the target of reducing the magnetic field inside the test stand to less than 10 % of the terrestrial magnetic field.

For all performed measurements inside the testing facility, the readout electronics for the sensor, i.e. the ADC as well as the computer, were also inside the test stand. While these devices do also produce a magnetic field that might adulterate the measurements, their influence on the readings was checked and found to be insignificant, unless the sensor is placed in direct proximity. Another fact that could affect the measurements is the presence of other unnaturally created magnetic fields (e.g. by the nearby PETRA experiment [Fra+06], which is a particle accelerator approximately 100 m away from the shipping container). Their influence was not specifically examined.

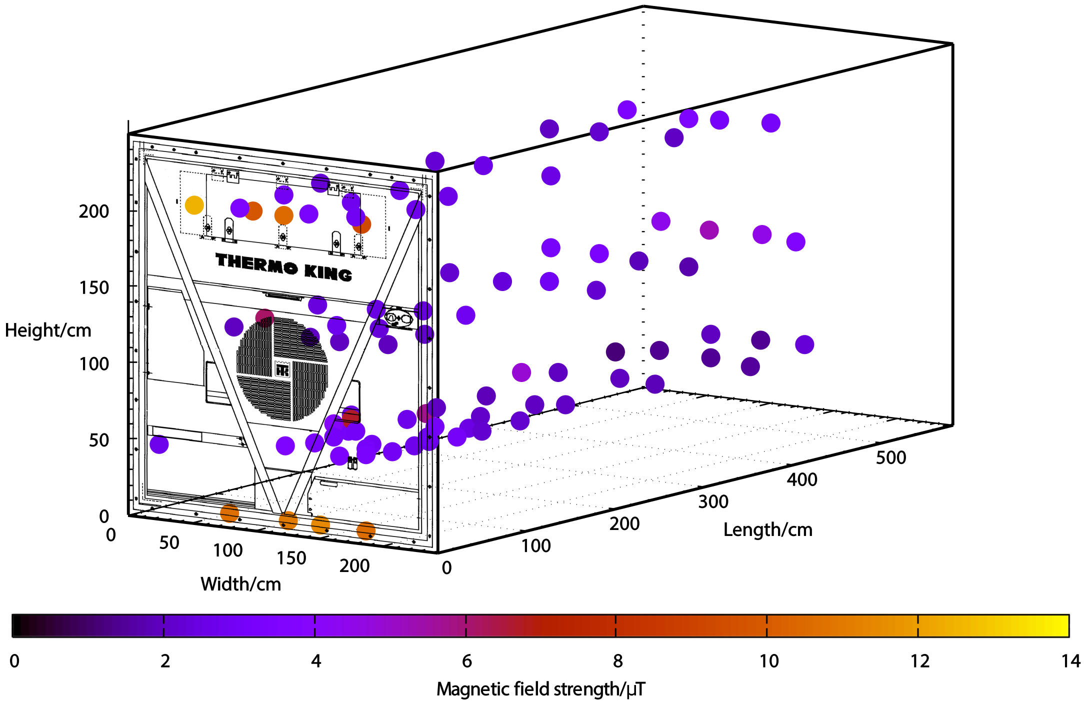

Figure 5.3.: The magnetic field strength inside the shielded container. For each value, the error is less than 1 %. The coordinates of the points of measurement have an assumed accuracy of ±2.5 cm. At the front, the HVAC unit is sketched (source: [Ing08]). The door allowing to access the test stand is located on the opposite side.

6 Implementation of a temperature monitoring system

The photomultiplier tubes for the JUNO experiment will be tested in a shipping container. For such a container, a temperature monitoring system was implemented. This chapter gives a detailed description of the developed system. In section 6.1, the necessity of the monitoring system is explained and an overview of the container given. Sections 6.2 and 6.3 outline the attempts and considerations of implementing the system using programmable logic controllers (PLCs). The final system based on an Arduino microcontroller is explained in detail in section 6.4. Section 6.5 illustrates the LabView integration of the monitoring system. Due to the fact that the container will be intensely used in future, the latter two sections should also be particularly understood as a documentation of the developed systems.

6.1. Motivation and overview

Four shipping containers will serve as test facilities for the JUNO photomultipliers. Here, the PMTs will each be placed in an aluminium drawer that is enclosed in an aluminium case (see figure 2.3). The aluminium drawer also holds a LED allowing to test the PMTs. Each test stand will contain 36 of these cases, i.e. 36 PMTs can be stored and tested simultaneously. The readout of the PMTs will be done utilising LabView, which is a monitoring and control software frequently used in particle physics (for a more detailed explanation of LabView see appendix B.1).

As discussed in section 3.3, the characteristics (e.g. the photo detection efficiency ψ, gain $\mathcal{G}$) of PMTs depend on the temperature. The specific temperature dependency of these characteristics for the JUNO photomultipliers has not yet been examined in detail. Additionally, the performance of the magnetic shielding that was discussed in chapter 5 might be affected by the temperature due to eventual changes of the permeability. Furthermore, the characteristics of the LED change with temperature. As for the temperature and magnetic field dependence of PMTs, the temperature dependence of LEDs is reliant on their type, material and manufacturing technique. In 1991, Reynolds *et. al.* [Rey+91] found the peak wavelength of a 660 nm LED to increase about 5.5 nm when subjected to a temperature change from 0 °C to 50 °C. Titkov *et. al.* [Tit+14] reported a change in the radiative efficiency of about 10 % over a temperature range of approximately 250 °C for a blue InGaN/GaN LED. The JUNO test stand will be equipped with an LED in the blue spectrum.

Because the tests that will be performed with the PMTs have to be comparable, it is of utmost importance to ensure that the PMTs are held at a constant temperature level. The temperature dependency of PMT also means that calibration data which will be acquired for the PMTs during testing will only be valid for a certain, known temperature. To ensure a constant temperature in the test stand, the shipping container is equipped with a Heating, Ventilation and Air Conditioning (HVAC) unit, based on a Thermo King Magnum+ cooling aggregate [Ing08] combined with an additional electric heater. Both units combined allow to control the inside air temperature of the container from −40 °C to 50 °C via a Siemens LOGO! controller [Con16] (see appendix B.2). For a smaller number of PMTs, the HVAC unit is later planned to be used to increase and decrease the temperature periodically from 5 °C to 45 °C. These temperature fluctuations impose mechanical stress on the photomultipliers due to the induced thermal expansion, causing an artificial ageing process of the PMTs. This is to evaluate in advance the change of the PMT's performances over time, as the JUNO experiment will be operating for several years.

The inside air temperature of the test stand is measured by the HVAC unit utilising a single PT100 sensor, which is a resistance temperature detector (RTD) that uses the dependency of platinum on the temperature (for a more detailed explanation of PT100 sensors, see section 6.2.1). However, this sensor alone is not sufficient for its intended use as it is only able to measure the temperature at a single point. Due to the placement of the HVAC unit or heat convection inside the test stand, it cannot be ensured that its interior will have a uniform temperature distribution.

Thus, another monitoring system has to be implemented. This monitoring system shall feature at least one sensor per drawer or PMT respectively, plus a few auxiliary sensors distributed in other parts of the test stand. Due to the PMTs being read out via LabView, it is appropriate to implement a monitoring system that also allows to be integrated into LabView.

Temperature sensors are available in many different form factors and types. When choosing a temperature sensor, the following key points have to be considered:

1. The temperature range $T_{\text{min}} < T_{\text{sensor}} < T_{\text{max}}$ the sensor needs to cover.
2. The highest allowed deviation δT from the true temperature, i.e. the accuracy.
3. The cost of the sensor as well as the cost and the complexity of the required readout electronics.
4. Special conditions under which the sensor has to operate (e.g. waterproofness).

In this application, a temperature range of $-40\,°\mathrm{C} < T < 50\,°\mathrm{C}$ is desired, as this is the maximum temperature range that can be achieved using the available HVAC-unit. The accuracy of the sensors should be 0.5 °C or better. Otherwise, no special requirements need to be met, although the functional ability at high air humidity levels is desirable, as such climate conditions may occur at the experimental site.

Based on these criteria and observations, various different sensor types were chosen. In the following sections these sensor types as well as the corresponding readout electronics and methods including their advantages and disadvantages will be discussed.

6.2. Beckhoff-fieldbus

The first system that was tested was based on a Beckhoff programmable logic controller (PLC), which will be described in section 6.2.2. Beforehand, a short overview of PT100 and PT1000 sensors, which were used in combination with the Beckhoff system, will be given in section 6.2.1.

6.2.1. PT100 and PT1000 sensors

The PT100 and PT1000 sensors are one of the most common temperature sensors and are widely used in industrial applications. They are *resistance temperature detectors* (RTDs) and use the temperature dependency of the electrical resistance in Platinum (Pt). Generally, in metals the electrical resistance is determined by the scattering of electrons in the conduction band on phonons, lattice defects and electron-electron-scattering. For low temperatures the phonons freeze out and the available phase-space volume for electron-electron scattering reduces [GM12]. Thus, for low temperatures a decrease in electrical resistance is expected. In metals, the temperature dependency of the resistance ρ can be mathematically described by the Bloch-Grüneisen law [Grü33; BBR06]:

$$\rho(T) = \rho_0 + A\left(\frac{T}{\Theta_\mathrm{D}}\right)^n \int_0^{\Theta_\mathrm{D}/T} \frac{x^n}{(\exp(x)-1)(1-\exp(-x))}\mathrm{d}x \tag{6.1}$$

$$= \rho_0 + \frac{A}{2}\left(\frac{T}{\Theta_\mathrm{D}}\right)^n \int_0^{\Theta_\mathrm{D}/T} \frac{x^n}{\cosh(x)-1}\mathrm{d}x. \tag{6.2}$$

Here, ρ_0 is the residual resistivity due to defect scattering, T the temperature, A a material constant and Θ_D the Debye-Temperature. The integer $n = 2, 3, 5$ depends upon the dominant interaction of free electrons [Oht+16; Cvi11]. Resistance due to electron-electron scattering is implied by $n = 2$. For $n = 5$, resistance due to electron-phonon scattering is implied, $n = 3$ describes resistance caused by s-d-electron scattering. Should more than one interaction be present, the total resistance can be determined by calculating the sum of the corresponding terms (Matthiessen's law) [Zin+73; PK82]. The case $n = 5$ particularly applies to transition metals such as platinum and thus, platinum RTDs; at least theoretically.

In practice, Pt-RTDs do not consist of pure platinum but rather of an alloy comprising of pure platinum alloyed with other platinum group metals [The06]. They are normed (DIN EN 60751 [Deu05]) within a temperature range of $T \in [-200\,°\mathrm{C}, 600\,°\mathrm{C}]$. At a temperature of 0 °C, PT100 (PT1000) temperature sensors have an electrical resistance of 100 Ω (1000 Ω). Hence, the resistance at a given temperature can be determined using a lookup table (see appendix A). Figure 6.1 shows the temperature dependency of PT100 and PT1000 sensors on the electrical resistance.

Mathematically, these dependencies differ slightly from equation (6.2) but can be described by the Callendar-Van-Dusen equation [Deu05]:

$$\rho_\mathrm{PT}(T) = \rho_0 \cdot \begin{cases} 1 + AT + BT^2 + CT^3(T - 100\,°\mathrm{C}) & \text{for } T \in [-200\,°\mathrm{C}, 0\,°\mathrm{C}) \\ 1 + AT + BT^2 & \text{for } T \in [0\,°\mathrm{C}, 600\,°\mathrm{C}]. \end{cases} \tag{6.3}$$

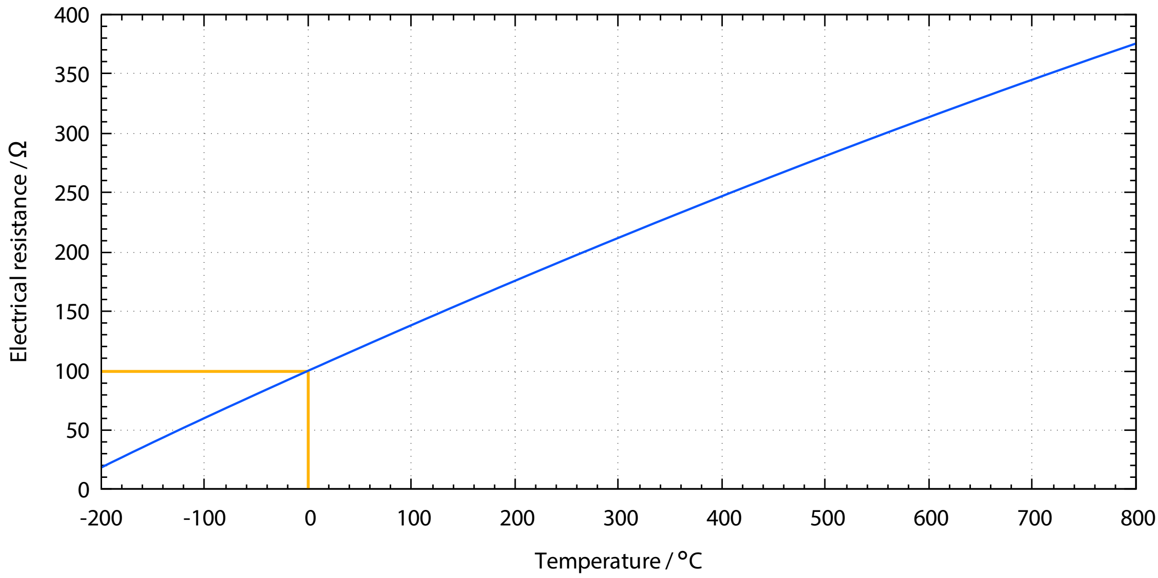

(a) PT100

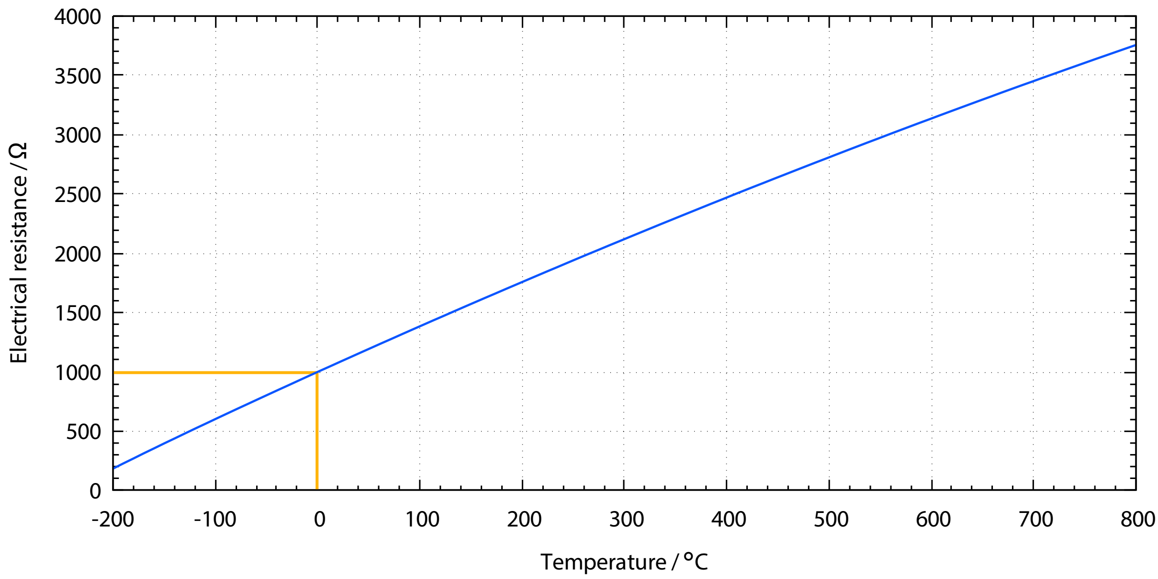

(b) PT1000

Figure 6.1.: The electrical resistance ρ of PT100 & PT1000 sensors as a function of the temperature according to [Deu05].

Here, the following constants apply:

$$A = 3.9083 \times 10^{-3}\,°\mathrm{C}^{-1}, \tag{6.4}$$

$$B = -5.7750 \times 10^{-7}\,°\mathrm{C}^{-2}, \tag{6.5}$$

$$C = -4.1830 \times 10^{-12}\,°\mathrm{C}^{-4}. \tag{6.6}$$

The PT100/PT1000 sensors can be wired up using different connection types. The easiest and cheapest connection can be established using a 2-wire connection as shown in figure 6.2a. Here, the resistances of the cables directly influence the measurements, as

$$\rho_{\mathrm{PT,measured}} = \rho_{\mathrm{PT}}(T) + \rho_1 + \rho_4, \tag{6.7}$$

where ρ_2 and ρ_3 are the resistances of the two cables attached to the sensor. From the Callendar-Van-Dusen equation (6.3) follows, that an additional resistance of 0.1 Ω does distort the measured temperature by roughly 0.3 K. Thus, systems using PT100 or PT1000 sensors in a 2-wire connection are only suitable for very short cable lengths unless the resistances of the cables are considered via an offset. Fluctuations in the resistance of the wires caused by temperature changes cannot be compensated.

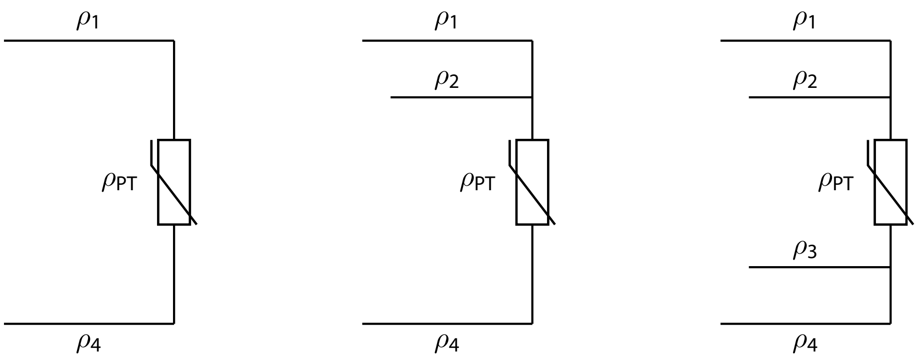

(a) 2-wire **(b)** 3-wire **(c)** 4-wire

Figure 6.2.: Different connection methods for PT100/PT1000 sensors. In a 2-wire connection, the resistance of the cables influence the measured temperature. In a 3-wire connection, the measured temperature is independent of the cables, should all leads have the same length. A complete independence of the cables can be achieved using a 4-wire connection.

In a 3-wire connection (see figure 6.2b), the measurements are not influenced by the cables resistances. In this case, a sense cable with a resistance ρ_2 is implemented next to the current-carrying wires. This sense cable allows to measure the voltage drop across one of the two wires. However, only the error of one of the cables is considered, as it is assumed that the same error occurs in the second wire. The error is weighed by a factor two. For a 3-wire connection the following relation applies:

$$\rho_{\text{PT,measured}} = \rho_{\text{PT}}(T) + \rho_4 - \rho_1. \tag{6.8}$$

Hence, if and only if both wires have the same resistances (e.g the same length and temperature), the error is mitigated.

Influences of the connecting cables can be completely diminished by using platinum RTDs in a 4-wire connection which is shown in figure 6.2c. As for the 2-wire and 3-wire connections, the sensor is supplied with current via two cables. The measuring voltage directly at the sensor can be tapped using two additional sensecables with resistances ρ_2 and ρ_3. The measured resistance is then exactly the resistance of the PT100/PT1000 sensor:

$$\rho_{\text{PT,measured}} = \rho_{\text{PT}}(T). \tag{6.9}$$

PT-RTDs connected via a 4-wire connection are often used in laboratory and calibration technology [WIK16].

6.2.2. Beckhoff

The Beckhoff Automation & Co. KG is a manufacturer of automation technology. Beckhoff offers a vast range of Bus Terminals including various input/output (I/O) components. Specifically, the KL3202 (KL3204) terminals can be used to read the temperatures from two (four) PT100/PT1000 sensors. The KL3202 terminal was the module that was tested. It allows the sensors to be connected using either a 2-wire or a 3-wire connection. An integrated microprocessor automatically performs a linearisation over the complete temperature range. The terminal is equipped with two ERROR LEDs, indicating a sensor error or a cable break. Two RUN LEDs indicate the active communication of the KL3202 module with the bus coupler. In this case, the Beckhoff BC-9000 bus terminal controller was used. The BC-9000 requires a 24 V power supply and connects to an external computer via an Ethernet port. This Ethernet port is also used to upload the desired configuration to the controller. The configuration itself is programmed utilising Beckhoffs TwinCat3 software and the programming language Structured Text (ST). The BC-9000 has integrated PLC (programmable logic controller) functionality and can be connected to 64 terminals in total [Bec16]. Figure 6.3 shows the complete and used stack of terminals that allows the implementation of the monitoring system, including the KL9001 bus end terminal. This module is required to establish the communication between the I/O terminals and the bus coupler.

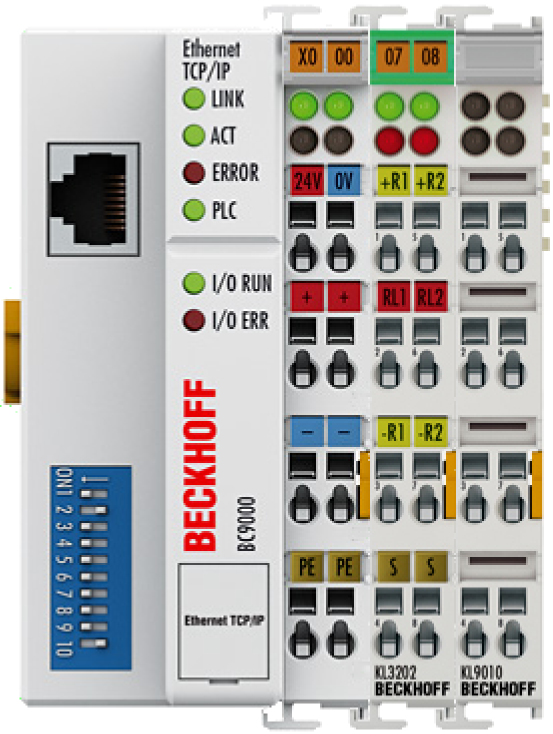

Figure 6.3.: The stack of Beckhoff modules consisting of a BC9000 Bus coupler (left), a KL3202 RTD module (middle) and a KL9010 bus end terminal (right). This setup can read two PT100/PT1000 sensors in either a 2-wire or a 3-wire connection. Power is applied to the bus coupler via an external 24 V power supply (not depicted). The bus coupler can be connected to a PC via an Ethernet port. Source: Own compilation based on illustrations from Beckhoff [Bec16].

The main advantage of using the Beckhoff system to read the PT100/PT1000 sensors is that its modularity allows it to be easily expanded on-the-fly. It also presents an all-in-one solution as other than the Beckhoff terminals themselves, the power supply and the sensors, no additional hardware is required.

For the application as a temperature monitoring system for the JUNO test stands it also desirable to integrate the monitoring system into the graphical programming system National Instruments™ LabView. The HVAC-unit of the container is controlled by a Siemens LOGO! controller, which can also be addressed and remote-controlled using LabView (see chapter 7). Beckhoff provides an automation device specification (ADS) library that supposedly allows for an easy LabView integration of the system.

The idea of using a Beckhoff system was discarded, as the solution turned out to be too costly compared to others, which will be discussed in section 6.4. Also, a reliable connection to the BC9000 bus controller via Ethernet could not be established. Besides, a solution based on a PLC would be quite excessive for a pure monitoring system, as PLCs are mainly used in industrial automation technology [WZ08].

6.3. Siemens LOGO!

Another solution that was considered but not tested was using a Siemens LOGO! controller like on the HVAC-unit of the container. Like Beckhoff, Siemens offers a programmable logic controller that can connect to various I/O terminals. Specifically, the LOGO! AM2 RTD expansion modules allow two PT100/PT1000 sensors to be connected in either a 2-wire or 3-wire connection. Theoretically, an advantage of using this solution is that the monitoring system can be combined with the Siemens powered HVAC-unit controller. However, this consideration was discarded and not practically tested due to cost reasons. Also, a single LOGO! controller allows for only eight analogue inputs (i.e. the readout of eight sensors), unless multiple controllers that are connected via a network are used.

6.4. Arduino microcontrollers

Another possibility to realise the required monitoring system lies within the usage of *microcontrollers*. A microcontroller is a system that is at least equipped with a microprocessor, memory and input/output ports [Ibr02], allowing it to control external devices. In order to evaluate their practicality, various Arduino microcontroller boards were acquired. These Arduino boards have been thoroughly tested with different sensor types. In the following sections, an overview over the Arduino platform is given and the different testing setups will be described.

6.4.1. Overview

Temperature monitoring systems using the Arduino platform have been successfully implemented in [ZFM14; Boc+14]. The Arduino platform consists of a hardware and a software part.

With regard to the software part, the Arduino platform comes with its own integrated development environment (IDE) that is based on `processing`. The programming language has close resemblances to `C/C++` based languages. An Arduino program is called *sketch*. First, variables are declared and initialised for later use. Code that is placed within the `void(setup)` function is executed once. The main function is the `void(loop)`. This function is continuously executed until the Arduino is disconnected from its power source. Within the scope of this thesis, all sketches were compiled using Arduino IDE version `V.1.6.9`.

A microcontroller board forms the hardware part of the platform. Due to the Arduino platform being open source, multiple other manufacturers other than Arduino manufacture and offer physically identical boards. A board is equipped with digital and analogue input/output ports. Via the input ports, data from sensors can be read. LEDs, relays or motors can be addressed using the output ports. Each board is equipped with a USB-port, allowing communication with a computer via the COM-interface. A brief overview of the range of Arduino boards is given in table 6.1.

Table 6.1.: Overview of some of the different available Arduino boards. Within the scope of this thesis, the Arduino UNO (basic) and the Arduino Mega (enhanced) were tested. Source: [Ard16].

Basic	Enhanced	Wearables	Internet capable
Arduino UNO	Arduino MEGA2560	Arduino GEMMA	Arduino YUN
Arduino PRO	Arduino ZERO	Arduino LILYPAD	
Arduino PRO Mini	Arduino DUE		
Arduino MICRO	Intel® Edison/Galileo		

Multiple different boards suiting various use cases are available. In [ZFM14], an Arduino UNO has been used to realise a temperature monitoring system for an incubator. Thus, concerning the implementation of the HVAC's monitoring system, the practicality of an Arduino UNO was chosen to be tested more thoroughly. Additionally, an Arduino MEGA2560 has been examined, as this board is flagged to offer enhanced functionality. The Arduino compatible Intel® Edison/Galileo 2 boards were not chosen, as they are able to run a Linux based operating system and are comparable to mini-computers like the Raspberry Pi series. The additional functionality of these boards was not deemed to be necessary. Also, the internet capable and wearable Arduino boards were not tested, as a direct internet connection is not required for this use case and the form factor is of no concern.

The Arduino UNO and MEGA boards are shown in figure 6.4. An overview of the technical data of both boards is outlined in table 6.2. The main difference of both boards is the amount of available memory and input/output ports. The Arduino MEGA has 256 kB of flash memory, which is eight times more than the UNO has. Concerning I/O, the MEGA has a total of 70 ports, 54 of which are digital. Of those, 15 offer pulse-width modulation (PWM) support. The UNO offers a total of 20 I/O ports with 14 being digital. Six digital ports feature PWM functionality. Each board is equipped with a different type of Atmel® controllers (UNO: ATmega328p, MEGA: ATmega2560) running at 16 MHz. Both microcontrollers have a built-in analogue to digital converter (ADC). In the following section, the processing power of the central processing units (CPUs) of both microcontrollers shall be discussed very briefly.

6.4.2. Computing power of the Arduino boards

The computing power of microprocessors is specified by the amount of *floating point operations per second* (FLOPS) or *integer operations per second* (IOPS). Both parameters have been very roughly determined in order to broadly evaluate and categorise the two CPUs.

In order to do so, a loop has been executed 255 times. In each loop iteration a basic mathematical operation (addition, subtraction, multiplication or division) using either floats or integers was performed. Then, the required time for 255 executions of the loop has been measured. Using this time, the amount of floating point operations and integer operations per second was calculated. Depending on the type of operation, different results were achieved. The results are shown in figure 6.5.

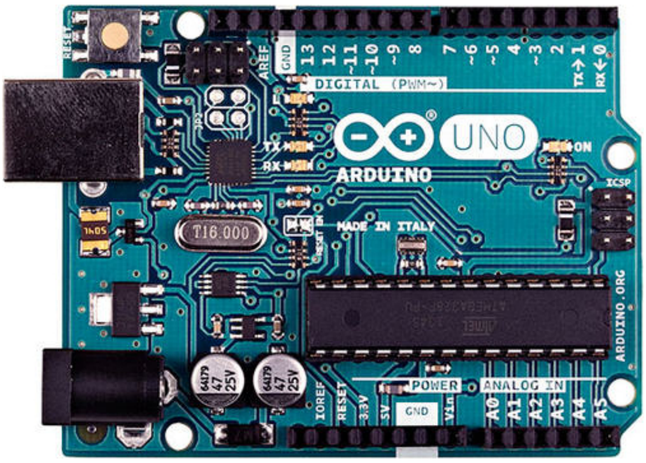

(a) Arduino UNO

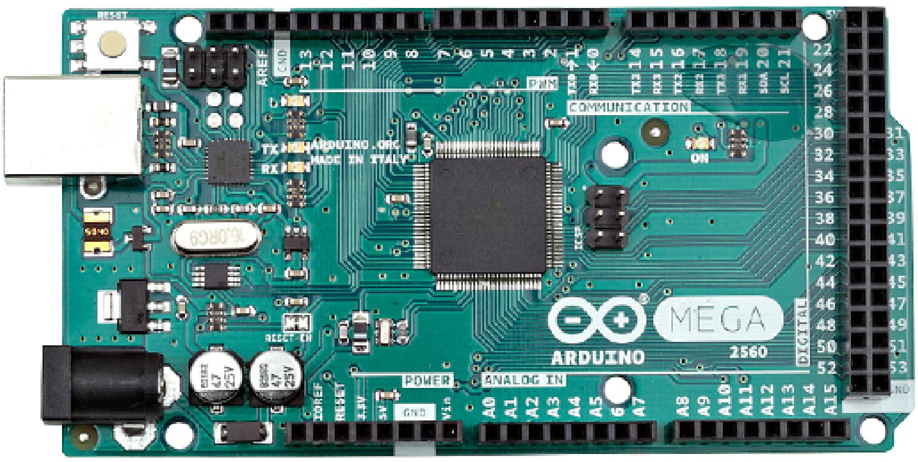

(b) Arduino MEGA2560

Figure 6.4.: Physical comparison between the two genuine Arduino boards that were tested. The Arduino UNO (top) offers basic functionality compared to the Arduino MEGA2560 (bottom), which offers enhanced functionality. Source: [ARD16].

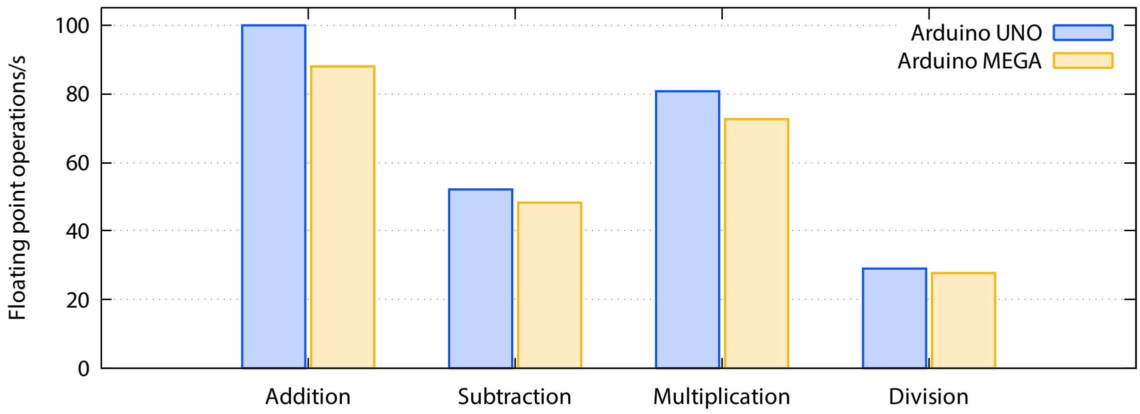

(a) FLOPS

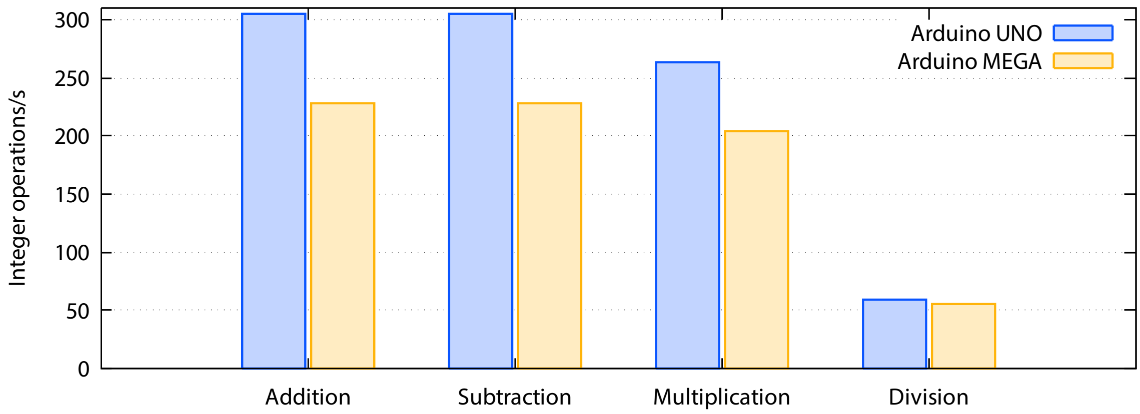

(b) IOPS

Figure 6.5.: Computing power of the two microprocessors installed on the Arduino UNO and the Arduino MEGA2560. The processing power is stated in floating point operations per second (FLOPS) and integer operations per second (IOPS) depending on different arithmetic operations. In all cases, the Arduino UNO has 10 % to 25 % more processing power.

Table 6.2.: Technical data of the Arduino UNO and Arduino MEGA2560 boards. Source: [ARD16]

			Arduino UNO	Arduino MEGA	Unit
Hardware		Microcontroller	ATmega328p	ATmega2560	
		CPU clock speed	16	16	MHz
		EEPROM	1	4	kB
		SRAM	2	8	kB
		Flash	32	256	kB
		UART	1	4	
Electrical		Operating Voltage	5	5	V
		Input Voltage	7-12	7-12	V
Connections	Analogue	Input	6	16	
		Output	0	0	
	Digital	Input & Output	14	54	
		PWM	6	15	
		USB	USB-B 2.0	USB-B 2.0	

Depending on the operation, the computing power of the Arduino UNO ranges from 29.01(1) kFlops to 99.86(10) kFlops and 59.51(4) kIops to 305.28(67) kIops respectively. Both boards yielded similar results, however the ATmega328p of the Arduino UNO turned out to be about 25 % more powerful in integer operations and roughly 10 % more powerful in floating point operations than the Arduino MEGA's ATmega2560 chip. For comparison, both Arduinos are about as powerful as a low-end Intel® Pentium 1 processor from 1993-1999, which does have 70 kFlops according to the manufacturers specifications [Int13]. During the evaluation of the different sensors (see sections 6.4.3, 6.4.4 and 6.4.5), no restrictions concerning the processing power of the boards did occur.

6.4.3. PT100/1000 analogue sensors

As described in section 6.2.1, PT-RTDs can be connected in three different ways. As a proof of concept, an electric circuit featuring a PT1000 sensor in a 2-wire connection, which was partially adapted from [Lea10; TS80], has been assembled (see figure 6.6) on a 6040 pin breadboard. The basic idea of this circuit is to convert the variable resistance of the sensor into a varying voltage, which can be analysed by the Arduinos internal ADC.

For this, a simple resistive voltage divider consisting of two resistors R_1 and $R_2 = \rho(T)$ (see equation (6.3)) has been implemented. When supplied with a voltage V_{cc}, this voltage divider does output a voltage given by

$$V_{out}(T) = \frac{\rho(T)}{R_1 + \rho(T)} \cdot V_{cc}. \tag{6.10}$$

Because the HVAC unit can cover a temperature range from −40 °C to 50 °C, this setup of the monitoring system has been configured to ensure full accuracy over a slightly larger range from −45 °C to 55 °C in order to take inaccuracies of the HVAC unit into account. With $V_{cc} = 5\,\mathrm{V}$, $R_1 = 10\,\mathrm{k\Omega}$, the output voltage is:

$$V_{out}(T) = \begin{cases} 0.380\,\mathrm{V} & \text{at } T = -45\,°\mathrm{C}, \\ 0.541\,\mathrm{V} & \text{at } T = 55\,°\mathrm{C}. \end{cases} \tag{6.11}$$

Given that the Arduino splits the default reference voltage of 5 V into 1023 divisions, the voltage range from equation (6.11) yields roughly 33 divisions. Thus, the accuracy over the range from −45 °C to 55 °C is equal to $100\,°\mathrm{C}/33 \simeq 3.03\,°\mathrm{C}$. To achieve a higher accuracy, the Arduinos reference voltage can be reduced via a command in the sketch to a minimum of 1.1 V. This would give an accuracy of 0.67 °C. Further improvements can be made, by modifying the voltage output from the measurement circuit so that at −45 °C the voltage is 0 V and at 55 °C the voltage is 1.1 V. This would result in an accuracy of approximately 0.10 °C.

In order to do so, a difference amplifier based on a Texas Instruments® LM358 operational amplifier (op-amp) and four resistors (R_5, R_6, R_7, R_8, see figure 6.6) has been implemented. If $R_5 = R_6$ and $R_7 = R_8$, its output voltage is given by [Lal08]

$$V_{out} = G \cdot \Delta V = \frac{R_7}{R_6}(V_{I^+} - V_{I^-}), \tag{6.12}$$

where $G = R_7/R_6$ is the gain and V_{I^-}, V_{I^+} are the voltages that are applied to the inverting input (I^-, pin 2) and the non-inverting input (I^+, pin 3). At −45 °C the voltage V_{I^+}, which is the voltage output of the PT1000 stage, will be 0.380 V (see equation (6.11)). Thus, in order to achieve an output voltage of 0 V at −45 °C at the difference amplifier, the voltage V_{I^-} has to be 0.380 V. This voltage is created using another voltage divider (R_3, R_4) that uses a variable 100 kΩ potentiometer. Its required resistance value of 8.23 kΩ can be derived from equation (6.11) (or be looked up in table A.1) and was set using a digital multimeter (Voltcraft, type VC-120).

In order to achieve an output voltage of 1.1 V at 55 °C, the voltage difference at 55 °C of 0.541 V − 0.380 V = 0.161 V has to be amplified to 1.1 V. This does require a gain of approximately $G \approx 6.8 = R_7/R_6 = 68\,\mathrm{k\Omega}/10\,\mathrm{k\Omega}$.

It has to be noted that because the difference amplifier circuit does draw some current, more current will flow through the first resistor of the voltage divider than through the second resistor. Thus, the output voltage of the voltage divider will be adulterated. In order to eliminate this effect, a *voltage buffer* (also: *voltage follower*) has been implemented. It consists of another LM358 op-amp in a setup that represents an amplifier with a gain of $G = 1$. The op-amps output is directly fed back into the inverting output, forcing it to adjust its output voltage equal to the input voltage. This way, a steady input of the desired voltage at the difference amplifier is ensured. For the same reasons, the RTD part of the circuit is also connected to the difference amplifier by a voltage follower.

The developed circuit in combination with the Arduinos ADC reference voltage setting of 1.1 V theoretically gives 0 ADC-counts at −45 °C and 1023 ADC-counts at 55 °C. Within this temperature interval of 100 °C the dependency of the temperature T on the ADC-counts c_{ADC} can then be described by a linear function:

$$T(c_{\mathrm{ADC}}) = \frac{100\,^{\circ}\mathrm{C}}{1023} \cdot c_{\mathrm{ADC}} - 45\,^{\circ}\mathrm{C}. \tag{6.13}$$

At first, a simple Arduino sketch has been used to read only the value from the analogue input. The signal, represented in figure 6.7 in blue, did show a considerable degree of noise. Five hundred values have been recorded, resulting in a mean of

$$\overline{c}_{\mathrm{ADC},1} = 594.44(261)\ \mathrm{cts}.$$

The values have an average absolute deviation from the mean of 2.11 cts. In order to reduce the amount of noise, various changes to the setup from figure 6.6 were tested. The minimum amount of noise was observed, when the decoupling capacitor C_1 and the resistor R_9 which

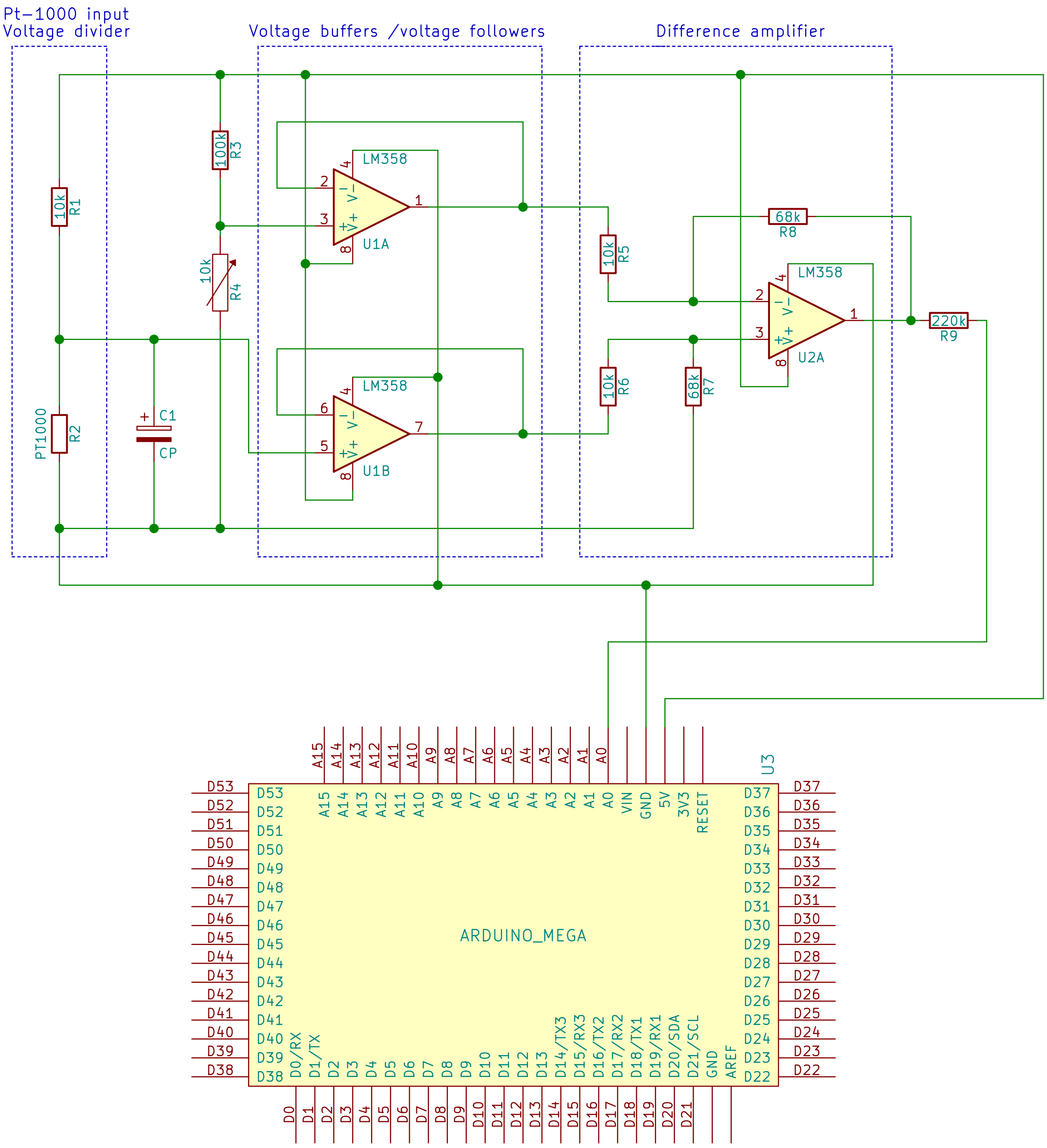

Figure 6.6.: The circuit that has been used to read a PT1000 sensor in a 2-wire connection using a genuine Arduino MEGA2560 board. Later, the decoupling capacitor C_1 and the resistor R_9 have been removed as a noise-reduction measure. The circuit's design was slightly adapted from [Lea10].

were proposed in [Lea10] were removed. The signal with a reduced noise level is represented in figure 6.7 in orange. A sample of 500 values yielded

$$\bar{c}_{\mathrm{ADC},2} = 595.89(84)\,\mathrm{cts},$$

with the values having an average absolute deviation of 0.64 cts from the mean. The aforementioned modifications to the circuit therefore resulted in a significant reduction of the noise by about a factor of four. A certain residual amount of noise may have been caused by inaccuracies or fluctuations of the Arduino's built in ADC.

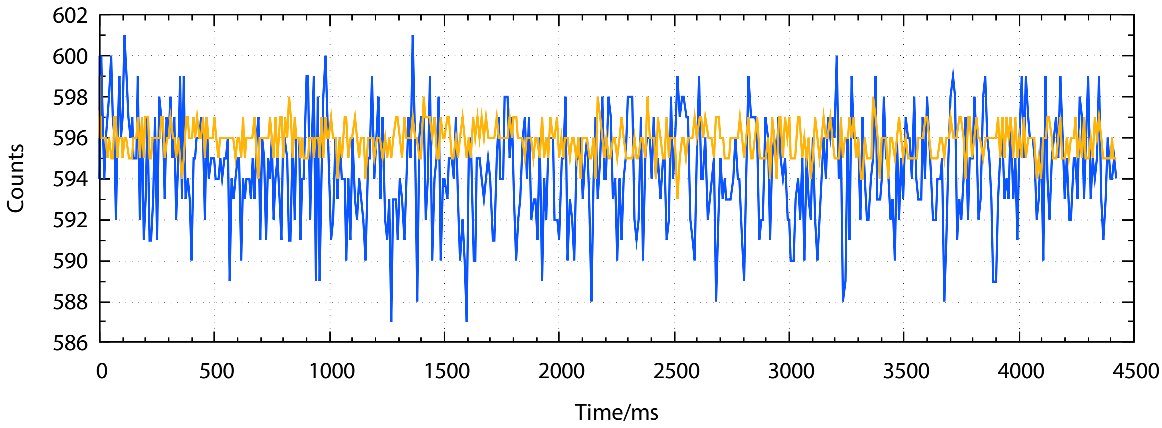

Figure 6.7.: The raw signal of the PT1000 circuit before calibration. In blue: The signal before any noise reduction modifications were performed. In this case, the circuit corresponds to the one shown in figure 6.6. In orange: The signal with reduced noise after C_1 and R_9 have been removed.

The signals have been converted into a temperature using equation (6.13) with a modified Arduino sketch. Although the signals were changing with temperature, they resulted in unrealistic temperature values. Despite the fact that the resistors used in the circuit have been chosen and set carefully, deviations from their nominal values result in a distorted signal. For reference, the aforementioned noise analysis was performed at room temperature, yet the results of about 595 cts would correspond to temperatures of roughly 13 °C. In order to obtain more accurate readings, the circuit was calibrated. For this purpose, the minimum resistance of the RTD, i.e. the resistance of the PT1000 (R_2) at the minimum temperature of −45 °C has been calculated to $R_{2,\mathrm{min}} = 822.90\,\Omega$ using equation (6.3). The sensor was then temporarily replaced by a resistor with a nominal value of 820 Ω (measured value: 823 Ω, for the measurement a Voltcraft digital multimeter Type VC 820 was used). Then, the potentiometer R_4

was adjusted, until the ADC-counts reached a minimum value. Theoretically, this minimum should be at 0 cts, however a value of 10(1) cts was observed. A measurement at room temperature using this calibrated circuit in combination with a PT1000 sensor showed 510 cts or 4.85 °C respectively. Another PT1000 sensor showed a slightly lower temperature of 3.97 °C. These unrealistic values probably originated from defective sensors. The used PT1000 sensors have already seen extensive use in the OPERA experiment [Gul+00]. Closer investigations showed, that the used sensors had resistance values of roughly 1009 Ω at 25 °C room temperature (confer table A.1).

In order to test the system with newly acquired PT100 thin-film sensors, the resistor R_1 in the RTD voltage divider was replaced with a 1 kΩ resistor. A recalibration was performed with a $R_{2,\mathrm{min}} = 80\,\Omega$ resistor (nominal, actual: $R_{2,\mathrm{min}} = 82.3\,\Omega$). The theoretically required value of $R_{2,\mathrm{min}} = 82.29\,\Omega$ can be derived from equation (6.3) or from the lookup table in appendix A. Measurements showed a temperature of

$$T_{\mathrm{PT100}} = 26.39(11)\,^{\circ}\mathrm{C}.$$

Another system that has been tested at the same time using multiple digital sensors (see section 6.4.5) showed a similar reading of $T_{\mathrm{DS18B20}} = 25.35\,^{\circ}\mathrm{C}$. A room thermometer indicated a temperature of 25.5 °C, generally agreeing with the reading of the digital sensors. The value measured by the PT100 circuit is about 1 °C higher, which is probably due to the calibration not having been precise enough.

6.4.4. LM35 series analogue sensors

The Texas Instruments Incorporated (short: TI) LM35 series are low-cost precision centigrade sensors. A temperature monitoring system based on an LM35 sensor and an Atmel ATmega8535 microcontroller has been successfully implemented in [WS12]. Particularly, their usage is often proposed in combination with Arduino microcontrollers (see [Bar12; Brü12]). In this section, the functional principle of the LM35 series sensors, their readout with an Arduino and the associated LabView integration are discussed.

6.4.4.1. Working principle

The LM35 are analogue *proportional to absolute temperature* (PTAT) sensors [SE15]. In general, the core element of a PTAT sensor is a pair of p-n-junctions (e.g. diodes or transistors). In an LM35 sensor, two transistors are used, both of which are operated at different emitter current densities J_{E_1}, J_{E_2}. Thus, both transistors have different base-emitter voltages V_{BE_1}, V_{BE_2}. It can be shown [SE15], that the difference ΔV_{BE} between the two base-emitter voltages is given by

$$\Delta V_{BE} := V_{BE_1} - V_{BE_2} = \frac{n k_B T}{e} \ln\left(\frac{J_{E_1}}{J_{E_2}}\right). \tag{6.14}$$

Here, n is a fabrication constant, T the temperature, $k_B = 1.38 \times 10^{-23}\,\mathrm{J\,K^{-1}}$ the Boltzmann constant and $e = 1.60 \times 10^{-19}\,\mathrm{C}$ the elementary charge [Kuc14]. If the ratio of current densities J_{E_1}/J_{E_2} is held constant, it follows from equation (6.14), that

$$\Delta V_{BE} \propto T. \tag{6.15}$$

While this is true over small temperature ranges, a certain non-linearity is still observed over the sensor's complete temperature range. In an LM35 sensor, the non-linearity is partially compensated using a compensation circuit. The full schematics of the LM35 sensors shall, however, not be further discussed within the scope of this thesis. A brief overview of the technical data of the LM35 type CZ sensor is shown in table 6.3, a complete overview can be found in [Tex16]. All LM35 sensors have a linear scaling factor of $10\,\mathrm{mV\,°C^{-1}}$. They do not require any external calibration and have an accuracy of $\pm 0.25\,°\mathrm{C}$ at room temperature. Required readout electronics are simple and only require a minimum amount of circuitry. They offer a low self-heating of about $\pm 0.08\,°\mathrm{C}$, as only a maximum of $60\,\mu\mathrm{A}$ of current is drawn.

6.4.4.2. Readout

The LM35 series sensors in combination with an Arduino board require only a minimum amount of circuitry. Early, successful tests were performed using an Arduino UNO compatible board (model: SainSmart UNO) in combination with type DZ sensors on an 830 pin breadboard. Figure 6.8 shows the fundamental design of the circuit, which has been taken from [Bar12]. The LM35 series sensors can be directly connected to the Arduinos 5 V and

Table 6.3.: Technical data of the National Instruments™ LM35 series type CZ sensors. Source: [Tex13].

				Unit
Specified operating temperature	$T_{\mathrm{min}} = -55 \leqslant T \leqslant 150 = T_{\mathrm{max}}$			°C
	Condition	*Typical*	*Maximum*	
Accuracy	$T = -10$	±0.3	±1.0	°C
	$T = 25$	±0.2	±0.5	°C
	$T = T_{\mathrm{min}}$	±0.4	±1.0	°C
	$T = T_{\mathrm{max}}$	±0.4	±1.5	°C
Non-linearity	Within $T_{\mathrm{min}} \leqslant T \leqslant T_{\mathrm{max}}$	±0.15	±0.3	°C
Long term stability/drift	$T = T_{\mathrm{max}}$ for $t = 1000$ h	±0.08		°C
		Minimum	*Maximum*	
Input voltage		−0.2	35	V
Output voltage		−1.0	6	V
Output current			−0.2	V

ground pins. The output voltages V_{out} of the sensors are hooked up to the analogue inputs of the UNO. Depending on the measured value c_{ADC} at the analogue input, the temperature of an LM35 series sensor can be calculated via

$$T(V_{\mathrm{ref}}, c_{\mathrm{ADC}}) = \frac{V_{\mathrm{ref}} \cdot 100 \cdot c_{\mathrm{ADC}}}{1024}. \tag{6.16}$$

Here, V_{ref} is the Arduinos ADC reference voltage. Similar to the PT100/PT1000 sensors, a reference voltage of $V_{\mathrm{ref}} = 5$ V will cause an inaccurate resolution. Thus, $V_{\mathrm{ref}} = 1.1$ V was used, which results in

$$T(c_{\mathrm{ADC}}) = \frac{125}{256}\, c_{\mathrm{ADC}}. \tag{6.17}$$

However, the LM35DZ sensors only have a temperature range from 0 °C to 100 °C. Also, the circuit that has been used thus far is only suitable for 2 °C to 150 °C [Tex16].

Thus, four LM35 type CZ sensors have been acquired. Their technical data corresponds with the specifications given in table 6.3. An improved circuit, which is shown in figure 6.9, was adapted from [Tex16] and allows the readout of temperatures lower than 0 °C. Due to the circuit's design, the readout of one sensor requires two analogue inputs and the UNO had to

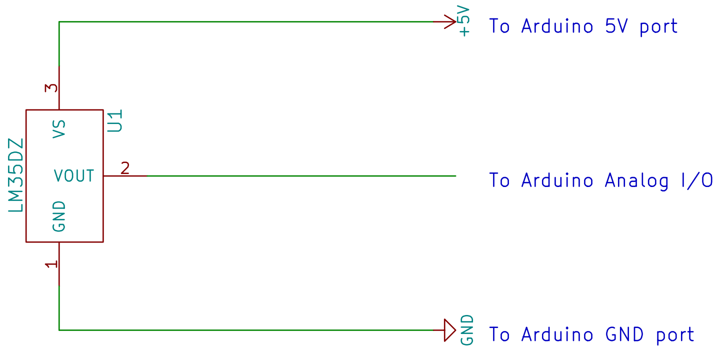

Figure 6.8.: The most basic circuit allowing to read a single LM35 series sensor. The sensor and the circuit were later changed to allow for negative temperatures to be measured.

be replaced with a genuine MEGA due to its enhanced I/O capabilities (see table 6.2). The sensors have been read out using a sketch that reads the values from the two analogue pins each sensor is connected to. Afterwards, the mean of 100 read values is computed. This hard coded averaging is not intended to increase the temperature accuracy, but mainly to reduce the fluctuations of the Arduinos ADC. The difference of the averaged readings corresponds to c_{ADC} from equation (6.16), which was then used to determine the temperature. It is important to note, that in this case the reference voltage V_{ref} has *not* been reduced to 1.1 V and was left at 5 V, as the greater temperature range requires a higher reference voltage.

A temperature measurement that was performed at ambient temperature with all four sensors is shown in figure 6.10a. During the measurement, a total of 200 temperature samples were acquired. In order to hold the temperature at a constant level, the complete system was placed in an airtight drawer and wrapped in multiple layers of aluminium foil separated by expanded polysterene foam. The system was before placed in an antistatic bag, thus, short circuiting of the system due to the aluminium foil could be prevented. Averaged over all values, the sensors showed the following temperatures:

$$\begin{aligned} T_1 &= 28.67(3)\,^{\circ}\mathrm{C}, \\ T_2 &= 29.72(3)\,^{\circ}\mathrm{C}, \\ T_3 &= 28.73(3)\,^{\circ}\mathrm{C}, \\ T_4 &= 28.11(3)\,^{\circ}\mathrm{C}. \end{aligned} \tag{6.18}$$

A reference bimetal thermometer (Feingerätebau Fischer, Thermometer Typ 117) indicated a temperature of roughly 28 °C, which is lower than any of the sensors readings. The readings of sensors S_2 and S_4 deviate by 1.61 °C, exceeding the expected deviation of 1 °C caused by the ±0.5 °C accuracy. Deviations higher than 1 °C between sensors have also been observed using the LM35 type DZ sensors with the basic circuit from figure 6.8. Measures to reduce the noise included adding bypass capacitors and R-C dampers to the circuitry from figure 6.9, as proposed in [Tex16]. No noticeable improvements could be observed. A short test was performed to confirm that the built circuit is able to operate under low temperature conditions. For this, the previously insulated system was placed in a refrigeration unit set to −15 °C. This measurement (see figure 6.10b) yielded in average

$$\begin{aligned} T_1 &= -14.53(5)\,^\circ\mathrm{C}, \\ T_2 &= -14.66(5)\,^\circ\mathrm{C}, \\ T_3 &= -13.99(7)\,^\circ\mathrm{C}, \\ T_4 &= -14.97(5)\,^\circ\mathrm{C}. \end{aligned} \tag{6.19}$$

Here, the reference thermometer indicated a temperature of roughly −14.5 °C, agreeing with the results from equations (6.19). Compared to the results from the measurement under ambient temperature conditions, a reduction of the level of variation between the sensors and an increase of noise can be observed.

A test with regard to different cable lengths was performed using five LM35CZ sensors that have been calibrated in order to achieve comparable results. For this, the over 200 samples averaged temperature of each sensor was progammatically set to 30 °C in the Arduino sketch using different offsets. One reference sensor with no cable was placed directly on the breadboard. The other four were attached to cables with lengths l of 5 m, 10 m, 15 m, and 20 m. The used cable was an unshielded 3M™ 2100 Series Twisted Pair Flat Cable with copper conductors, a capacitance of 47.9 pF m^{-1} [3M 10] and a measured resistance of 0.21 Ω m^{-1}. Measuring 200 samples for each sensor over a course of 17 min resulted in

$$\begin{aligned} T_1(l = 0\,\mathrm{m}) &= 30.16(4)\,^\circ\mathrm{C}, \\ T_2(l = 5\,\mathrm{m}) &= 31.10(13)\,^\circ\mathrm{C}, \\ T_3(l = 10\,\mathrm{m}) &= 32.39(65)\,^\circ\mathrm{C}, \\ T_4(l = 15\,\mathrm{m}) &= 34.56(71)\,^\circ\mathrm{C}, \\ T_5(l = 20\,\mathrm{m}) &= 37.03(181)\,^\circ\mathrm{C}. \end{aligned} \tag{6.20}$$

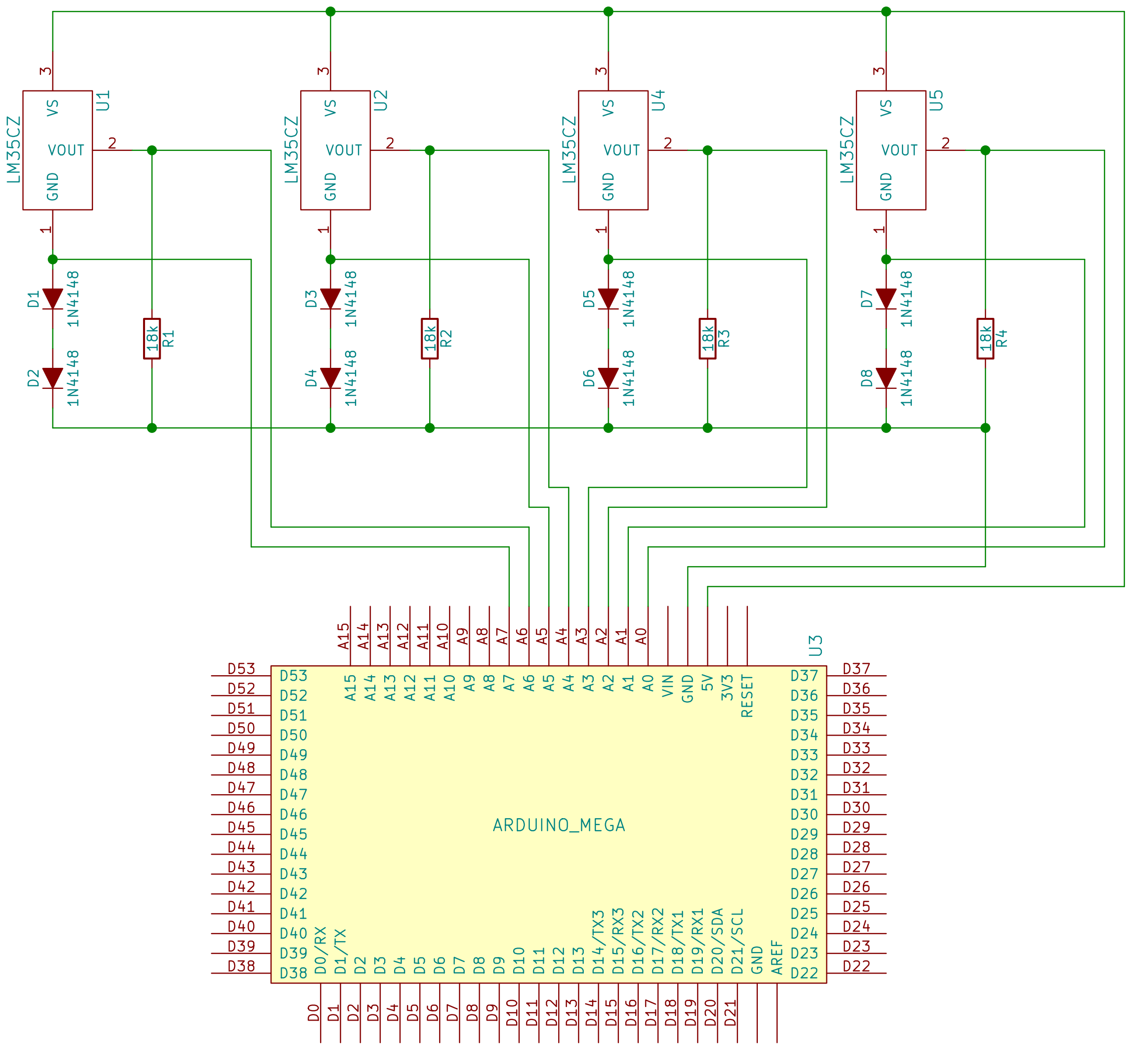

Figure 6.9.: The electric circuit used to read out four LM35CZ sensors in parallel at low temperatures in combination with a MEGA2560 board. The circuit was adapted from [Tex13].

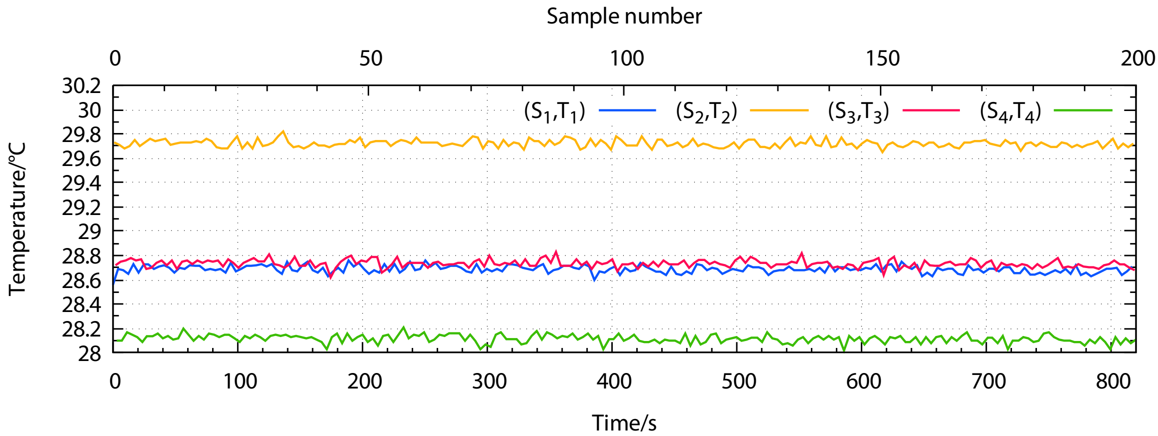

(a) Measurement at room temperature.

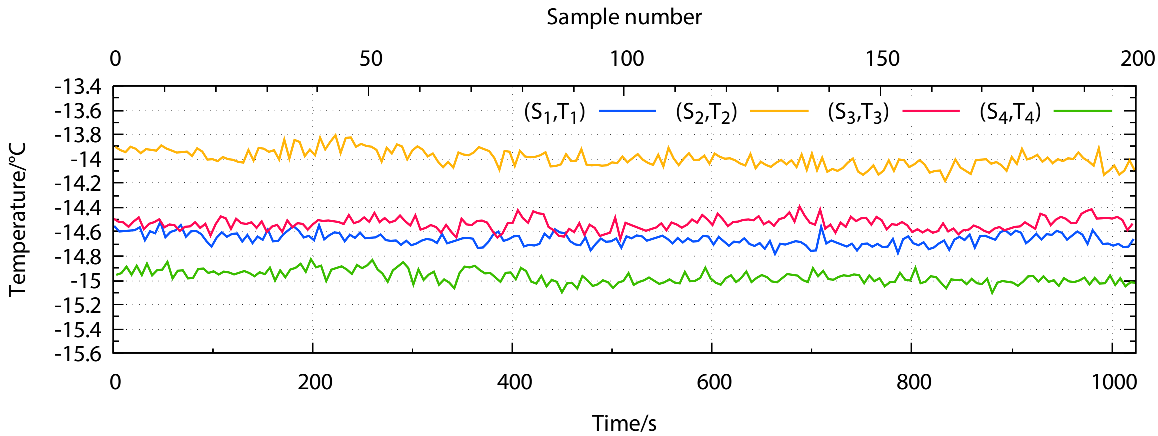

(b) Measurement under low temperature conditions.

Figure 6.10.: Two temperature measurements with LM35CZ sensors conducted under ambient and low temperature conditions. A total of 200 samples were taken for each measurement. For the measurement at low temperatures, the measurement duration was slightly larger due to another fifth sensor, which was not actually connected, but has been accounted for in the sketch. In both cases, the test system was enclosed in isolation material to diminish short term temperature fluctuations. Each colour corresponds to a different LM35CZ sensor S_i with its temperature T_i.

Figure 6.11 shows the results graphically. As expected, the standard deviation and the noise correspondingly with regard to the sensor without a cable increase with the cable length. The observed increase is non linear. Also, a non linear increase of the measured temperature with the cable length was observed.

As an attempt to reduce the noise, an $R = 2\,\mathrm{k}\Omega$ resistor was added to the V_{out} pin of the sensor as well a $C_{bp} = 10\,\mathrm{nF}$ bypass capacitor as proposed in the data sheet [Tex16] for powering high impedance devices. Also, the system was used with the sensors being supplied with power using an external supply (type Voltcraft PA1000S LED) and not the Arduinos 5 V and GND pins. However, these measures did not change the observed behaviour of increasing temperatures and noise levels with longer cables.

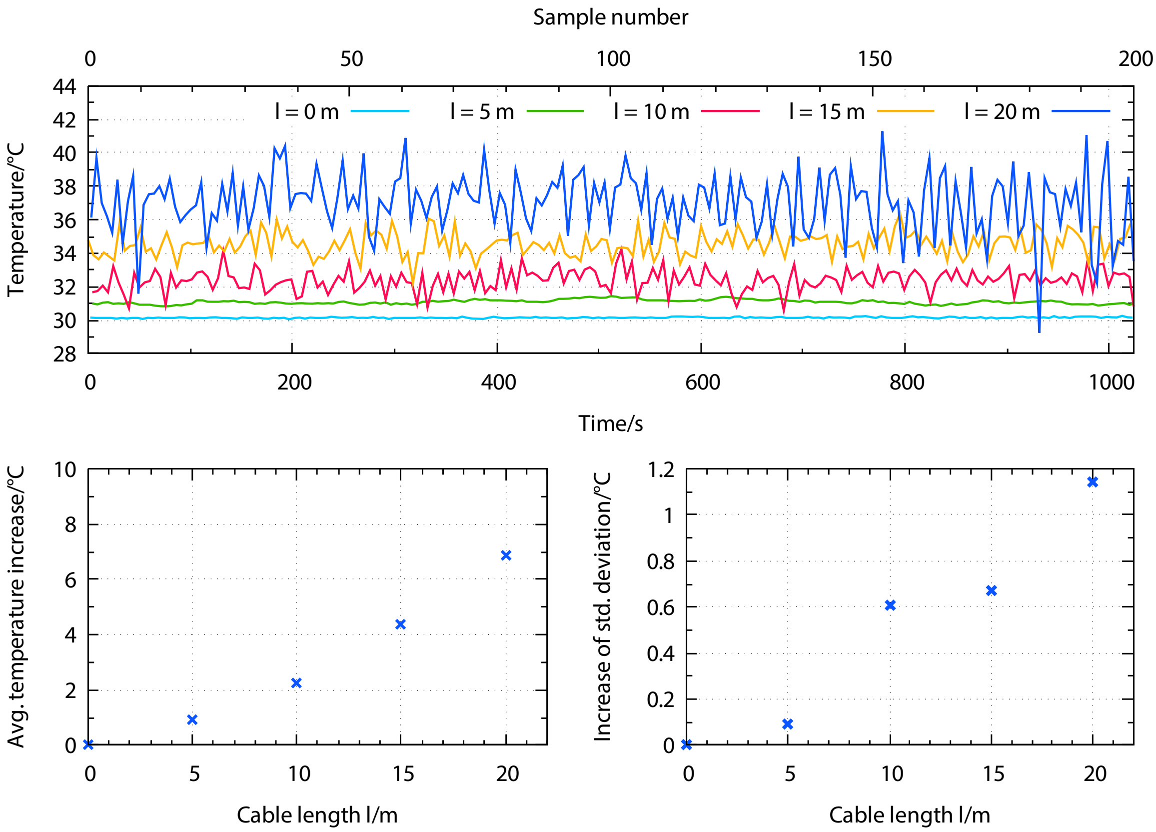

Figure 6.11.: The temperature values that were read out by five LM35CZ sensors with different cable lengths ranging from 0 m to 20 m under ambient temperature conditions (top). In total, 200 temperature samples were acquired. During testing, the system was wrapped in isolation material to diminish short term temperature fluctuations. On the bottom, the average temperature increases as well as the increase of their standard deviations depending on the cable length are depicted.

6.4.4.3. LabView integration

As a proof of concept, a single sensor has been read out via National Instruments LabView (for a detailed description of LabView see appendix B.1). For this, a genuine Arduino Mega2560 has been flashed with the Digilent LINX firmware, which is available from [Nat16], or directly from the LabView VI Package Manager. It is a firmware that allows LabView to issue commands to the Arduino via the COM-port (see figure 6.12). After the Arduino processes the command, the data is sent back to LabView, again via the COM-port. This means, that a two-way connection can be established, where LabView *directly* controls the Arduino. However, a reliable connection to the Arduino board could not be established. Thus, the discontinued predecessor of LINX, the LabView Interface for Arduino (LIFA) has been used. Although the LIFA framework lacks several features compared to the LINX framework, it works in the same way. The `LIFA_Base` firmware was compiled and uploaded to the MEGA using an early version of the Arduino IDE (`v.1.0.5-r2`).

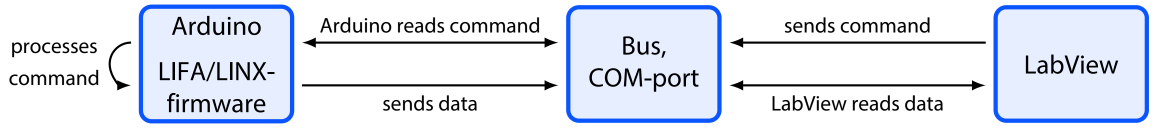

Figure 6.12.: This block diagram illustrates the two-way communication between LabView and the Arduino in the case of LM35CZ sensors. The Arduino runs the LabView Interface for Arduino (LIFA) firmware, which allows LabView to directly access and control the Arduino via the COM-port. Data from the Arduino is then transmitted back to LabView again via the COM-port.

The readout program for the single LM35CZ sensor is shown in figure 6.13. The program first initialises the Arduino using a VI provided by the LIFA package. For this, the appropriate COM-Port has to be set by the user. A `while` loop contains the main readout code. For better clarity, a custom function (`LM35CZ - Read Temp`) has been written. This SubVI reads the voltages from the two user specified analogue input pins and uses their difference to calculate the temperature. In order to average over n readings (n is a user set variable), an array of the dimension $D = n$ containing zeros is initialised. These zero valued array elements are then gradually replaced by the temperatures from the custom SubVI using a `for` loop with n iterations. A standard LabView VI is then used to compute the mean of the temperatures in the array as well as their standard deviation and variance. If the loop is stopped by the user, the connection to the Arduino is closed. The successful LabView integration for this one LM35CZ sensor can be expanded relatively easy to read out more than one sensor.

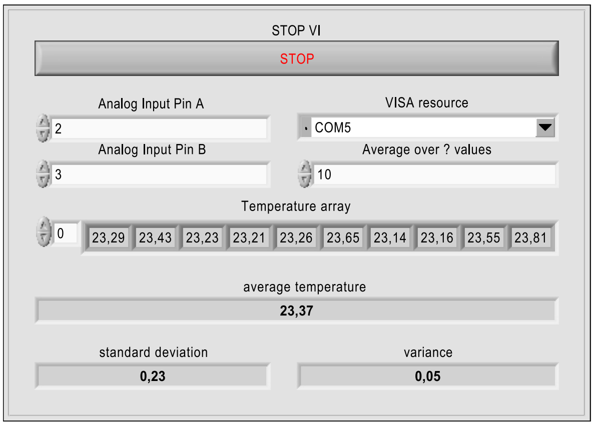

(a) Front panel: On the top, the VI can be stopped using the "STOP" button. Next, the user can set the Arduino pins to which the sensor is connected to as well as the COM port and the number of temperatures over which averaging will be performed. In the "Temperature array", the temperature readings over which is averaged are shown. In the bottom, the average temperature as well as the standard deviation and the variance are shown. All temperatures are displayed in degrees Celsius.

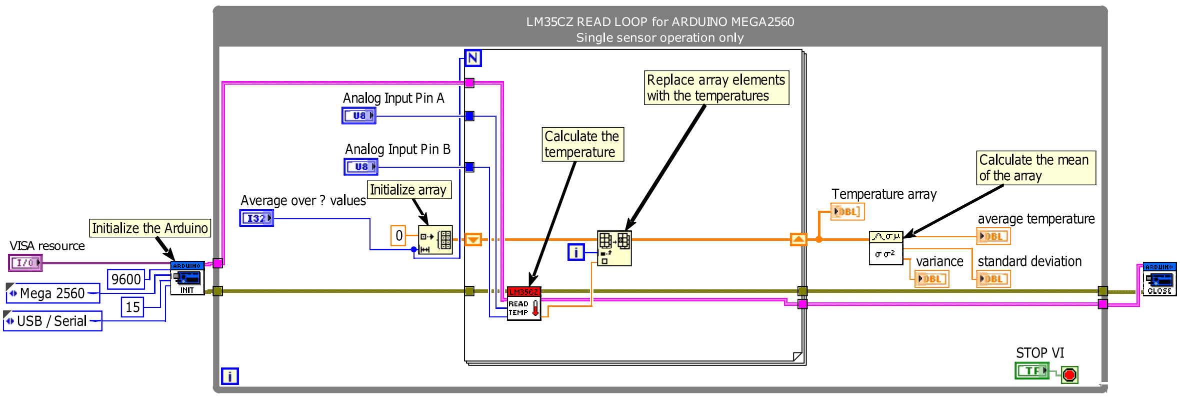

(b) LabView source code: After initialising the connection to the Arduino, the voltages from the input pins are read and converted into a temperature. Multiple temperatures are stored in an array, over which is then averaged. Also, the standard deviation and the variance are calculated. Should the VI be stopped, the connection to the Arduino is closed.

Figure 6.13.: The LabView Front Panel and the source code of the VI that was developed to read out a single LM35CZ sensor. The system is depicted in figure 6.12 as a block diagram and allows for a two-way communication between LabView and the Arduino.

6.4.5. Maxim integrated DS18B20 digital one-wire sensors

Like the previously introduced LM35 series sensors, The Maxim Industries DS18B20 (formerly Dallas Semiconductors DS18B20) devices are silicon bandgap temperature sensors. The key difference compared to the LM35 is that the DS18B20 are digital sensors.

6.4.5.1. Working principle

The following short description of the DS18B20 sensors is based on [Max15]. DS18B20 devices consist of five main parts. Each sensor has a serial number which is stored in a 64-bit read-only memory (ROM). The digital output of the temperature sensor is stored in a 2-bit scratchpad memory. The 1-byte upper and lower alarm trigger registers and the configuration register can be accessed with the scratchpad. Via the configuration registers, the resolution of the temperature-to-digital conversion can be set to either $9, 10, 11$ or $12\,\mathrm{bit}$.

A characteristic feature of the DS18B20 devices is the usage of the 1-wire bus protocol. This protocol is exclusive to Maxim's integrated circuits. The 1-wire system uses a single bus with a single *master* controlling one or multiple *slaves*. The DS18B20 devices always act as slaves. In a *single-drop* system only one slave per bus is present. In case of the existence of multiple slaves per bus, the configuration is designated as a *multi-drop* system. For a multi-drop system, the master (e.g. an Arduino microcontroller) identifies the single devices using their 64-bit serial numbers. Hence, a nearly unlimited amount of devices can be present on one bus. In general this means, that multiple DS18B20 devices can be controlled and read out with a single data line. This data line requires a pullup resistor of $\sim 5\,\mathrm{k\Omega}$, since all devices are linked to the bus via an open-drain port.

Another feature of the DS18B20 devices is, that an external power supply is not required for their operation. This is especially beneficial in space constrained environments. In the *parasite-power mode* the devices can be supplied with power via only the pullup resistor and the DQ pin. The *normal mode* features a more classic power delivery via an additional VDD pin. This mode is advised when operating under high temperature conditions and for long buses.

The transaction sequence for the DS18B20 consists of the *initialisation*, a *ROM-command* and a *DS18B20 function command*. During the initialisation phase, the master device sends a reset pulse which is answered by the slaves with a presence pulse. This gives the information, that one-wire devices are connected and ready to operate. Then, the master issues various ROM-commands. These use the unique 64-bit serial numbers of the DS18B20 and are used to specify with which device the communication should be established in case of a multi-drop system. ROM-commands can be used to determine the exact amount of sensors on the bus and their status, e.g. if an error exists. After the addressing, the master device uses DS18B20 function commands and can access (read/write) the scratchpad memory. Inter alia the power supply mode can be read or a temperature conversion can be initiated. This conversion time depends on the resolution (93.75 ms for 9-bit up to 750 ms for 12-bit).

The DS18B20 devices have been chosen due to their low cost and accuracy over a temperature range suitable for the application in the HVAC unit. Also, their required input voltages can be effortlessly provided by an Arduino microcontroller. A short overview of the technical data can be found in table 6.4.

Table 6.4.: Technical data of the Maxim Integrated digital DS18B20 one-wire sensors. Source: [Max15].

				Unit
Specified operating temperature	$T_{\text{min}} = -55 \leqslant T \leqslant 125 = T_{\text{max}}$			°C
	Condition	*Typical*	*Maximum*	
Accuracy	$-10 \leqslant T \leqslant 85$		±0.5	°C
	$-55 \leqslant T \leqslant 125$		±2.0	°C
Long term stability/drift	$T = T_{\text{max}}$ for $t = 1000$ h	±0.2		°C
		Minimum	*Maximum*	
Input voltage		3.0	5.5	V
Input voltage (pullup)		3.0	5.5	V
Temperature conversion time (12-bit resolution)			750	ms

6.4.5.2. Readout

The Maxim Industries DS18B20 digital one-wire sensors were tested in conjunction with a Sunfounder Arduino MEGA compatible board and an 830 pin breadboard. Early tests were conducted using a single sensor, later tests were done using eight and up to 40 sensors. Similar to the LM35 sensors, the required circuitry is minimal. A DS18B20 device can be directly connected to the 5 V and GND pins of the Arduino. The data pin of the sensor is connected to the 5 V pin via a 4.7 kΩ resistor and to a digital pin of the Arduino. The circuit diagram depicted in figure 6.14 corresponds with the early test setup used to read eight parallel sensors in single-drop configurations. With an Arduino, the digital one-wire sensors can be easily read out by including the `DallasTemperature` and the `OneWire` libraries into the sketch. The libraries are available from [Bur16; Sto+16]. They allow the implementation of initialisation-, ROM- and function commands in the Arduino sketch (see section 6.4.5.1).

Similar to the LM35CZ sensors, a measurement at ambient room temperature was performed. For this purpose, the whole system was isolated using the same technique as for the LM35 sensors. In this case, over a timespan of roughly 4.5 min 200 samples were acquired, which are shown in figure 6.15a. Averaging resulted in the following temperatures:

$$\begin{aligned} T_1 &= 25.44(1)\,^\circ\mathrm{C}, & T_5 &= 23.87(0)\,^\circ\mathrm{C}, \\ T_2 &= 25.14(3)\,^\circ\mathrm{C}, & T_6 &= 24.25(0)\,^\circ\mathrm{C}, \\ T_3 &= 26.25(1)\,^\circ\mathrm{C}, & T_7 &= 25.31(0)\,^\circ\mathrm{C}, \\ T_4 &= 24.56(0)\,^\circ\mathrm{C}, & T_8 &= 25.44(1)\,^\circ\mathrm{C}. \end{aligned} \tag{6.21}$$

The reading of a reference thermometer (≈ 25 °C) agreed with the DS18B20's temperatures. The measurement shows a discrete temperature distribution among the sensors, which is to be expected due to the digital nature of the DS18B20 devices. Fluctuations of 0.065 °C correspond to the resolution at 12 bit, which is the highest resolution DS18B20 devices are capable of providing. Compared to the results from the LM35CZ sensors (see equations (6.18) and figure 6.10a), the fluctuations of the temperatures are less, resulting in standard deviations that are roughly three to five times lower. Half of the sensors show no fluctuations at all. As with the LM35 series sensors, a maximum deviation of 1 °C between the sensors due to the ±0.5 °C accuracy at room temperature is expected. However, the difference between the highest reading (T_3) and the lowest reading (T_5) is 2.38 °C.

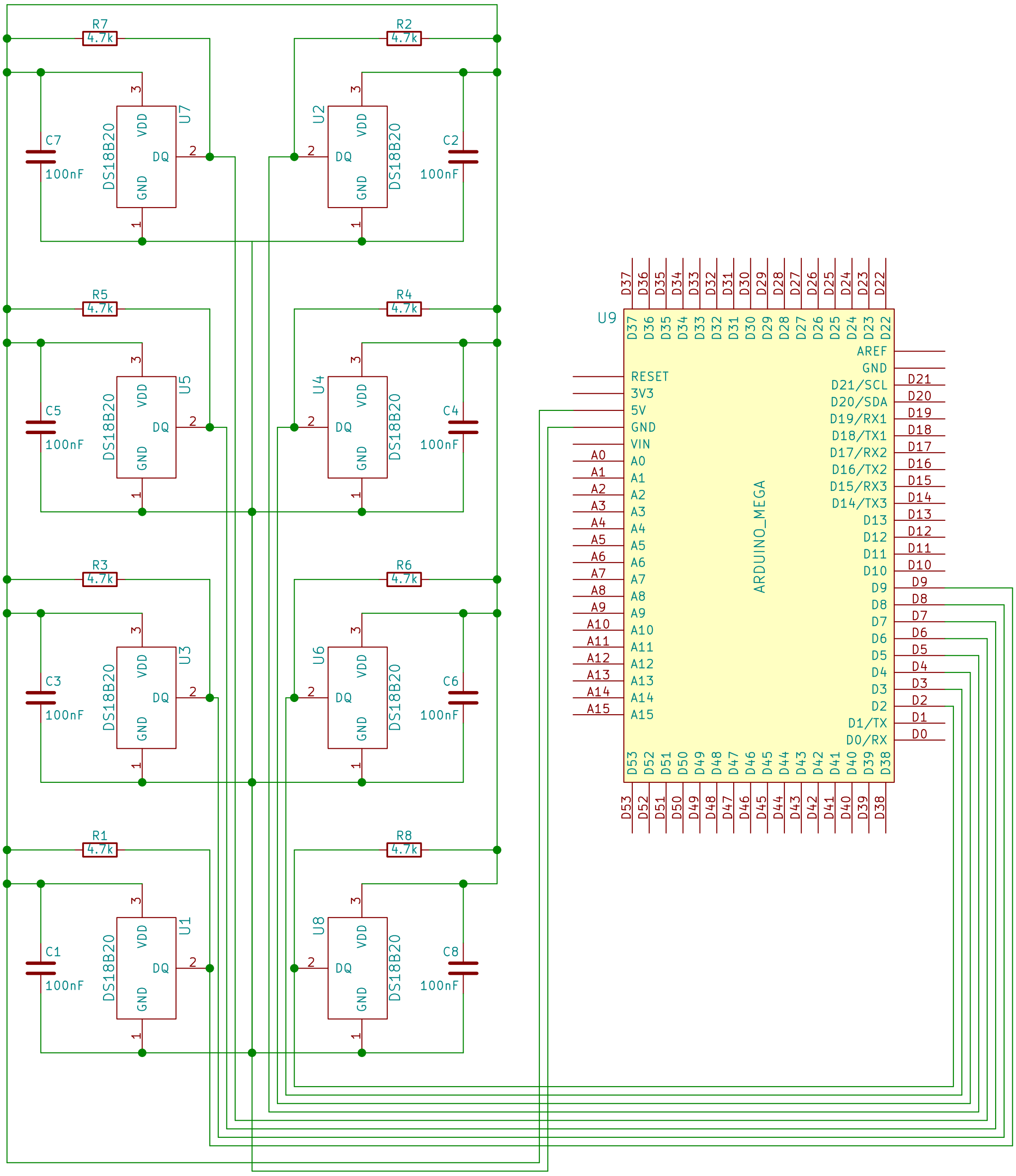

Figure 6.14.: The electric circuit used to read out eight digital DS18B20 sensors with an Arduino MEGA2560. In this case, the eight sensors are connected in eight parallel single-drop systems. Each sensor has its own decoupling capacitor.

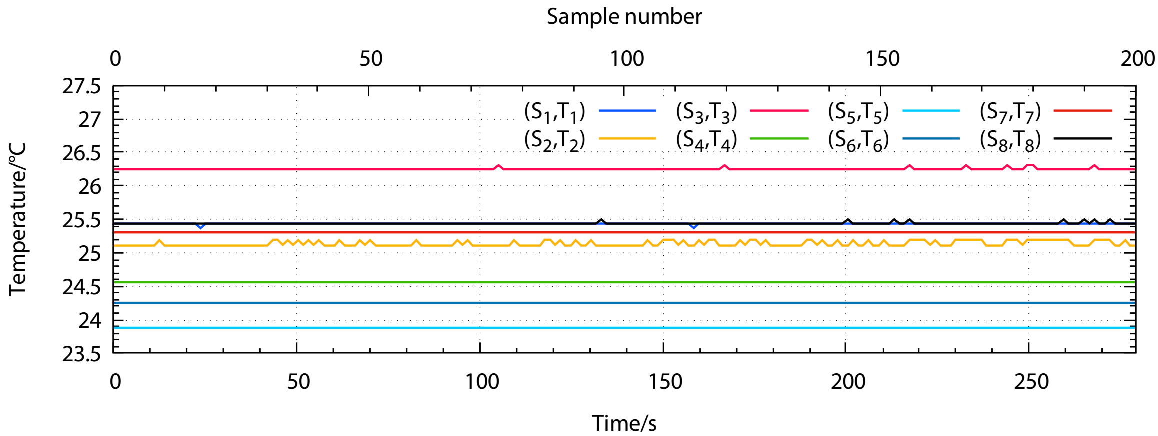

(a) Measurement at ambient temperature.

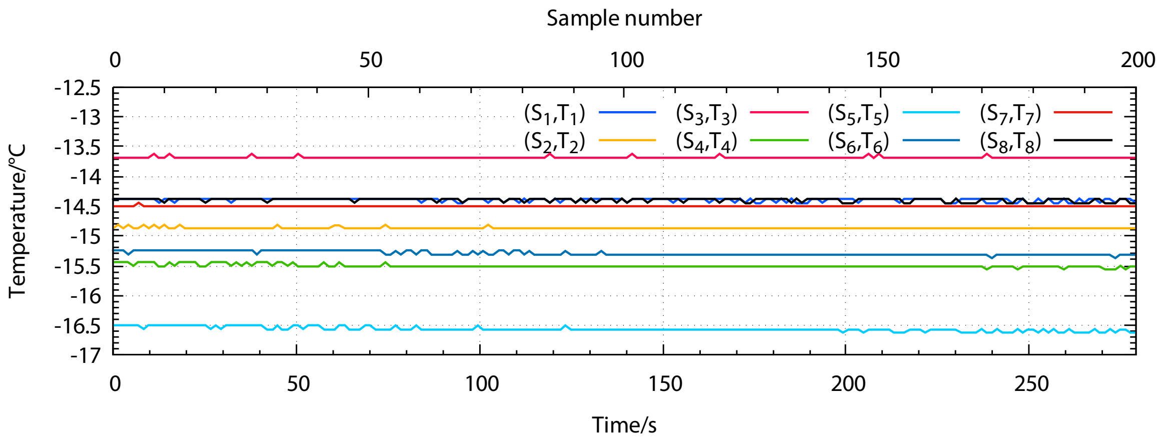

(b) Measurement under low temperature conditions.

Figure 6.15.: Two temperature measurements conducted with eight DS18B20 sensors in single-drop systems under ambient and low temperature conditions. A total of 200 samples were taken for each measurement. In both cases, the test system was enclosed in isolation material to diminish short term temperature fluctuations. Each colour corresponds to a different DS18B20 sensor S_i with its temperature T_i.

Under low temperature conditions, the reference thermometer yielded −14 °C. This reading is slightly higher than the ones provided by the DS18B20 devices (see figure 6.15b):

$$
\begin{aligned}
T_1 &= -14.39(3)\,°\mathrm{C}, & T_5 &= -16.55(4)\,°\mathrm{C},\\
T_2 &= -14.87(1)\,°\mathrm{C}, & T_6 &= -15.29(3)\,°\mathrm{C},\\
T_3 &= -13.69(2)\,°\mathrm{C}, & T_7 &= -14.500(4)\,°\mathrm{C},\\
T_4 &= -15.49(2)\,°\mathrm{C}, & T_8 &= -14.39(3)\,°\mathrm{C}.
\end{aligned}
\tag{6.22}
$$

In this low temperature scenario no major anomalies can be observed. Temperature fluctuations still remain 0.065 °C at maximum. An increase in the fluctuations frequencies is observed, which is reflected in the higher standard deviations in equations (6.22) compared to the ones in equations (6.21). The highest deviation between two sensors is 2.86 °C. In this case, this deviation is well within the expected range, as the accuracy of each sensor is reduced to ±2 °C below −10 °C.

The DS18B20 devices were tested with the same cable type used for the LM35CZ tests and the same calibration technique to deliver comparable results. Unlike with the LM35 series sensors, neither an increase of noise nor an increase of the temperatures became apparent. Other tests included mid to long-term tests at high humidity levels, where eight sensors were enclosed for roughly 20 d in an air tight container filled with water. Here, no anomalies or malfunctions could be observed.

6.4.5.3. LabView integration

Due to the digital nature of the DS18B20 sensors, a direct integration using only the functions provided by the LIFA package is not possible. The one-wire sensor can be used in combination with LabView using a community made library, which is available from [B11]. However, first tests using this unofficial library and multiple sensors were unsuccessful.

As it was considered sufficient to only read the temperatures from the sensors in LabView, a workaround has been implemented. A block diagram of the system is depicted in figure 6.16. Contrary to the system depicted in figure 6.12, the workaround features a one-way communication between the Arduino and LabView. Here, the Arduino is *not* directly controlled by LabView. Instead of running the LIFA base software, a standard Arduino sketch for the DS18B20 sensors is running on the microcontroller board. This standalone firmware reads

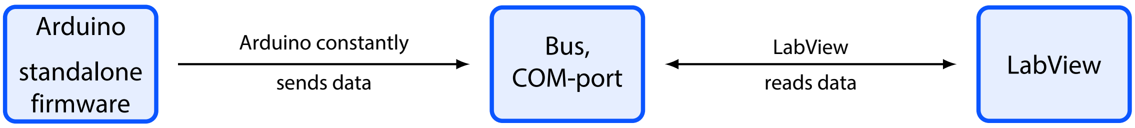

Figure 6.16.: This block diagram illustrates the one-way communication between LabView and the Arduino in the case of the implemented workaround for DS18B20 sensors. The Arduino has a full, standalone firmware that reads and transmits the temperatures via the COM-Port. A LabView program then reads the temperatures from the COM-Port.

out the sensors and transfers the data tab-delimited to the serial port. A proof of concept LabView VI is shown in figure 6.17. Essentially, it imports the data from the serial port into LabView. Therefore, the serial port is first initialised and then data is read as a string using the `VISA read` function. This spreadsheet string is then converted into an array, where each element is a temperature.

While this solution might be slightly less elegant than the one from figure 6.12 as it requires two full programs to work instead of one single VI controlling the whole system, it has one major advantage. The developed LabView VI is able to work with *any* sensor type, as it only requires the values to be transmitted tab delimited via the serial port. This means, that the VI could be used regardless of the final sensor choice.

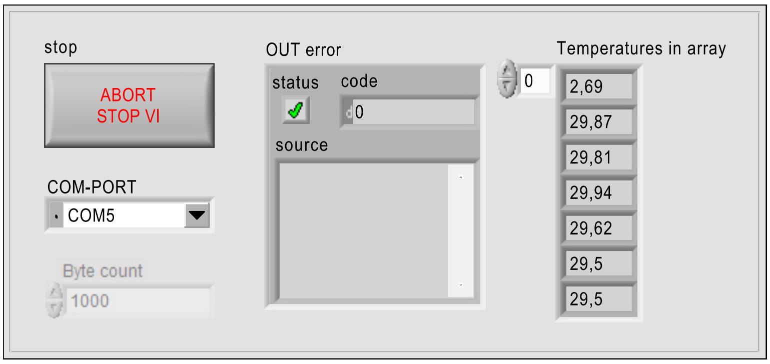

(a) Front panel: The front panel of the LabView VI that reads out multiple DS18B20 sensors. Via the "Abort Stop VI" button, the VI can be stopped. The user has to correctly set the COM-Port of the Arduino. VI errors are shown in the "OUT error" window, the temperatures are shown in rightmost array indicator ("Temperatures in array"). The first entry of the array is a timestamp. All temperatures are displayed in degrees Celsius.

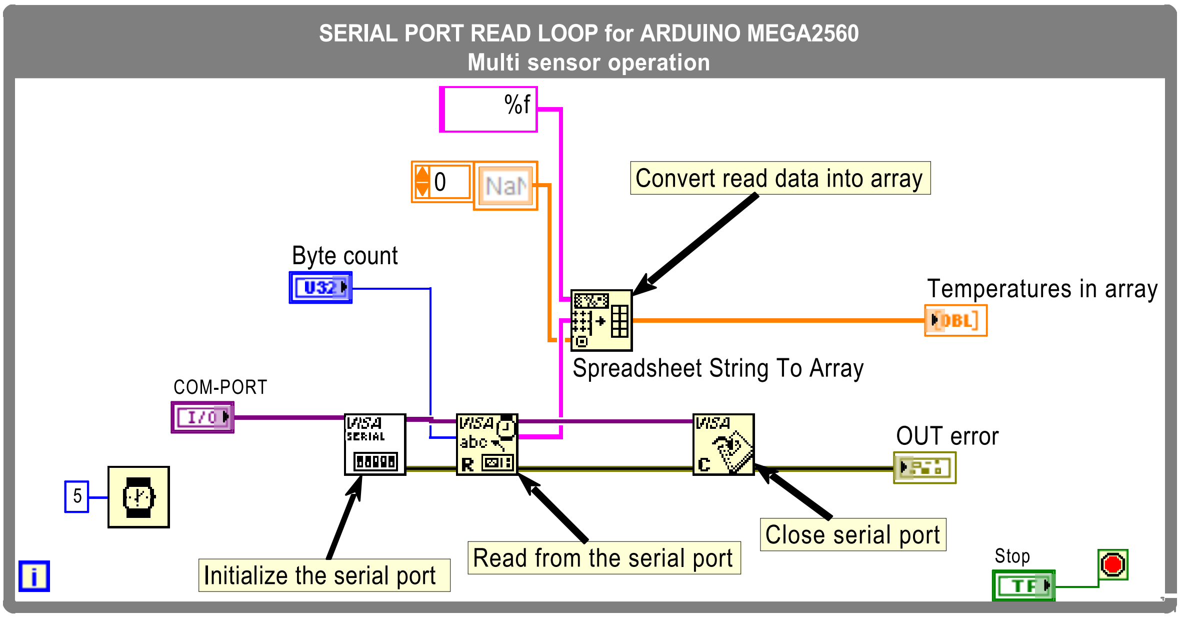

(b) LabView source code: The VI reads the temperatures provided by the sensors from the COM-port as a string. It then converts this string into an array of doubles and displays this array on the front panel.

Figure 6.17.: The LabView Front Panel and the source code of the VI that was developed to read out multiple DS18B20 sensors. The system is depicted in figure 6.16 as a block diagram and allows for a single-way communication between LabView and the Arduino.

6.4.6. Interim results and final design choices

The platinum RTDs in combination with an Arduino (see section 6.4.3) show promising results with high-resolution readings and low polling times. The circuit can be calibrated to read out a custom temperature range, improving the accuracy. However, the tested proof of concept circuit features only a 2-wire connection of the Pt-RTDs. The influence of long cables on the read temperature and the noise as well as the usage of a multiplexer allowing to read more than 16 sensors have not been examined. Compared to the other sensors, the readout electronics for the PT100/1000 sensors are more complicated and costly. Also, they require a quite complex and time consuming calibration method for each sensor. As for the integration into LabView, the VI for the LM35 sensors (see figure 6.13) can be easily modified and used for the RTDs, although this has not been explicitly tested.

The LM35CZ (see section 6.4.4) sensors require simpler readout electronics and have been successfully tested in conjunction with LabView. They feature a relatively high resolution and, theoretically, a short polling time. In practice however, the polling time is significantly increased due to the requirement of signal averaging resulting from ADC inaccuracies. Tests using various cable lengths (twisted pair cable) indicate a high increase of noise with the cable length as well as a non-linear increase of the measured temperature. For a monitoring system based on the LM35 series sensors, these factors require more research and further refinement of the circuitry. Tests using multiple sensors showed deviations of more than one degree between the sensors, requiring the need of a software based calibration or offset system.

The DS18B20 digital sensors (see section 6.4.5) need the simplest circuitry, but have a comparatively high polling time of 750 µs in theory. In the tested setup, this polling time is on par with the LM35CZ sensors. The DS18B20 show the lowest amount of noise and no dependency on the cable length. A lacking native library for LabView prevents an easy, direct and arguably more elegant LabView integration, however a workaround resulting in an indirect integration has been successful. Compared to the analogue sensors, the integration of multiple sensors of this type was easy due to the 1-wire capabilities and the Arduino's higher number of digital I/O ports. The observed deviations between sensors are higher than the ones of the LM35 series sensors, making a calibration system compulsory.

Two Arduino boards, the UNO and the MEGA2560 from different manufacturers (genuine Arduino, Sunfounder, SainSmart), were tested. While nowhere during the testing limitations concerning the computing power (see section 6.4.2) were observed, the MEGA2560 was used in the majority of cases. This was due to its enhanced I/O capabilities. The onboard memory of both boards was always sufficient during the tests, although the LIFA base firmware occupied the majority of the UNOs memory, hampering the possibility for eventual modifications or custom extensions to it. While the boards of the same type but from different manufacturers worked exactly the same, significant differences in build quality were observed. Compared to the genuine MEGA, which is the most expensive of the tested boards, especially the SainSmart UNOs quality was below-average, which may be a concern towards the board's lifetime. During testing with LM35DZ sensors, one analogue port of the SainSmart UNO consistently showed false readings, suggesting a defective I/O port.

After these considerations, the DS18B20 sensors in combination with genuine Arduino MEGA2560 boards have been chosen to realise the temperature monitoring system for the JUNO test facility. The few disadvantages of the DS18B20 devices are not critical and this solution was the most affordable of the three tested Arduino based systems. Also, the integration into LabView was successful.

The final design features some changes compared to the earlier design from figure 6.14. Instead of using a single-drop design, eight multi-drop systems are used as shown in figure 6.18. Each of these systems consists of five sensors, giving 40 sensors in total. The usage of small multi-drop configurations was found to decrease the polling time significantly compared to multiple single-drop systems. It also simplified the circuitry slightly. A single multi-drop system with 40 sensors was found to deliver occasional false readings, probably due to the large physical bus length. Furthermore, it is another single point of failure. Should the single bus loose connection to the Arduino, e.g. due to a cable break, thermomechanical strain or a damaged Arduino input port, the whole system would fail. In this regard, the implementation of multiple buses also provides a certain degree of redundancy. The final system uses LappKabel Stuttgart Unitronic® LiYY cables [Lap16] instead of the earlier used 3M ribbon cables. The specifications of this cable type vary from the specifications of the 3M ribbon cable. With the LiYY cable, the readout of five cabled (cable length: $\simeq 20\,\mathrm{m}$) sensors in a single-drop system required the pull-up resistor to be reduced from the earlier $4.7\,\mathrm{k\Omega}$ down to $1\,\mathrm{k\Omega}$ to ensure proper functionality. Instead of having the readout circuitry on a temporary breadboard, the final system uses a printed circuit board (PCB). Figure 6.19 shows a two-dimensional rendering of this PCB.

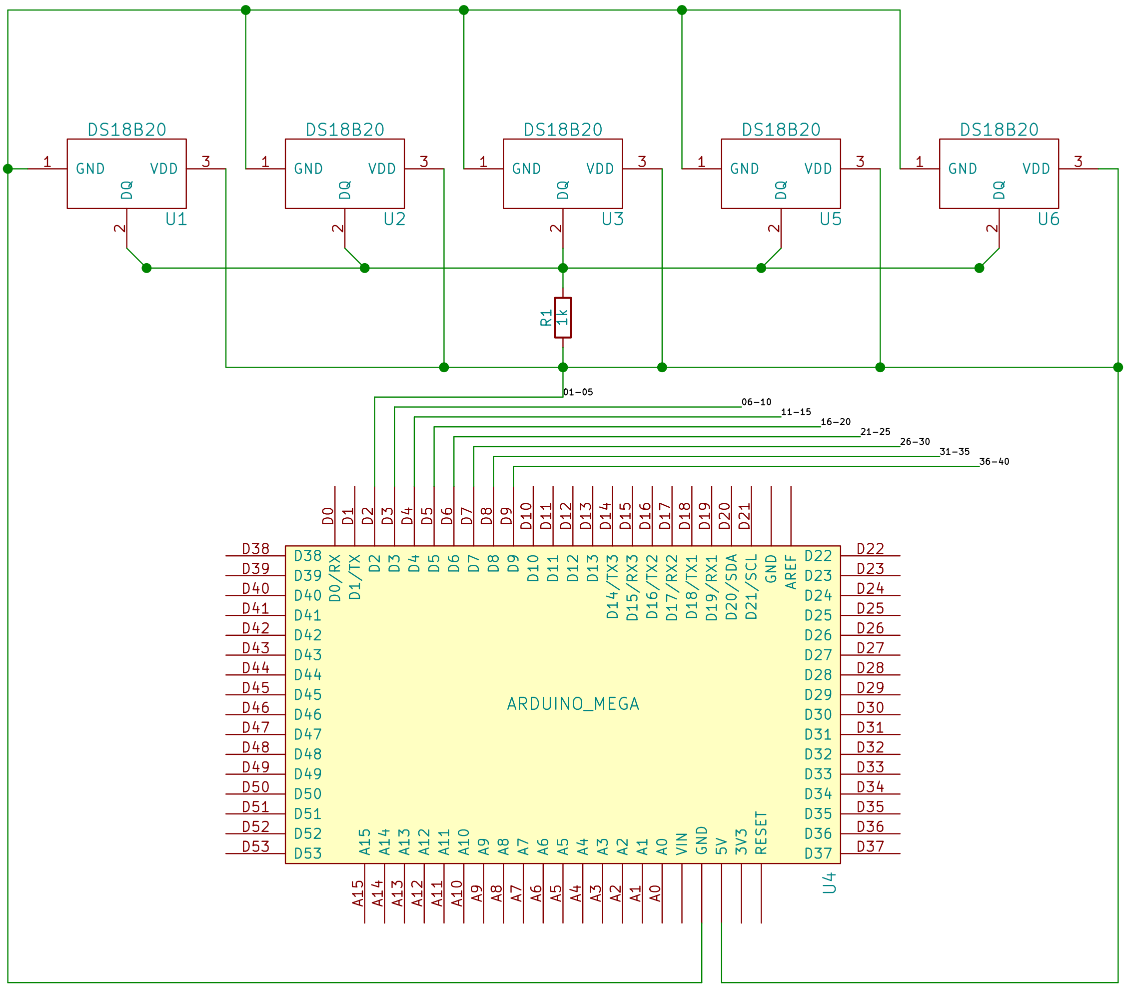

Figure 6.18.: Final scheme of the electric circuitry used to read out 40 Maxim Integrated DS18B20 devices. This setup features eight multi-drop systems consisting of five sensors each. One of these multi-drop systems is explicitly depicted and connected to digital input D2. The remaining seven are only suggested (digital pins D3-D9) but designed equally. All sensors in all multi-drop systems are provided with power by the Arduino board. Compared to figure 6.14, the decoupling capacitors are no longer present. This has no influence on the readout.

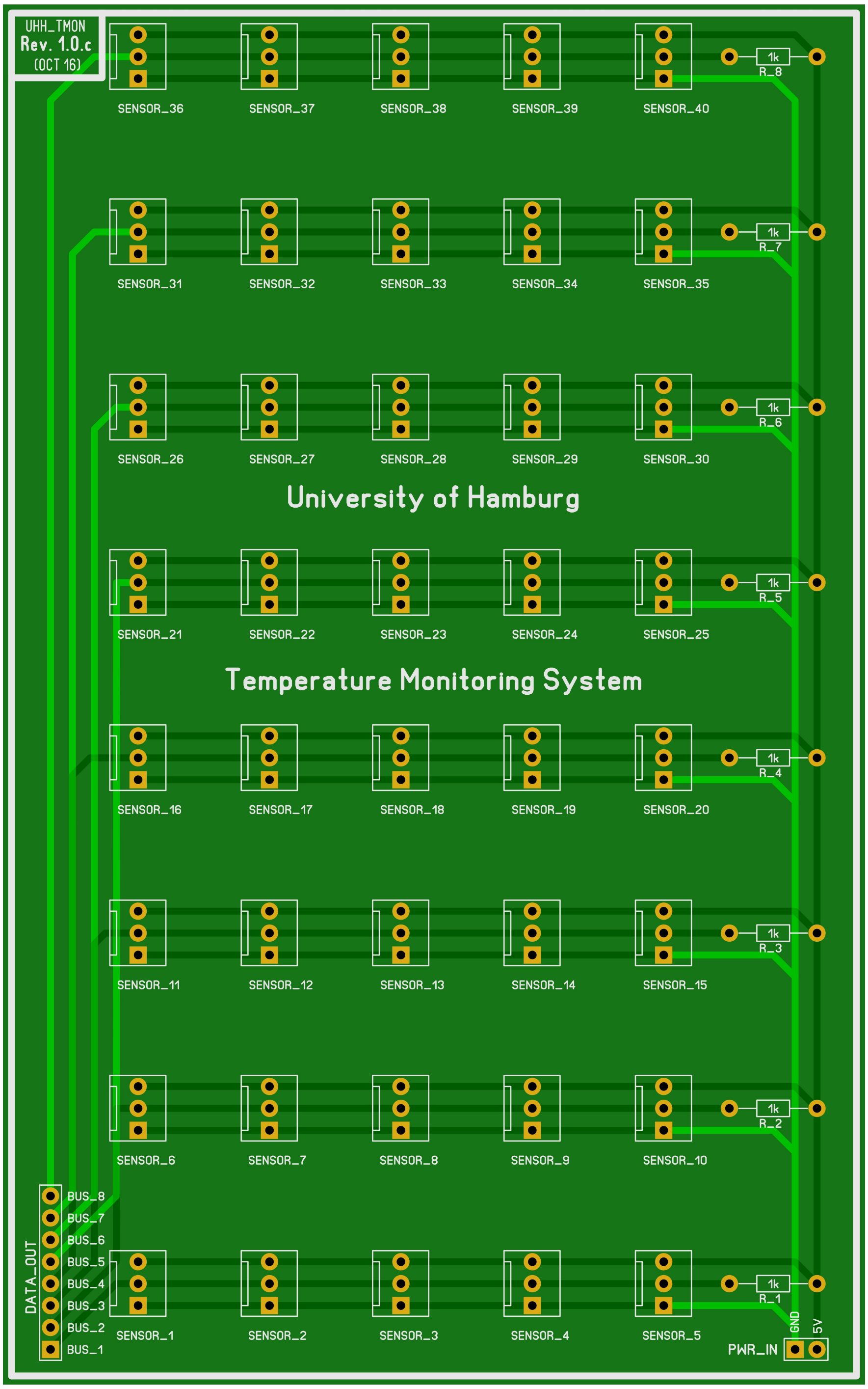

Figure 6.19.: Two-dimensional rendering of the component side of the dual-layer PCB (length×width: 160 mm×100 mm) for the temperature monitoring system with sketched headers, connectors and resistors. Bottom layer traces are depicted in dark green and top layer traces in light green. Eight multi-drop-systems hold five sensors each. The PCB design and the rendering were created using Sprint Layout Version 6.0.

6.5. Final LabView integration

A basic proof-of-concept program to read the DS18B20 sensors has already been developed (see figure 6.17). This program has been improved concerning functionality and user friendliness. In this section the basic working principle and the features shall be briefly discussed. Due to the extent of the LabView VI, the full code shall not be listed here. However, a flowchart illustrating the VI's operational sequence is shown in figure 6.20.

The core of the program is the VI that has already been described in section 6.4.5.3. It reads the temperature data from the serial port and writes them into a LabView array that can be displayed on the front panel. In the final VI, this array is not used to display the temperatures on the front panel. Instead, a function is used that extracts each array element separately and displays each temperature in its own independent indicator. Although this makes the code much more complex, it allows the temperature indicators to be designated with a colour coding, improving the clarity of the user interface. Due to LabView limitations, this could not be done with an array of indicators.

One requirement of the program is to calculate the mean of the temperatures, as it is considered to eventually use it to control the HVAC unit. In order for faulty data or wrong readings not to affect the mean, an error handling functionality is implemented. Therefore, the user can set low and high setpoint temperatures ($T_{\mathrm{SP-}}$, $T_{\mathrm{SP+}}$). Should a temperature not be inside this range, i.e. $T \notin [T_{\mathrm{SP-}}, T_{\mathrm{SP+}}]$, it will be ignored in the calculation of the mean. Such temperatures are flagged with the string `Warning` and are shown in orange on the front panel. A faulty connection between the Arduino and the DS18B20 sensors yields a reading of $T_{\mathrm{INOP}} = -127\,°\mathrm{C}$. Temperatures, which fulfil $T = T_{\mathrm{INOP}}$ are flagged with the string `INOP` (inoperative). These are also excluded from the calculation of the mean. On the front panel, they are marked in red and flash repeatedly. This set of criteria forms the first stage of data filtering.

The second stage of the filter ensures, that temperature readings which deviate more than a multiple of the standard deviation from the mean temperature are excluded from the mean calculation. Therefore, the mean $\overline{T}$ of the filtered array and its standard deviation σ_{T} are calculated. Then, for each array element the condition

$$T \in [\overline{T} - n\sigma_{\mathrm{T}}, \overline{T} + n\sigma_{\mathrm{T}}] \tag{6.23}$$

is checked. Here, n is a user-set variable ("deviation multiplier" on the front panel). If this statement does not hold true, the element is removed from the array, flagged with the string `Deviation` and highlighted in yellow on the front panel. If and only if a temperature satisfies condition (6.23) it remains in the array. Such temperatures are marked as `OK` and shown in green on the user interface. Then, the mean and standard deviation after this second stage of the filter are computed. This concludes the error handling function of the monitoring system's VI. On the front panel, this function can be activated or deactivated by the user.

Another implemented feature is the ability to define offsets for each individual sensor. Tests using multiple sensors (see section 6.4.5) indicated, that the need for a function to set offsets for the sensors is compulsory. Therefore, an array of controls has been implemented on the front panel, where each control corresponds to a single sensor. These controls can be accessed by changing to the "Calibration panel" tab on the top of the front panel. Programatically, this offset array is added to the array read from the serial port.

Feature-wise, data logging capabilities are added to the LabView program. The raw data that is read from the serial port can be written into a data file. From the front panel, a desired file path can be set by the user. The function has been tested to save the files in `.txt`, `.dat` and `.asc` formats. Corrected data, i.e. the raw data plus the data from the offset array, can also be saved to a different text file. The data logging functions for raw and corrected data can be enabled/disabled separately using two switches on the user interface.

In order to allow for easy tracking of the temperature profile, a graph is implemented. It shows the temporal progression of each corrected temperature individually. The graph overview can be examined by changing the view on the front panel to "Chart" using the tab control.

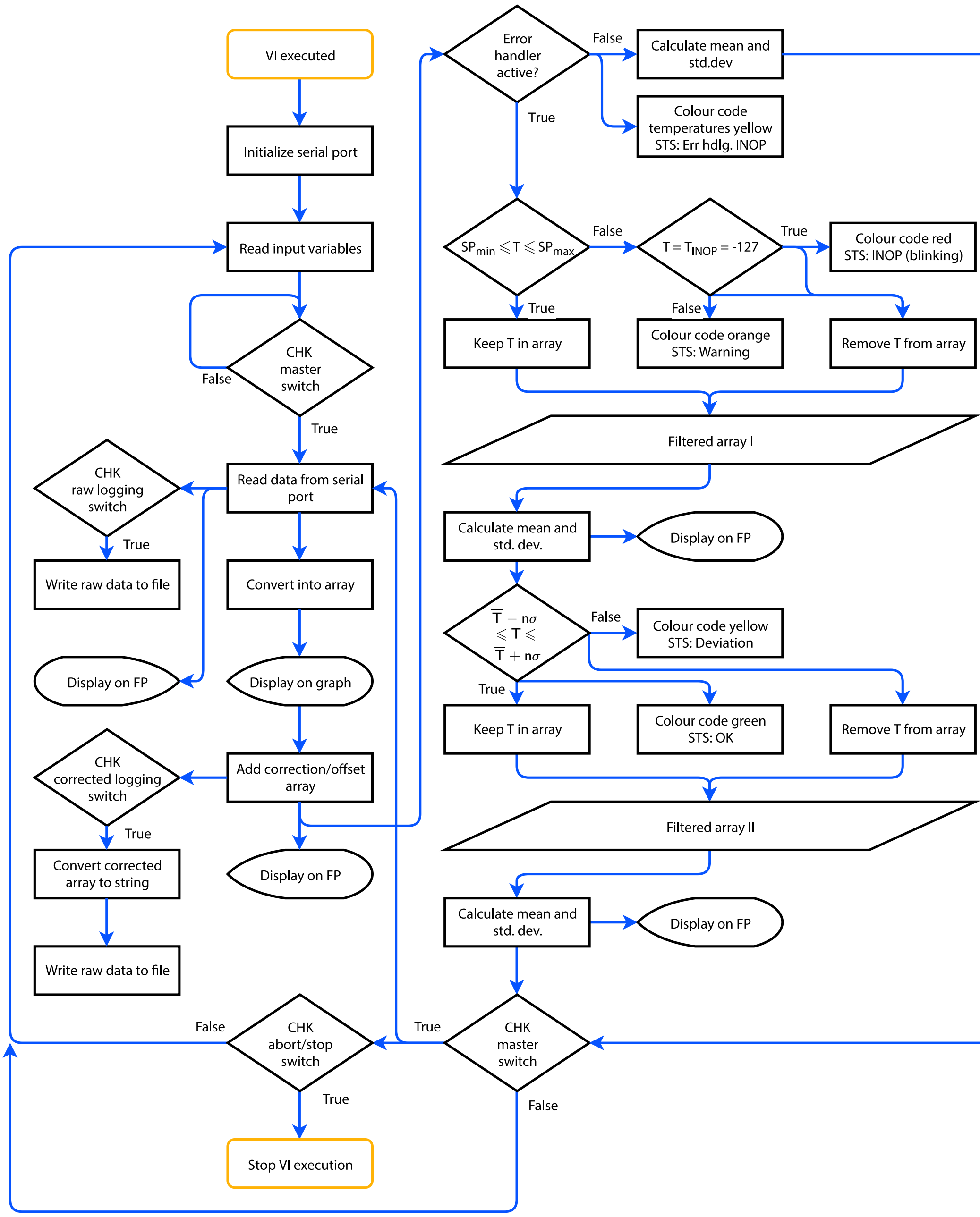

Figure 6.20.: This flowchart depicts the operational sequence of the LabView VI that has been developed for the final temperature monitoring system based on DS18B20 sensors. For reasons of clarity, the processes associated with LabView internal errors (VI errors) are not illustrated. In the case of switches, the booleans true/false correspond with the states on/off. Abbreviations: Check (CHK), front panel (FP), setpoint (SP), status (STS), inoperative (INOP).

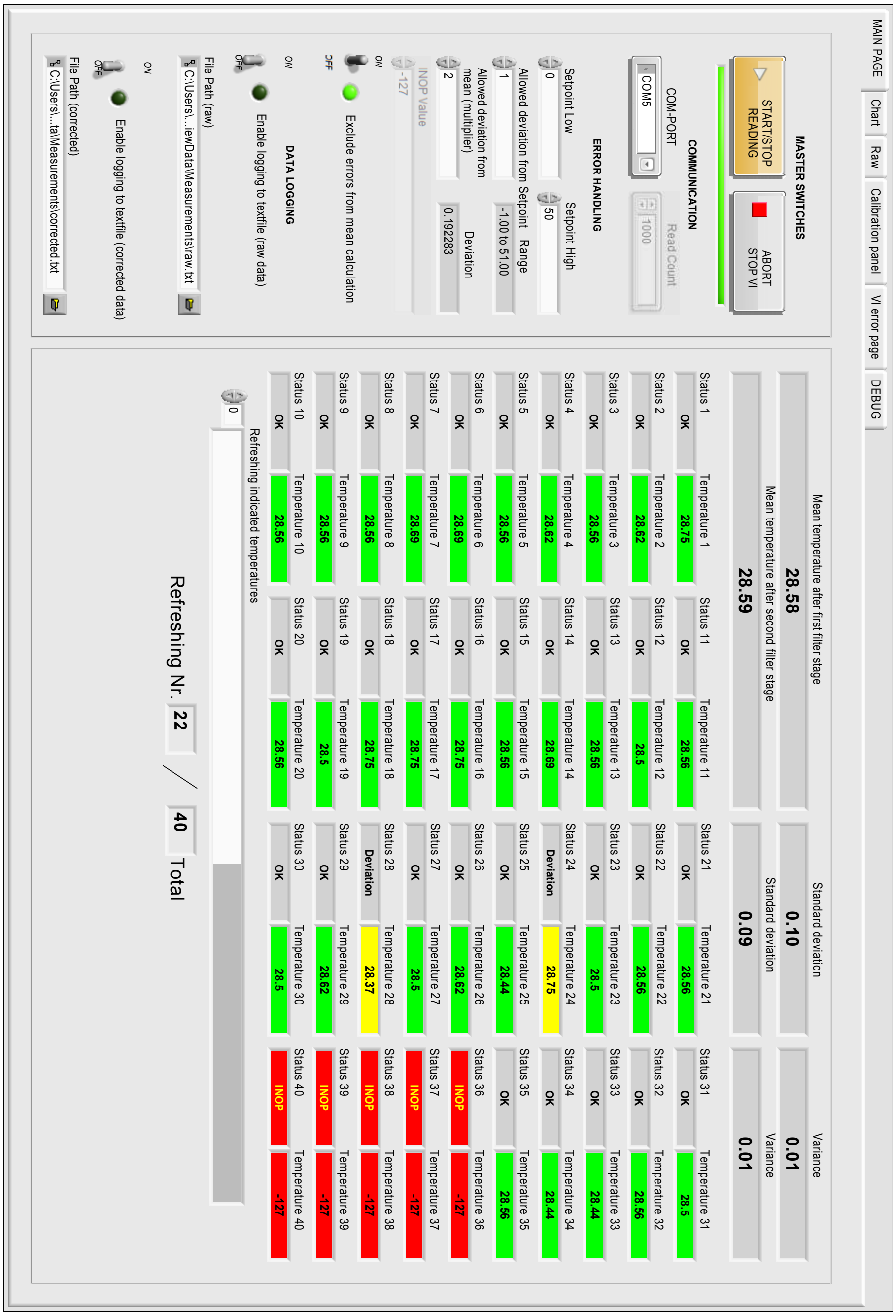

Figure 6.21.: The main page of the front panel of the LabView VI used to read out 40 DS18B20 sensors. On the left side, various controls allow to set up the connection to the Arduino and activate data logging and error handling features. On the right side, the temperatures as well as their averages are shown. Temperatures are colour coded depending on different conditions. At the top, multiple tabs allow to switch between different menus which allow to monitor the temperatures in a chart, monitor the raw temperatures, view errors or to calibrate the sensors. The shown front panel is part of a late beta version. The tab "DEBUG" will be removed in the final release.

7 Implementation of a remote control system

As already mentioned in the previous chapters, the test facility for the JUNO photomultipliers is equipped with an HVAC unit that allows to control the inside temperature. This HVAC unit is controlled and monitored by a Siemens LOGO! programmable logic controller (PLC) equipped with an external text display (LOGO! TDE) that is mounted on the outside of the container. Various PT100 sensors (see section 6.2.1) monitor the temperature of different parts of the HVAC unit. Also, the inside and outside temperatures are monitored, each by a single sensor. The set temperature can be manually changed via hardware buttons on the LOGO! TDE. This chapter explains the remote control system implemented for the test facility's HVAC unit. After section 7.1 introduces the goals and targeted features of the system, the LabView integration and known issues are described in sections 7.2 and 7.3.

7.1. Goals and motivation

A remote control system for the HVAC unit simplifies the operation of the test facility. Some PMTs will be artificially aged by increasing and decreasing the temperature periodically, which also requires a remote control system. The Siemens LOGO! controller can be accessed through an Ethernet interface. The main goal of the remote control system is to allow the user to set a temperature via the Ethernet port while retaining the ability to manually change the temperature via the hardware buttons on the LOGO! controller itself. Also, the temperatures of the various components of the HVAC unit should be read out via the remote control system. Another aim of the system is to allow the user to start/stop the unit as well as log the data to a file or display them graphically in order to provide an overview of the temporal progression of the temperatures. Moreover, the remote control system should provide the user with information about eventual error statuses of the HVAC unit.

7.2. LabView integration

Due to the PMTs and the temperature monitoring system being read out with LabView, the remote control system was also realised with LabView. As with the LabView integration of the DS18B20 sensors (see sections 6.4.5.3 and 6.5), a direct integration was not possible due to the Siemens proprietary LOGO! software not providing built-in LabView compatibility. Thus, another indirect solution was found.

The core part of the developed program is an Application-Programming-Interface (API) that has been developed by the National Instruments Community allowing to link a LOGO! based system to a LabView VI [Nat09]. The API is able to monitor the Ethernet data flow put out by the LOGO! controller. With the API, specific data blocks integrated into the LOGO! controllers source code can be read out. The API is embedded in the developed remote control VI. To establish the connection between it and the LOGO! system, the IP-address of the target system has to be set properly on the VI's front panel (see figure 7.2, annotation ②).

The built-in temperature sensors of the HVAC unit are connected to the analogue inputs $\{\mathrm{AI}_j \mid j = 1, 3, 4, 5, 6\}$ of the LOGO! PLC. The analogue input AI_2 is unallocated. In the LOGO! software, these inputs have a unique variable memory (VM) address. These addresses are passed to the LabView API, allowing to read the analogue input values. In LabView, this yields an array of various pairs of two bytes (b_1, b_2). Each pair of bytes corresponds to a specific analogue input value x_{AI_j}, which is made up as follows:

$$x_{\mathrm{AI}_j} = 255 b_1 + b_2. \tag{7.1}$$

From this equation, the temperature T_{AI_j} can be determined via

$$\frac{T}{°\mathrm{C}} = \frac{x_{\mathrm{AI}_j}}{4} - \begin{cases} 100 & \text{for } j = 1, \\ 50 & \text{for } j \in \{3, 4, 5, 6\}. \end{cases} \tag{7.2}$$

This system is used to display the inside air temperature (AI_1), evaporator temperature, supply air temperature as well as the exhaust and outside temperatures (AI_3 to AI_6) on the front panel (figure 7.2, ⑧).

The set temperature can be adjusted using the control ⑦ on the front panel. Right next to it is an indicator showing the current set temperature allowing to cross check or verify the set value. Programatically, the set temperature is stored in a specific, VM-addressed data block in the LOGO! code. Consequently, a value can be written to the block via the LabView API. Here, similar to equation (7.2), an offset of 100 has to be considered. This is programatically done in the VI.

In order to start/stop the cooling or heating process, a hardware button on the LOGO! text display has to be pressed. This button could not be addressed via VM-mapping. Thus, a workaround via a VM-mappable analogue threshold switch is implemented. It outputs a logical value depending on the input value and the set threshold. If the input value is less than the threshold, the output is a logical zero, if the input value exceeds the threshold the output is a logical one. In the LabView VI, the API is used to write a value exceeding the threshold to the PLC, followed by a value that is less than the threshold. This is streamlined in the VI so that the HVAC unit can be started or stopped via a toggle switch ③. The implemented solution uses an OR-gate in the LOGO! code, and thus still allows the user to start/stop the cooling or heating process from the hardware button on the LOGO! TDE.

Various control indicators (see ④) are implemented into the VI to allow monitoring the current status of the container. The first LED ("Run status") indicates, whether the cooling or heating operation is active. For the realisation of this feature, a digital marker is added to the corresponding LOGO! code. This marker outputs either a logical 0 or a logical 1, depending on whether the code section is active or inactive. Addressing the marker makes this output value accessible in LabView using the aforementioned API. The exact same technique is used to indicate, whether the HVAC unit is currently initialising or if an error exists. With this solution, it is currently only possible to read, whether or not an error exists. The specific cause of the error can not be displayed in LabView but only on the LOGO! TDE. However, this drawback is not considered to be severe, as the HVAC unit requires a full manual reset by disconnecting it from the mains as well as a reboot after the occurrence of an error. Both of these measures can only be performed via hardware switches on the container itself.

Similar to the temperature monitoring system discussed in section 6.5, the remote control system offers the possibility to display the temperatures in a graph (see ⑥) and log them, including a time stamp, to a file. The data logging feature can be activated in ⑤ and saves the data to a file at the user specified path. Tested file extensions include `.txt`, `.dat` and `.asc` formats. It is currently discussed, how this data logging feature can be improved, for example by integrating it into a SQL database system.

Another feature currently being considered is the possibility to access the LabView VI's front panel via the internet. Currently, the container can be controlled via the VI from any computer in the same network as the LOGO! controller that runs an installation of LabView. LabView offers a built-in function to host the VI on a local computer, making it accessible from any PC in the network. However, remote servicing and monitoring of the container may require the access from different networks. For this, a standalone website with the front panel built in could be implemented. Questions concerning security (e.g. password protection) and data security are currently being investigated.

7.3. Known issues

In spite of all efforts, the remote control system currently has some known issues. Strictly speaking these issues are, however, not impairing the functionality. Firstly, the developed VI does perform relatively slowly. This is due to the fact, that the API's read and write function needs a delay time of at least 1000 ms between each call. In the VI, the read/write function of the API is called up to six times per cycle, resulting in an eventual delay of up to six seconds between a user input and the input being processed. While this does not significantly hamper the functionality, it requires some streamlining in order to improve the user experience and simplify the operating process. Should the remote control VI be turned into a SubVI and be implemented into another VI, this issue definitely needs to be addressed, as other VIs or processes might require a faster operating sequence.

Secondly, the developed VI is currently not a plug-and-play system, meaning that the proper execution of the VI requires a preparatory step. By default, the API cannot connect to the LOGO! target system, because the IP address is not recognised by the system. Via the Siemens LOGO! Soft Comfort Software, a connection to the LOGO! PLC has to be configured first. After that, the IP address is recognised by the remote control VI. This behaviour was observed on various different computers and is probably a Windows 7 operating system (OS) related issue, where the IP address first has to be communicated to the OS via the LOGO! software. This would also explain the fact that prior to setting up the connection via the LOGO! software, the LOGO! PLC cannot be pinged via the Windows console.

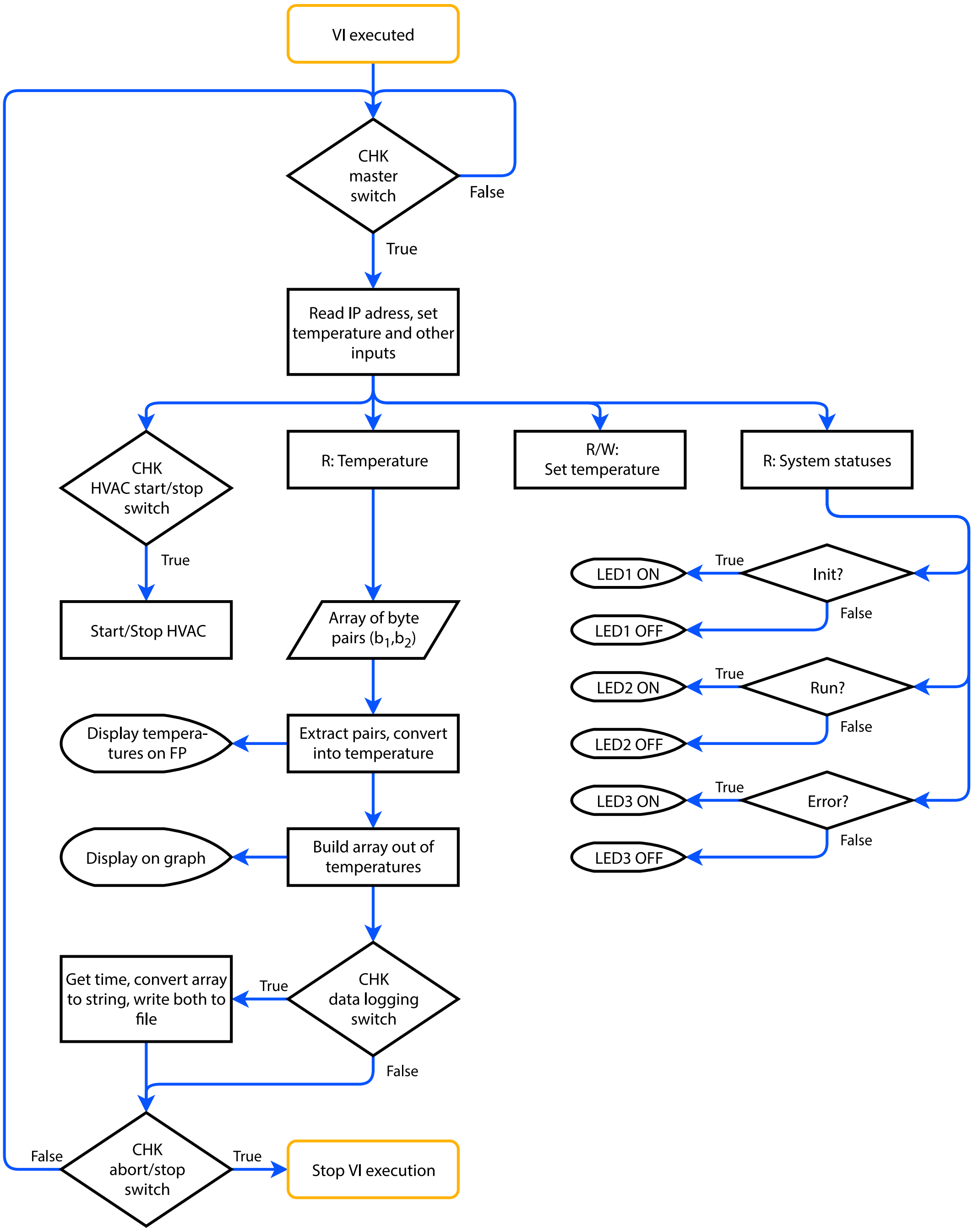

Figure 7.1.: This flowchart depicts the operational sequence of the LabView VI that has been developed to remotely control the HVAC unit of the test stand. For reasons of clarity, the processes associated with error handling are not depicted. In the case of switches on the front panel, the booleans true/false correspond with the states on/off. Abbreviations: Check (CHK), front panel (FP), read (R), write (W), read and write (R/W), initialise (Init)

Figure 7.2.: The front panel of the LabView VI allowing to remotely control the HVAC unit of the test stand. The main controls allowing to set up the connection ② to the HVAC unit, start reading the actual temperatures ① as well as start/stop the heating/cooling process ③ and activate data logging features ⑤ are located on the top left. Next to the start/stop buttons, three indicators ④ are placed showing the current status of the HVAC unit. On the top right, the set temperature can be adjusted ⑦ and the read temperatures ⑧ as well as VI errors ⑨ are shown. A graph in the bottom ⑥ shows the temporal progression of the read temperatures.

Conclusion and outlook

Within the course of this thesis, a test facility to characterise JUNO photomultiplier tubes was commissioned. Here, the main target was to implement a temperature monitoring system. For this purpose, various different systems and sensors were tested. The first system was based on a programmable logic controller manufactured by Beckhoff. While a PLC-based system is rather excessive for a pure temperature monitoring system, it is the most future-proof, as it can be easily expanded. However, the tested Beckhoff system did not turn out to be a satisfactory solution, mainly due to the fact that a reliable connection to the bus controller via Ethernet could not be established. As an alternative, different Arduino microcontroller boards and different sensors were assessed. Specifically, the Arduino UNO and MEGA2560 boards in conjunction with PT100/1000, LM35 and DS18B20 sensors were tested. After an evaluation of the different combinations, the Arduino UNO was disregarded mainly due to its reduced I/O capabilities. The PT100/PT1000 sensors, while being in theory the most accurate, showed promising results. However, a system based on these sensors would have required a comparatively more complex circuit as well as an elaborate calibration process. The LM35 series sensors, while requiring an easier circuit, showed complications in combination with longer cable runs. Here, a sensor with a 20-m long cable indicated a temperature that was 6.87 °C higher than the reading of a sensor without a cable. The readings of two sensors at ambient temperature without cables deviated by 1.61 °C, which was more than the expected deviation and would have required a calibration system. While the issues concerning cable length could have been resolved by modifying the circuit, the final system was implemented utilising the digital DS18B20 sensors. They showed no reliance on the cable length and required similarly straightforward readout electronics. An adequate accuracy was noted, however an average deviation of 2.86 °C between two sensors was observed, rendering a calibration system compulsory.

The system was successfully integrated into LabView. The developed VI does not control the Arduino, but rather reads the data that is transmitted by the Arduino to the serial port.

This workaround was necessary, because for the DS18B20 a native LabView library was not available. The development of the LabView VI is practically finished and allows to read and display the temperatures in a clear user interface. Moreover, it can display the temperature profile in a graph and provides a simple data logging feature. Here, the developed VI can be extended in the future. Currently, the data logging feature is limited, as it only allows to save the temperatures to a data file. However, the temperatures might later be saved in a digital database. Thus, a feature to automatically write the temperatures read in LabView to a database can be realised.

While the LabView VI provides a basic feature that allows to calibrate the sensors, the actual calibration still remains to be performed. Without any changes to the VI, a *single-point calibration* can be performed. Therefore, the reading of a sensor has to be compared with the reading of a reference sensor. The difference of the two readings can then be entered as an offset in the “Calibration panel” of the VI (see figure 6.21). Such a single point calibration can be easily performed utilising a bath of ice water. For more precise calibration techniques, such as a *two-point calibration*, the LabView VI will need slight modifications in the future. To perform a two point calibration, the readings of a sensor at two different temperatures need to be taken. Via a comparison of these two readings with the readings of a reference sensor at the same temperatures, a two point calibration is not only able to correct offset errors, but also slope errors. The mathematical function that calculates the slope and error corrections as well as the user interface which will allow to enter the required raw and reference readings are currently not yet incorporated, but can be implemented rather easily by modifying the existing calibration function. Such a two-point calibration may be performed utilising a bath of ice water for the first reading and a bath of boiling water for the second reading.

Besides the development of a temperature monitoring system for the JUNO test stand, a remote control system for the HVAC system of the test stand was successfully implemented with LabView. This system reads and writes specific data blocks to the HVAC unit’s LOGO! software, allowing to set the temperature as well as read the status of the container. The developed VI is equipped with the same data logging and display features as the dedicated monitoring system. The remote control system has a clear user interface and works stable once set up properly. In future however, several aspects of this program, especially the known issues which were discussed in chapter 7, can be improved or remedied. At the moment, the performance of the VI is subpar, due to the fact that the read/write function of the VI requires a delay of at least one second between each call. Also, the connection to the LOGO! system has to be initialised using the LOGO! software first before the VI works properly. In future, this initialisation step can be integrated directly into the LabView program. As for the temperature monitoring system, a database integration of the system is another aspect that may be added to the VI in the future.

Moreover, both VIs can be integrated into a web-based framework, e.g. a website. This will allow to access the monitoring and remote control systems from virtually anywhere and would significantly simplify eventual remote diagnosis and management. LabView provides a web-publishing feature that was tested successfully. However, the website could only be accessed by clients within the same network. An important aspect that has to be considered concerning the implementation of such a web-based system is data security.

The magnetic field strength inside the test stand was determined before and after the container was fitted with a passive soft iron shielding. For this purpose, an accurate fluxgate sensor was used. The measurements indicated that before the shielding was applied, the field strength in the interior of the test facility was roughly equal to the earth's magnetic field. After the shielding was applied, the field strength was reduced to around 6 % of the earth's magnetic field. It was therefore shown that the shielding was applied properly and functions as intended, complying with the targeted reduction to at least 10 % of the terrestrial magnetic field. In future, the magnetic field needs to be measured in each of the drawers for the PMTs after all of the electronic components are completely installed. This is to ensure that the magnetic fields created by the readout and monitoring electronics do not significantly affect the magnetic field inside the test stand and will ultimately show that the magnetic shielding is ready for operation.

To sum up, a temperature monitoring and a remote control system for the JUNO test facility were developed. Additionally, it was shown that the magnetic field strength inside the test stand is reduced sufficiently to ensure proper PMT functionality. Thus, the work performed within the scope of this thesis allows the PMTs to be tested in a controlled environment.

Apart from that, measurements with two small test stands, which shall ultimately reproduce the characteristics of the JUNO mass test stands, were performed. For both small test stands dark count measurements with two different PMTs were executed. In order to reduce the noise, a coincidence circuit was implemented and tested with one of the PMTs. The measurements showed an unexpected behaviour. A closer investigation revealed, that the signal rate was significantly lower than the coincidence rate, implying an error in the setup or a malfunctioning component. Resolving these errors will require a step-by-step troubleshooting process in the future. To begin with, coincidence measurements with the current setup but without the LED can be repeated in the future. A comparison between such measurements and the already performed measurements will give some indications about the performance of the LED. Also, the pulse width and the pulse length can be increased in order to diagnose the issues. Moreover, an oscilloscope may be used to cross check whether the PMT registers a signal from the LED. In total, these troubleshooting steps are fairly elaborate and were thus not performed within this thesis.

A PT100/PT1000 resistance lookup tables

Table A.1.: Lookup tables for resistance values of PT100 and PT1000 sensors for a temperature range of $-50\,°C \leqslant T \leqslant 50\,°C$. The first column indicates the temperature in degrees Celsius. By adding the desired temperature from the first row, the corresponding resistance of the RTD can be determined. All resistance values are given in ohms.

(a) PT100

T in °C	+0°C	+1°C	+2°C	+3°C	+4°C	+5°C	+6°C	+7°C	+8°C	+9°C
-50.00	80.31	80.70	81.10	81.50	81.89	82.29	82.69	83.08	83.48	83.87
-40.00	84.27	84.67	85.06	85.46	85.85	86.25	86.64	87.04	87.43	87.83
-30.00	88.22	88.62	89.01	89.40	89.80	90.19	90.59	90.98	91.37	91.77
-20.00	92.16	92.55	92.95	93.34	93.73	94.12	94.52	94.91	95.30	95.69
-10.00	96.09	96.48	96.87	97.26	97.65	98.04	98.44	98.83	99.22	99.61
0.00	100.00	100.39	100.78	101.17	101.56	101.95	102.34	102.73	103.12	103.51
10.00	103.90	104.29	104.68	105.07	105.46	105.85	106.24	106.63	107.02	107.40
20.00	107.79	108.18	108.57	108.96	109.35	109.73	110.12	110.51	110.90	111.29
30.00	111.67	112.06	112.45	112.83	113.22	113.61	114.00	114.38	114.77	115.15
40.00	115.54	115.93	116.31	116.70	117.08	117.47	117.86	118.24	118.63	119.01
50.00	119.40									

(b) PT1000

T in °C	+0°C	+1°C	+2°C	+3°C	+4°C	+5°C	+6°C	+7°C	+8°C	+9°C
-50.00	803.06	807.03	811.00	814.97	818.94	822.90	826.87	830.83	834.79	838.75
-40.00	842.71	846.66	850.62	854.57	858.53	862.48	866.43	870.38	874.32	878.27
-30.00	882.22	886.16	890.10	894.04	897.98	901.92	905.86	909.80	913.73	917.67
-20.00	921.60	925.53	929.46	933.39	937.32	941.24	945.17	949.09	953.02	956.94
-10.00	960.86	964.78	968.70	972.61	976.53	980.44	984.36	988.27	992.18	996.09
0.00	1000.00	1003.91	1007.81	1011.72	1015.62	1019.53	1023.43	1027.33	1031.23	1035.13
10.00	1039.03	1042.92	1046.82	1050.71	1054.60	1058.49	1062.38	1066.27	1070.16	1074.05
20.00	1077.94	1081.82	1085.70	1089.59	1093.47	1097.35	1101.23	1105.10	1108.98	1112.86
30.00	1116.73	1120.60	1124.47	1128.35	1132.21	1136.08	1139.95	1143.82	1147.68	1151.55
40.00	1155.41	1159.27	1163.13	1166.99	1170.85	1174.70	1178.56	1182.41	1186.27	1190.12
50.00	1193.97									

B Used software

Within the scope of this thesis, various software were used to control microcontrollers or to evaluate and analyse data. The following sections give a short overview of these programs.

B.1. LabView

The following descriptions of LabView is based on [GM11; PR10]. National Instruments™ LabVIEW is an abbreviation for *Laboratory Virtual Instrument Engineering Workbench*. It is a graphical control, test and measurement environment and development package. LabView is a graphical programming language that uses icons instead of classical lines of text (e.g. `C++, python`). Since its introduction in 1986, National Instruments has constantly extended LabViews functionality making it nowadays possible to control FPGA's, microcontrollers and embedded devices. Today, it is one of the most used software packages for test, measurement and control applications in industrial businesses but also in particle physics. A major feature of LabView is its built-in support to embed graphical user interfaces (GUIs).

A LabView program is called *virtual interface* (VI). It consists of two main parts, the front panel and the block diagram. The front panel is the place where the GUI is located. It consists of all the inputs and outputs that the program requires, which can generally be categorised into controls and indicators. Supported data types include integers, floats, complex numbers, strings and booleans. Especially the latter type in the form of switches or buttons is highly important in LabView. The block diagram holds the main program code. Here, functions are graphically pictured by blocks and are interconnected via lines. Depending on the data type, these lines are colour coded differently. The block diagram also provides the possibility to include other user made VI's into the current VI. These are called *SubVIs* and can be used to make the code modular and to increase its clarity. For this, each SubVI needs to have an own icon as well as connectors.

The VIs that were designed in the course of this thesis were developed using a full LabView Professional Development System, Version 2014 Service Pack 1 and Version 2015. All VIs programmed using the 2015 version have been tested successfully under the 2014 version.

B.2. Siemens LOGO!

Siemens LOGO! is a family of compact programmable logic controllers (PLCs) and logic modules which, particularly in more complex cases, can be programmed via a regular computer [Asc14]. For this, Siemens provides its own Siemens LOGO! Soft Comfort software suite. This software also allows to test the programmed LOGO! applications offline. All applications are based on the programming language *Function Block Diagram* (FBD), which is one of the five languages supported by the IEC 61131-3 standard [Deu06] for a PLC. Similar to LabView (see appendix B.1), it is a graphical programming language where functions are depicted as graphical blocks that are connected by lines.

B.3. ROOT

ROOT is an object-oriented framework that is predominantly used for data analysis [PQZ15]. It is developed by the CERN (European Organization for Nuclear Research) and based on the general-purpose programming languages `C/C++`. The ROOT framework is often used in high energy and particle physics, as it is optimized for very large data sets utilising vertical data storage techniques [Ant+09]. For this purpose, ROOT provides a data structure called `tree`, which consists of various branches. These branches are comprised of arrays containing floats or integers. Such trees can be rapidly saved and read. Another big advantage of ROOT is that it provides easy ways to visualise and mathematically analyse data. Especially histograms can be generated effortlessly with ROOT.

B.4. Gnuplot

Gnuplot is a portable, command line driven graphing utility for multiple platforms including Microsoft Windows and Linux [Wil+11]. Gnuplot has its own command line language. Data can be visualised in either 2D or 3D plots. Support to draw vector files, surfaces or contours is also built in. The graphical output can be viewed via an interactive terminal or via an output file. Aside the typical file formats (e.g. `.png`, `.pdf`, `.eps`), Gnuplot also supports the direct integration into LaTeX via a `.tex` file. Furthermore, Gnuplot does feature basic statistical analysis tools. The statistical properties (e.g. the average) of a set of data or a file can be effortlessly determined using Gnuplot. A basic functionality allowing to fit data sets is built in. Gnuplot (version 5) was often used during this thesis for plotting or calculating averages due to its interactiveness and simplicity, especially when the undeniably larger functionality of the ROOT framework was unnecessary.

B.5. CoolTerm & HTerm

CoolTerm is a serial port terminal application that allows to monitor and display the data exchange between multiple serial ports (e.g. COM-ports) concurrently. The program can send data and text files to a device via the COM-port. CoolTerm allows to log the monitored data to a data file. This was the main intended purpose of CoolTerm within the context of this thesis. CoolTerm offers support for various operating systems including Microsoft Windows and Linux, however incompatibilities with Windows 10 were observed. For this reason, HTerm was used on Windows 10 based machines. It provides similar features as CoolTerm.

Bibliography

[3M 10] 3M Interconnect Solutions. *3M Twisted Pair Flat Cable: 2100 Series*. 2010. URL: http://multimedia.3m.com/mws/media/224310/3mtm-twisted-pair-flat-cable-2100-series-ts0762.pdf (visited on 08/28/2016).

[Ach+06] A. Achterberg et al. "First year performance of the IceCube neutrino telescope". In: *Astroparticle Physics* 26.3 (2006), pp. 155–173. ISSN: 09276505. DOI: 10.1016/j.astropartphys.2006.06.007. URL: http://arxiv.org/abs/astro-ph/0604450 (visited on 09/25/2016).

[Ada+07] T. Adam et al. "The OPERA experiment Target Tracker". In: *Nuclear Instruments and Methods in Physics Research Section A: Accelerators, Spectrometers, Detectors and Associated Equipment* 577.3 (2007), pp. 523–539. ISSN: 01689002. DOI: 10.1016/j.nima.2007.04.147.

[Ada+15] T. Adam et al. *JUNO Conceptual Design Report*. 2015. URL: http://arxiv.org/pdf/1508.07166v2.

[Aie+12] S. Aiello et al. "Influence of the Earth's Magnetic Field on Large Area Photomultipliers". In: *IEEE Transactions on Nuclear Science* 59.4 (2012), pp. 1259–1267. ISSN: 0018-9499. DOI: 10.1109/TNS.2012.2189245.

[AME08] AMETEK/ORTEC, ed. *Electronics Standards and Definitions*. Mar. 1, 2008.

[An+15] Fengpeng An et al. "Neutrino physics with JUNO". In: *Journal of Physics G: Nuclear and Particle Physics* 43.3 (2015), p. 030401. ISSN: 0954-3899. DOI: 10.1088/0954-3899/43/3/030401.

[Ang+05] J. Angrik et al. *KATRIN design report 2004*. Ed. by KATRIN Collaboration. 2005.

[Ant+09] I. Antcheva et al. "ROOT - A C++ framework for petabyte data storage, statistical analysis and visualization". In: *Computer Physics Communications* 180.12 (2009), pp. 2499–2512. ISSN: 00104655. DOI: 10.1016/j.cpc.2009.08.005.

[ARD16] ARDUINO S.R.L., ed. *Arduino: Boards*. 2016. URL: http://www.arduino.org/ (visited on 10/01/2016).

[Ard16] Arduino, ed. *Arduino - Products*. 2016. URL: https://www.arduino.cc/en/Main/Products (visited on 10/01/2016).

[Asc14] Bernd Aschendorf. *Energiemanagement durch Gebäudeautomation: Grundlagen - Technologien - Anwendungen*. Berlin: Springer Vieweg, 2014. ISBN: 9783834805737. DOI: 10.1007/978-3-8348-2032-7. URL: http://gbv.eblib.com/patron/FullRecord.aspx?p=1106485.

[B11] Seth B. *Arduino and Dallas DS1820 (one-wire)*. Ed. by National Instruments. 2011. URL: https://decibel.ni.com/content/thread/9701 (visited on 10/02/2016).

[Bar12] Erik Bartmann. *Die elektronische Welt mit Arduino entdecken: [behandelt Arduino 1.0 ; mit dem Arduino messen, steuern und spielen ; Elektronik leicht verstehen ; kreativ programmieren lernen]*. 1. Aufl., 3., korr. Nachdr. O'Reillys basics. Beijing: O'Reilly, 2012. ISBN: 978-3-89721-319-7.

[BBR06] Aveek Bid, Achyut Bora, and A. K. Raychaudhuri. "Temperature dependence of the resistance of metallic nanowires: Applicability of Bloch-Grüneisen theorem". In: *Physical Review B* 74.3 (2006). ISSN: 1098-0121. DOI: 10.1103/PhysRevB.74.035426.

[BD76] J. N. Bahcall and R. Davis JR. "Solar neutrinos: a scientific puzzle". In: *Science (New York, N.Y.)* 191.4224 (1976), pp. 264–267. ISSN: 0036-8075. DOI: 10.1126/science.191.4224.264.

[Bec16] Beckhoff Automation GmbH & Co. KG, ed. *BECKHOFF: New Automation Technology*. 29.09.2016. URL: https://www.beckhoff.de/ (visited on 10/01/2016).

[Bei16] Bosse Bein. "Aufbau eines Teststandes zur Charakterisierung von PMTs in magnetischen Feldern". Bachelor thesis. Hamburg: University of Hamburg, 2016. (Visited on 09/18/2016).

[Bel+13] G. Bellini et al. "Cosmogenic Backgrounds in Borexino at 3800 m water-equivalent depth". In: *Journal of Cosmology and Astroparticle Physics* 2013.08 (2013), p. 049. ISSN: 1475-7516. DOI: 10.1088/1475-7516/2013/08/049.

[Bet07] A. Bettini. "GERDA. Germanium Detector Array. Search for Neutrino-less ββDecay of 76Ge". In: *Nuclear Physics B - Proceedings Supplements* 168 (2007), pp. 67–69. ISSN: 09205632. DOI: 10.1016/j.nuclphysbps.2007.02.018.

[Boc+14] Valerio Bocci et al. "The ArduSiPM a compact trasportable Software/Hardware Data Acquisition system for SiPM detector". In: *2014 IEEE Nuclear Science Symposium and Medical Imaging Conference (NSS/MIC)*. 2014, pp. 1–5. DOI: 10.1109/NSSMIC.2014.7431252. (Visited on 07/29/2016).

[Bri+13] T. Briese et al. *Testing of Cryogenic Photomultiplier Tubes for the MicroBooNE Experiment*. 2013. URL: http://arxiv.org/pdf/1304.0821v4 (visited on 09/26/2016).

[Brü12] Thomas Brühlmann. *Arduino Praxiseinstieg: Behandelt Arduino 1.0*. 2nd ed. Mitp Professional. Verlagsgruppe Hüthig Jehle Rehm, 2012. ISBN: 978-3-8266-8342-8.

[Bur16] Miles Burton. *Arduino-Temperature-Control-Library*. 3.08.2016. URL: https://github.com/milesburton/Arduino-Temperature-Control-Library (visited on 10/02/2016).

[CAE15] CAEN, ed. *CAEN: Electronic Instumentation: Tools for Discovery*. 2015. URL: http://www.caen.it/csite/HomePage.jsp (visited on 10/01/2016).

[Cap+14] F. Capozzi et al. "Status of three-neutrino oscillation parameters, circa 2013". In: *Physical Review D* 89.9 (2014). ISSN: 1550-7998. DOI: 10.1103/PhysRevD.89.093018.

[Con16] Conrail Container GmbH, ed. *Betriebsanleitung 20" HC Kühl-/Heizcontainer CCCU500052_3 AG262: UNI- Hamburg*. Apr. 2016.

[Cow+56] C. L. Cowan JR et al. "Detection of the Free Neutrino: a Confirmation". In: *Science (New York, N.Y.)* 124.3212 (1956), pp. 103–104. ISSN: 0036-8075. DOI: 10.1126/science.124.3212.103.

[Cvi11] D. Cvijović. "The Bloch-Gruneisen function of arbitrary order and its series representations". In: *Theor. Math. Phys. (Theoretical and Mathematical Physics)* 166.1 (2011), pp. 37–42. DOI: 10.1007/s11232-011-0003-4.

[Dan+62] G. Danby et al. "Observation of High-Energy Neutrino Reactions and the Existence of Two Kinds of Neutrinos". In: *Physical Review Letters* 9.1 (1962), pp. 36–44. ISSN: 0031-9007. DOI: 10.1103/PhysRevLett.9.36.

[Deu05] Deutsches Institut für Normung e.V. *Industrial platinum resistance thermometers and platinum temperature sensors (IEC 60751:2008); German version EN 60751:2008*. Berlin, 2009-05.

[Deu06] Deutsches Institut für Normung e.V. *Programmable controllers - Part 3: Programming languages (IEC 61131-3:2013); German version EN 61131-3:2013*. Berlin, 2014-06.

[Dus23] Saul Dushman. "Electron Emission from Metals as a Function of Temperature". In: *Physical Review* 21.6 (1923), pp. 623–636. ISSN: 0031-899X. DOI: 10.1103/PhysRev.21.623.

[EK16] Lisa Edelhäuser and Alexander Knochel. *Tutorium Quantenfeldtheorie: Was Sie schon immer über QFT wissen wollten, aber bisher nicht zu fragen wagten*. Berlin and Heidelberg: Springer Spektrum, 2016. ISBN: 978-3-642-37676-4. DOI: 10.1007/978-3-642-37676-4. URL: http://dx.doi.org/10.1007/978-3-642-37676-4.

[FM02] S. O. Flyckt and Carole Marmonier. *PHOTOMULTIPLIER TUBES: principles & applications*. Brive-la-Gaillarde, France, 2002. URL: http://www2.pv.infn.it/~debari/doc/Flyckt_Marmonier.pdf (visited on 09/18/2016).

[Fra+06] H. Franz et al. "Technical Report: PETRA III: DESY's New High Brilliance Third Generation Synchrotron Radiation Source". In: *Synchrotron Radiation News* 19.6 (2006), pp. 25–29. ISSN: 0894-0886. DOI: 10.1080/08940880601064984.

[Fuk+98] Y. Fukuda et al. "Evidence for Oscillation of Atmospheric Neutrinos". In: *Physical Review Letters* 81.8 (1998), pp. 1562–1567. ISSN: 0031-9007. DOI: 10.1103/PhysRevLett.81.1562.

[GGS58] M. Goldhaber, L. Grodzins, and A. W. Sunyar. "Helicity of Neutrinos". In: *Physical Review* 109.3 (1958), pp. 1015–1017. ISSN: 0031-899X. DOI: 10.1103/PhysRev.109.1015.

[Giu+13] Elena Giusarma et al. "Constraints on neutrino masses from Planck and Galaxy clustering data". In: *Physical Review D* 88.6 (2013). ISSN: 1550-7998. DOI: 10.1103/PhysRevD.88.063515.

[GM11] Wolfgang Georgi and Ergun Metin. *Einführung in LabVIEW: Mit ... 146 Aufgaben ; [Studentenversion inklusive]*. 4., neu bearb. Aufl., [Nachdr.] München: Fachbuchverl. Leipzig im Carl-Hanser-Verl., 2011. ISBN: 3446415602. URL: `http://www.gbv.de/dms/faz-rez/FTUM200905162269313_8.pdf`.

[GM12] Rudolf Gross and Achim Marx. *Festkörperphysik*. München: Oldenbourg, 2012. ISBN: 978-3-486-71294-0. URL: `http://dx.doi.org/10.1524/9783486714869`.

[Gra16] Marco Grassi. *JUNO: a General Purpose Experiment for Neutrino Physics*. 2016. URL: `http://arxiv.org/pdf/1605.09118v1`.

[Grü33] E. Grüneisen. "Die Abhängigkeit des elektrischen Widerstandes reiner Metalle von der Temperatur". In: *Annalen der Physik* 408.5 (1933), pp. 530–540. ISSN: 00033804. DOI: `10.1002/andp.19334080504`.

[Gul+00] M. Guler et al. "OPERA: An appearance experiment to search for nu/mu <-> nu/tau oscillations in the CNGS beam. Experimental proposal: Experiment Proposal". In: *CERN/SPSC 2000-028; SPSC/P318; LNGS P25/2000* (2000).

[HAM07] HAMAMATSU PHOTONICS K. K. *PHOTOMULTIPLIER TUBES: Basics and Applications*. 2007.

[HAM15] HAMAMATSU PHOTONICS K.K., ed. *Final Test Sheet: Photomultiplier Tube, Type: R12860 HQE: HPD/Uni Hamburg*. Dec. 18, 2015.

[HAM98] HAMAMATSU PHOTONICS K.K., ed. *Photomultiplier Tubes: Construction and Operating Characteristics, Connections to External Circuits*. 1998.

[Ibr02] Dogan Ibrahim. *Microcontroller-based temperature monitoring and control*. Oxford: Newnes, 2002. ISBN: 9780750655569. URL: `http://proquest.tech.safaribooksonline.de/9780750655569`.

[Ice16] IceCube Collaboration, ed. *PINGU: A Vision for Neutrino and Particle Physics at the South Pole*. 2016. URL: `http://arxiv.org/pdf/1607.02671.pdf` (visited on 09/25/2016).

[Ing08] Ingersoll Rand, Climate Control Technologies – ESA, ed. *MAGNUM+: TK 60275-4-MM*. Ireland, Sept. 2008.

[Int13] Intel Corporation, ed. *Export Compliance Metrics for Intel® Itanium® and Pentium® Processors*. 2013. URL: http://www.intel.com/content/www/us/en/support/processors/000007250.html#3 (visited on 09/26/2016).

[Jil98] David Jiles. *Introduction to magnetism and magnetic materials*. 2. ed. London u.a: Chapman & Hall, 1998. ISBN: 9780412798603.

[Kat13] Ulrich F. Katz. *The ORCA Option for KM3NeT*. Ed. by KM3NeT Collaboration. 2013. URL: https://arxiv.org/pdf/1402.1022v1.pdf (visited on 09/25/2016).

[Kod+01] K. Kodama et al. "Observation of tau neutrino interactions". In: *Physics Letters B* 504.3 (2001), pp. 218–224. ISSN: 03702693. DOI: 10.1016/S0370-2693(01)00307-0.

[KS95] Hans Volker Klapdor-Kleingrothaus and Andreas Staudt. *Teilchenphysik ohne Beschleuniger*. Teubner Studienbücher Physik. Wiesbaden: Vieweg+Teubner Verlag, 1995. ISBN: 978-3-322-89144-0. DOI: 10.1007/978-3-322-89144-0. URL: http://dx.doi.org/10.1007/978-3-322-89144-0.

[Kuc14] Horst Kuchling. *Taschenbuch der Physik: Mit zahlreichen Tabellen*. 21., aktualisierte Aufl., Jub.-Ausg. 50 Jahre. München: Fachbuchverl. Leipzig im Carl-Hanser-Verl., 2014. ISBN: 978-3-446-44218-4.

[Kus09] Alexander Kusenko. "Sterile neutrinos: The dark side of the light fermions". In: *Physics Reports* 481.1-2 (2009), pp. 1–28. ISSN: 03701573. DOI: 10.1016/j.physrep.2009.07.004.

[Lal08] K. Lal Kishore. *Operational amplifiers and linear integrated circuits*. New Delhi: Dorling Kindersley (India), 2008. ISBN: 978-81-7758-566-7. URL: http://proquest.tech.safaribooksonline.de/9788131709863.

[Lap16] Lapp Group, ed. *Lapp Kabel: Product Information: UNITRONIC® LiYY*. Jan. 13, 2016. URL: http://products.lappgroup.com/online-catalogue/data-communication-systems/low-frequency-data-transmission-cables/din-colour-code/unitronic-liyy.html (visited on 10/03/2016).

[Lea10] Trystan Lea. *4x Multiplexed RTD Temperature sensor module*. Ed. by OpenEnergyMonitor. 30.11.2010. URL: https://openenergymonitor.org/emon/buildingblocks/rtd-temperature-sensing (visited on 10/02/2016).

[Li16] Yu-Feng Li. *Jiangmen Underground Neutrino Observatory: Status and Prospectives*. 2016. URL: `http://arxiv.org/pdf/1606.04743v1`.

[LS05] Thierry Lasserre and Henry W. Sobel. "Reactor neutrinos". In: *Comptes Rendus Physique* 6.7 (2005), pp. 749–757. ISSN: 16310705. DOI: `10.1016/j.crhy.2005.08.002`.

[Lu14] Haoqi Lu. "Reactor antineutrino experiments". In: *International Journal of Modern Physics: Conference Series* 31 (2014). ISSN: 2010-1945. DOI: `10.1142/S201019451460283X`.

[Max15] Maxim Integrated, ed. *DS18B20: Programmable Resolution 1-Wire Digital Thermometer*. 2015. URL: `https://datasheets.maximintegrated.com/en/ds/DS18B20.pdf` (visited on 07/08/2016).

[MM12] Thomas Michael and Irene Munt, eds. *Diercke - Weltatlas*. [Vollst. Neubearb.], 1. Aufl., Dr. A, [Nachdr.] Braunschweig: Westermann, 2012. ISBN: 9783141007008.

[MNS62] Ziro Maki, Masami Nakagawa, and Shoichi Sakata. "Remarks on the Unified Model of Elementary Particles". In: *Progress of Theoretical Physics* 28.5 (1962), pp. 870–880. ISSN: 0033-068X. DOI: `10.1143/PTP.28.870`.

[Nar16] Stephan Narison. *Particles and the universe: From the Ionian school to the Higgs Boson and beyond*. New Jersey et al.: World Scientific, 2016. ISBN: 978-981-4644-68-6.

[Nat] National Oceanic and Atmospheric Administration (NOAA), ed. *NCEI Geomagnetic Calculators*. URL: `http://www.ngdc.noaa.gov/geomag-web/#igrfwmm` (visited on 10/02/2016).

[Nat09] National Instruments, ed. *S7 PLC TCP/IP Protocol Reference Example*. 2009. URL: `https://decibel.ni.com/content/docs/DOC-5467#/?page=3` (visited on 10/07/2016).

[Nat16] National Instruments, ed. *LabView MakerHub: LINX*. 2016. URL: `https://www.labviewmakerhub.com/doku.php?id=libraries:linx:start` (visited on 10/02/2016).

[Oht+16] Kenji Ohta et al. "Experimental determination of the electrical resistivity of iron at Earth's core conditions". In: *Nature* 534.7605 (2016), pp. 95–98. ISSN: 0028-0836. DOI: `10.1038/nature17957`. URL: `http://www.nature.com/nature/journal/v534/n7605/full/nature17957.html` (visited on 10/04/2016).

[Oli14] K. A. Olive. "Review of Particle Physics: Particle Data Group". In: *Chinese Physics C* 38.9 (2014), p. 090001. ISSN: 1674-1137. DOI: 10.1088/1674-1137/38/9/090001.

[PK82] D. B. Poker and C. E. Klabunde. "Temperature dependence of electrical resistivity of vanadium, platinum, and copper". In: *Physical Review B* 26.12 (1982), pp. 7012–7014. ISSN: 1098-0121. DOI: 10.1103/PhysRevB.26.7012. URL: http://journals.aps.org/prb/pdf/10.1103/PhysRevB.26.7012.

[Pol10] Chris Polly. *Neutrino history 1927 - 1987: 1930: Pauli neutrino letter (translated by Kurt Riesselmann): MicroBooNE-doc-953-v1*. 2010. URL: http://microboone-docdb.fnal.gov/cgi-bin/ShowDocument?docid=953 (visited on 09/11/2016).

[Pov+15] Bogdan Povh et al. *Particles and Nuclei: An Introduction to the Physical Concepts*. 7th ed. 2015. Graduate Texts in Physics. Berlin, Heidelberg and s.l.: Springer Berlin Heidelberg, 2015. ISBN: 978-3-662-46321-5. DOI: 10.1007/978-3-662-46321-5. URL: http://dx.doi.org/10.1007/978-3-662-46321-5.

[PQZ15] Danilo Piparo, Günter Quast, and Manuel Zeise. *A ROOT Guide for Students: Diving Into ROOT*. 2015.

[PR10] Pedro Ponce-Cruz and Fernando D. Ramírez-Figueroa. *Intelligent Control Systems with LabVIEW™*. London: Springer-Verlag London, 2010. ISBN: 978-1-84882-683-0. DOI: 10.1007/978-1-84882-684-7. URL: http://site.ebrary.com/lib/alltitles/docDetail.action?docID=10351869.

[Rey+91] K. J. Reynolds et al. "Temperature dependence of led and its theoretical effect on pulse oximetry". In: *British journal of anaesthesia* 67.5 (1991), pp. 638–643. ISSN: 0007-0912.

[Sch11] Friederike Schöck. "Studies on atmospheric neutrino oscillations with the ANTARES neutrino telescope". Doctoral thesis. Nürnberg: Friedrich-Alexander University Erlangen-Nürnberg, 2011.

[Sch16] Stefan Scherer. *Symmetrien und Gruppen in der Teilchenphysik*. 1. Aufl. 2016. Berlin and Heidelberg: Springer Spektrum, 2016. ISBN: 978-3-662-47733-5. DOI: 10.1007/978-3-662-47734-2. URL: http://dx.doi.org/10.1007/978-3-662-47734-2.

[SE15] Saman Saeedi and Azita Emami. "Silicon-photonic PTAT temperature sensor for micro-ring resonator thermal stabilization". In: *Optics express* 23.17 (2015), pp. 21875–21883. ISSN: 1094-4087. DOI: 10.1364/OE.23.021875. URL: https://www.osapublishing.org/DirectPDFAccess/8B954193-9A52-263B-AEFD8B11AB7EA8BE_324004/oe-23-17-21875.pdf?da=1&id=324004&seq=0&mobile=no (visited on 07/27/2016).

[SNO01] SNO Collaboration, ed. *Measurement of charged current interactions produced by 8B solar neutrinos at the Sudbury Neutrino Observatory*. June 18, 2001. URL: http://www.sno.phy.queensu.ca/sno/first_results/sno_first_results.pdf (visited on 09/21/2016).

[Ste] Stefan Mayer Instruments, ed. *Magnetic Field Sensor FLC3-70: Triaxial fluxgate sensor with high sensitivity*.

[Ste17] Lisa Steppat. "Development and commissioning of the setup for the masstesting of JUNO PMTs: (Work in progress)". Master thesis. Hamburg, Germany: University of Hamburg, 2017.

[Sto+16] Paul Stoffregen et al. *OneWire Library*. 27.09.2016. URL: http://www.pjrc.com/teensy/td_libs_OneWire.html (visited on 10/02/2016).

[Str+15] Virginia Strati et al. "Expected geoneutrino signal at JUNO". In: *Progress in Earth and Planetary Science* 2.1 (2015), p. 70. DOI: 10.1186/s40645-015-0037-6. URL: https://arxiv.org/ftp/arxiv/papers/1412/1412.3324.pdf (visited on 10/01/2016).

[Tex13] Texas Instruments Incorporated, ed. *AN-460 LM34/LM35 Precision Monolithic Temperature Sensors*. May 2013. URL: http://www.ti.com/lit/an/snoa748c/snoa748c.pdf (visited on 07/27/2016).

[Tex16] Texas Instruments Incorporated, ed. *LM35 Precision Centigrade Temperature Sensors*. Aug. 2016. URL: http://www.ti.com/lit/ds/symlink/lm35.pdf (visited on 07/27/2016).

[The06] Thermal Developments International Ltd., ed. *Hand made platinum resistance temperature detectors*. 2006. URL: http://www.t-d-i.co.uk/pdfs/tdi-cat.pdf.

[Tit+14] Ilya E. Titkov et al. "Temperature-Dependent Internal Quantum Efficiency of Blue High-Brightness Light-Emitting Diodes". In: *IEEE Journal of Quantum Electronics* 50.11 (2014), pp. 911–920. ISSN: 0018-9197. DOI: 10.1109/JQE.2014.2359958.

[Top09] Topcraft. *Bedienungsanleitung: Ultraschall-Entfernungsmesser: GT-UDM-07*. 2009.

[TS80] Ulrich Tietze and Christoph Schenk. *Halbleiter-Schaltungstechnik*. 5., überarb. Aufl. Berlin: Springer, 1980. ISBN: 3-540-09848-8.

[Uni15] Universität Hamburg: Forschungsgruppe Neutrinophysik. *JUNO*. 2015. URL: http://www.neutrino.uni-hamburg.de/projekte/juno/ (visited on 10/31/2016).

[VWZ15] P. Vogel, L. J. Wen, and C. Zhang. "Neutrino oscillation studies with reactors". In: *Nature Communications* 6 (2015). DOI: 10.1038/ncomms7935.

[WIK16] WIKA Alexander Wiegand SE & Co. KG, ed. *Technical information: Operating limits and tolerances of platinum resistance thermometers per EN 60751: 2008: WIKA data sheet IN 00.17*. Klingenberg, Germany, Feb. 2016. URL: http://de-de.wika.de/upload/DS_IN0017_en_co_20804.pdf (visited on 10/04/2016).

[Wil+11] Thomas Williams et al. *Gnuplot 4.4: An Interactive Plotting Program*. 2011. URL: http://www.gnuplot.info/docs_4.4/gnuplot.pdf.

[WS12] Theophilus Wellem and Bhudi Setiawan. "A Microcontroller-based Room Temperature Monitoring System". In: *International Journal of Computer Applications* 53.1 (2012), pp. 7–10. ISSN: 09758887. DOI: 10.5120/8383-1984.

[Wu+57] C. S. Wu et al. "Experimental Test of Parity Conservation in Beta Decay". In: *Physical Review* 105.4 (1957), pp. 1413–1415. ISSN: 0031-899X. DOI: 10.1103/PhysRev.105.1413.

[WZ08] Günter Wellenreuther and Dieter Zastrow. *Automatisieren mit SPS — Theorie und Praxis*. Wiesbaden: Vieweg+Teubner, 2008. ISBN: 978-3-528-23910-7. DOI: 10.1007/978-3-8348-9018-4.

[ZFM14] M. A. Zermani, Elyes Feki, and Abdelkader Mami. "Temperature Acquisition and Control System based on the Arduino". In: *IJESE (International Journal of Emerging Science and Engineering)* 2.12 (2014). URL: http://citeseerx.ist.psu.edu/viewdoc/download?doi=10.1.1.676.5690&rep=rep1&type=pdf (visited on 07/29/2016).

[Zha+08] Liang Zhan et al. "Determination of the neutrino mass hierarchy at an intermediate baseline". In: *Physical Review D* 78.11 (2008). ISSN: 1550-7998. DOI: 10.1103/PhysRevD.78.111103.

[Zin+73] V. E. Zinov'ev et al. "Matthiessen Rule and High-Temperature Electrical Resisitivity of Solid Solutions of Silicon in Iron". In: *Soviet Physics JETP* 36.6 (1973).

[Zub12] Kai Zuber. *Neutrino physics*. 2. ed. Series in high energy physics, cosmology and gravitation. Boca Raton, Fla.: CRC Press / Taylor & Francis, 2012. ISBN: 978-1-4200-6471-1.

List of Abbreviations

ADC	Analogue to digital converter
ADS	Automation device specification
Amp	Amplifier
API	Application-Programming-Interface
bis-MSB	1.4-bis[2-(2-methylphenyl)ethenyl]-benzene
CERN	Conseil Européen pour la Recherche Nucléaire
CHK	Check
CKM	Cabibbo-Kobayashi-Maskawa
COM	Communication
CP	Charge parity
CPU	Central processing unit
DAQ	Data acquisition
DCR	Dark count rate
DNSB	Diffuse supernova neutrino background
DONUT	Direct Obersvation of the nu tau (experiment)
FLOPS	Floating operations per second
FP	Front panel
GERDA	Germanium Detector Array (experiment)
GND	Ground

HVAC	Heating, ventilation and air conditioning
I/O	Input/Output
IDE	Integrated development environment
IH	Inverted (mass) hierarchy
INOP	Inoperative
IOPS	Integer operations per second
JUNO	Jiangmen Underground Neutrino Observatory
KATRIN	Karlsruhe Tritium Neutrino (experiment)
LAB	Linear Alkyl-Benzyne
LabView	Laboratory Virtual Instrument Engineering Workbench
LAND	Liquid Scintillator Antineutrino Detector
LED	Light emitting diode
LIFA	Labview Interface for Arduino
LTD	Low threshold discriminator
MCA	Multichannel analyser
MCP	Microchannel plate
MH	Mass hierarchy
MWE	Meter water equivalent
NCEI	National Centers for Environmental Information
NH	Normal (mass) hierarchy
NIM	Nuclear Instrumentation Module (standard)
NNVT	Northern Night Vision Technology
NOAA	National Oceanic and Atmospheric Administrations

NPP	Nuclear power plant
Op-amp	Operational amplifier
OPERA	Oscillation Project with Emulsion Tracking Apparatus
ORCA	Oscillation Research with Cosmics in the Abyss
OS	Operating system
PDE	Photo detection efficiency
PETRA	Positron Electron Tandem Ring Accelerator
PINGU	Precision IceCube Next Generation Upgrade
PLC	Programmable logic controller
PM	Photomultiplier
PMNS	Pontecorvo-Maki-Nakagawa-Sakata
PMT	Photomultiplier tube
PPO	2.5-Diphenyloxazole
PTAT	Proportional to absolute temperature
PVC	Polyvinyl chloride
PWM	Pulse-width modulation
QCD	Quantum chromodynamics
QE	Quantum efficiency
QFT	Quantum field theory
ROM	Read-only memory
RTD	Resistance temperature detector
SM	Standard Model
SNO	Sudbury Neutrino Observatory
SP	Setpoint
ST	Structured Text

STS Status
SUSY Supersymmetry

TDE Text display expansion
TTL Transistor-transistor Logic

USB Universal Serial Bus

VI Virtual instrument
VM Variable memory

List of Figures

List of Tables

Acknowledgements

First of all, I would like to thank

Prof. Dr. Caren HAGNER

for allowing me to write my bachelor thesis in the neutrino physics research group. Special thanks are also due to

Dr. Björn WONSAK

for supervising as well as proof reading my thesis. Also, I would like to express my deepest thanks to

Henning REBBER,

for not only helping me during all works concerning the JUNO container, especially the implementation of the remote control system, but also for proof reading various of iterations of this thesis. Also, I greatly appreciated the help of

Dr. Daniel BICK

for all advices concerning Linux and the ROOT framework. Special thanks also to

Dr. Joachim EBERT *and* *Hans-Jürgen* OHMACHT

for supporting me in the laboratory and answering my questions about hardware, electronics and other technical or practical issues. Also, I greatly welcomed the advice and support of

Lisa STEPPAT,

while performing measurements with the test stands in the laboratory as well as for providing records and suggestions for upcoming lectures. Naturally, thanks are also due to all remaining members of the research group:

Dr. Björn OPITZ	*Stefan* BIESCHKE	*David J.* MEYHÖFER
Annika HOLLNAGEL	*Felix* BENCKWITZ	*Daniel* HARTWIG
Simon REICHERT	*Hauke* SCHMIDT	*Benedict* SCHACHT

Eidesstattliche Erklärung

Hiermit erkläre ich an Eides Statt, dass die vorliegende Arbeit von mir selbständig verfasst wurde und ich keine anderen als die angegebenen Hilfsmittel, insbesondere keine im Quellenverzeichnis nicht benannten Internet-Quellen, benutzt habe. Sämtliche Stellen der Arbeit, die im Wortlaut oder dem Sinn nach anderen gedruckten oder im Internet verfügbaren Werken entnommen sind, habe ich durch genaue Quellenangaben kenntlich gemacht. Die Arbeit wurde von mir vorher nicht in einem anderen Prüfungsverfahren eingereicht. Die eingereichte schriftliche Fassung entspricht der auf dem elektronischen Speichermedium. Ich bin damit einverstanden, dass die Bachelorarbeit veröffentlicht wird.

Freie und Hansestadt Hamburg, Datum

Unterschrift

Statutory declaration

I hereby declare that I have authored this thesis independently and that I have not used other than the declared resources, in particular no Internet resources that are not labelled in the bibliography. I have explicitly marked all material which has been quoted either literally or by content from the used sources. This thesis has not been submitted in another examination procedure before. The submitted, written version conforms with the one on the electronic storage medium. I agree that the thesis will be published.

Free and Hanseatic City of Hamburg, date

Signature